Chapter 4
Ultramafic Lower-Mantle Mineral Association

Abstract The juvenile ultramafic lower mantle is composed of the following mineral association: bridgmanite + ferropericlase + CaSi-perovskite + free silica. Bridgmanite, with mg = 0.84–0.96 forms two compositional groups: low-Al and high-Al. High-Al bridgmanite is richer in Fe and infers the characteristic of deeper layers in the lower mantle. The crystal structure of bridgmanite is orthorhombic through the entire lower mantle down to the D″ layer. The chemical composition of ferropericlase differs from the predicted composition, with the magnesium index mg varying from 0.36 to 0.90. Low-Fe ferropericlase has a cubic rocksalt structure, which is stable throughout the entire lower mantle. Iron contents in both ferropericlase and bridgmanite and ferropericlase increase with increasing pressure, indicating higher Fe concentration in the lower mantle with increasing depth. CaSi-perovskite is remarkably clean in its chemical composition with only minor admixtures of Ti, Al and Fe, but is enriched in trace elements. CaSi-perovskite within the lower mantle has a cubic structure, which, at low temperatures (in subsolidus conditions), may transfer into a tetragonal or orthorhombic structure. The presence of free silica in the lower mantle was identified in geological samples from all areas. In the upper part of the lower mantle, it is represented by stishovite; at a depth of 1600–1800 km, stishovite transforms into the $CaCl_2$-structured polymorph; and at the core–mantle boundary, into a α-PbO_2 phase seifertite. In addition to the major minerals, a variety of other mineral phases occur in the lower mantle: Mg–Cr–Fe, Ca–Cr and other orthorhombic oxides, jeffbenite, ilmenite, native Ni and Fe, moissanite and some others.

4.1 General

According to experimental data, three major minerals comprise the juvenile, ultramafic lower mantle: bridgmanite, CaSi-perovskite, and ferropericlase. However, significant differences occur between the model experimental composition and observations made in natural ultramafic lower-mantle associations.

First, the proportion of the major minerals that occur in natural samples differs significantly the proportion of major minerals suggested by experimental data.

Bridgmanite, which is supposed to comprise 77% of the lower mantle volume, comprises (in different regions) only 5–10% of all lower-mantle mineral inclusions in diamond; while ferropericlase, which is expected to comprise 18%, accounts for the majority of the lower-mantle inclusions at 48–63%.

Second, the fourth major mineral, free silica, SiO_2, occurs in the lower-mantle ultramafic association; it comprises (in different areas) between 2 and 20% of all lower-mantle inclusions in diamond (average: 8.4%). At depth, it exists as stishovite and post-stishovite phases; however, because of their instability it occurs in samples as a form of quartz. However, its usual association with ferropericlase and CaSi-perovskite proves its primary origin within the lower mantle.

Third, the composition of major minerals from the calculated ultramafic association differs from the theoretical and experimental data. Bridgmanite in natural samples has a magnesium index $mg = 0.84$–0.96 (average: 0.916), conversely, the predicted values of magnesium index were $mg = 0.80$–0.88. Differences in the composition of ferropericlase are more drastic: instead of the expected $mg = 0.73$–0.88, in the natural mineral, mg varies widely from 0.36 to 0.90, forming a series of periclase–wüstite solid solution compositions.

Fourth, other minerals exist in the lower-mantle ultramafic association. For example, the recently found lower-mantle microxenolith is composed of ferropericlase; iron carbide; and two new orthorhombic oxides, $Mg(Cr,Fe)_2O_4$ and $CaCr_2O_4$. Some other minerals are known in association with major lower-mantle minerals, such as jeffbenite; ilmenite; perovskite $CaTiO_3$; minerals with a composition of olivine and spinels; titanite; native nickel and iron; sulphides; and some other phases, the genesis of which remains unclear.

4.2 Bridgmanite (Mg,Fe)SiO₃

4.2.1 General

Bridgmanite (Brd) is the most abundant mineral in the lower mantle (Tschauner et al. 2014) and was previously known as magnesium silicate perovskite. The name 'perovskite' was initially derived from the $CaTiO_3$ analog in the perovskite family, which actually has a cubic crystal structure. It is a member of the perovskite family with an orthorhombic distortion of the ideal cubic perovskite structure and has the general formula of $^{VIII/XII}A^{2+}\ ^{VI}B^{4+}O^{2-}_3$, where the A site is a larger pseudo-dodecahedral site (with 8/12-fold coordination), mainly occupied by divalent cations, such as Mg, Fe, Mn, Ni, Ca; and the B site is a smaller six-fold octahedral site occupied by Si^{4+}, Al^{3+} and Fe^{3+} cations. The simplified formula that most represents lower-mantle bridgmanite is $(Mg,Fe)(Si,Al,Fe)O_3$, as other cations are much less abundant, but it should be noted that Fe^{3+} may also be present in the A site (McCammon et al. 1997; Lin et al. 2013). The crystal has an orthorhombic structure with space group *Pbnm* (Liu 1974; Fiquet et al. 2000).

Bridgmanite is formed as a result of the dissociation of ringwoodite (Mg,Fe)$_2$SiO$_4$ into ferropericlase and bridgmanite and is responsible for the 660 km seismic discontinuity. Due to the similarity in Fe–Mg partitioning across the transformation, it should take place over a narrow pressure interval, equivalent to <2 km in depth (Ito and Takahashi 1989; Ito et al. 1990), which is consistent with seismic observations of short-period reflected and converted phases (Kind and Li 2007).

Ringwood (1962) first suggested that MgSiO$_3$ might have a perovskite structure in the deep mantle and pointed out that such a structure would be a few percent denser than an isochemical mixture of MgO and SiO$_2$. This MgSi-perovskite was first synthesised by Liu (1974) from almandine-pyrope garnet, which was laser heated to about 1400–1800 °C at approximately 27 GPa in a diamond-anvil cell (DAC). Subsequently, Liu (1975) synthesised silicate perovskite by transformation of forsterite and enstatite at high pressure and temperature. Ever since then, bridgmanite, in various chemical compositions of geological relevance, had been synthesized in laser-heated DACs (LHDACs) and in multi-anvil apparatus (Ito and Matsui 1978). It is interesting to note that the discovery of the silicate perovskite, amongst many other discoveries in mineral physics, was made possible as a result of the invention of the LHDAC technique by Bassett (2001).

Bridgmanite has also been found in nature, including in meteorites and diamond inclusions (Scott Smith et al. 1984; Tomioka and Fujino 1997; Tschauner et al. 2014). In diamond inclusions, it has been found to be associated with ferropericlase, CaSi-perovskite, jeffbenite, a phase with the composition of olivine, chrome spinel, native nickel and sulphide. It forms colorless grains, 15–150 μm in size, which tend not to exhibit crystal faces. It may have an elongated ellipsoid, moderately well-formed euhedral shape, but its overall form is either indistinguishable or it has no discernable form at all. There is evidence for imposed 'negative' octahedral shape on a few grains (Fig. 4.1).
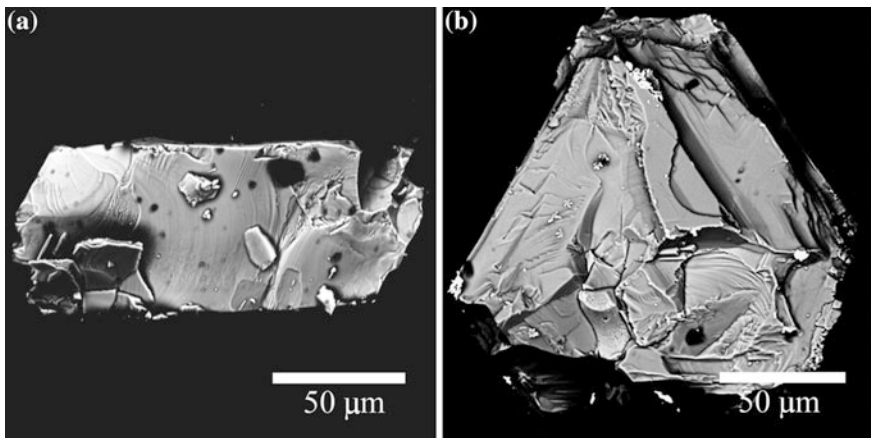
Fig. 4.1 Grains of bridgmanite extracted from diamonds of the Rio Soriso area, Brazil. SEM image. From Hayman et al. (2005)

The retrograde phase fully inherits its initial bridgmanite chemical composition, including a high Al content, which is not characteristic for enstatite. In its natural environment, it was found first as an inclusion in diamond from the Koffifontein kimberlite pipe, South Africa, where it was initially identified as 'enstatite' (Scott Smith et al. 1984). Subsequently, it was confirmed to be in association with ferropericlase in another diamond from the same pipe (Moore et al. 1986). Scott Smith et al. (1984) described it also as 'enstatite' in association with ferropericlase from a diamond in the Orroroo dyke, South Australia. Later 'MgSi-perovskite' was identified as inclusions in diamonds from placer deposits and kimberlite pipes in the Juina and Machado areas in Brazil (Wilding et al. 1991; Hutchison 1997; Harte et al. 1999; Kaminsky et al. 2001, 2009a, b; Hayman et al. 2005; Bulanova et al. 2008, 2010; Thomson et al. 2014; Zedgenizov et al. 2014a, 2015), from the Kankan placer deposit in Guinea (Stachel et al. 2000), from kimberlitic pipes in the Northwest Territories of Canada (Davies et al. 2004; Tappert et al. 2005a), and from the kimberlitic dyke K7 and ancient placer deposits from the Orroroo area in South Australia (Tappert et al. 2009b).

Due to its unstable nature under ambient conditions, this phase undergoes retrograde transformation to a pyroxene-type structure after extraction from diamond inclusions, inheriting the initial chemical composition. The identification of the retrograde phase as 'perovskite' was based on the analogy with experimental data and the association with other high-pressure (supposedly lower-mantle) minerals.

In meteorites, $(Mg,Fe)SiO_3$-perovskite was identified in the shock-induced veins in the Tenham L6 chondritic meteorite (Tomioka and Fujino 1997) using XRD and TEM; the perovskite grains showed an orthorhombic diffraction pattern, but became amorphous after the electron beam irradiation. This observed phase was inferred to have transformed from pyroxene at high pressures and temperatures by shock metamorphism. The structural data was sufficient for the International Mineralogical Association to approve bridgmanite as a new mineral (specimen IMA 2014-017). Bridgmanite was named after Percy W. Bridgman (1882–1961), the 1946 Nobel laureate, for his fundamental contributions to high-pressure physics (Tschauner et al. 2014).

4.2.2 Chemical Composition of Natural Bridgmanite

Analysis of the chemical composition of natural bridgmanite samples is mainly based on the full empirical formula of the ABO_3 oxide, where the pseudo-dodecahedral A site is occupied by large-size cations, Mg, Fe, Mn and Ca; and the octahedral B site contains smaller cations, Si and Al, with various cation substitutions. Its full formula is $(Mg, Fe, Mn, Ca)(Si,Al)O_3$. Ti (0–0.23 wt% TiO_2), Ni (0–0.09 wt% NiO) and K (0–0.26 wt% K_2O) are considered to be minor impurities (Table 4.1). All analyzed samples show almost ideal stoichiometry in accordance with experimental and theoretical data, with the exception of Al-rich samples, in which the B site shows excess cations, implying the presence of Al in

Table 4.1 Representative compositions of bridgmanite inclusions in diamond from different areas (wt%)

	Brazil			Machado	Canada	Guinea		Australia	Tenham L6
Country	Brazil			Machado	Canada	Guinea		Australia	Tenham L6
Area	Juina				Northwest Territories	Kankan		Ororoo	meteorite
Location	Sao Luiz placer		Rio Vermelho placer	Placer	Pipe DO27	Placer		Dyke Eurelia K7	
Sample No.	BZ207C	BZ242B	4-104	P33-1a	DO2700100	KK-103b	USNM 7703	FBS5-11	KK-16c
Mineral association	Brd + fPer + Jbn	Brd + fPer	Brd + Jbn	Brd + Jbn + 'Ol'	Brd + fPer + CaSiPrv	Brd + fPer	Brd + Akm + Rng + Maj + Msk	Brd + fPer	Brd + fPer + Sid
SiO$_2$	55.43	54.96	55.96	56.97	57.40	57.38	55.6	60.02	57.50
TiO$_2$	0.20	0.03	0.23	0.14	0.00	0.02	0.19	0.03	0.01
Al$_2$O$_3$	2.66	12.58	2.16	2.24	0.69	0.61	0.2	0.25	0.55
Cr$_2$O$_3$	0.15	1.75	0.17	0.03	0.28	0.17	0.13	0.38	0.28
FeO	9.02	3.95	8.57	4.71	2.85	3.39	13.7	2.93	3.34
NiO	0.03	0.01	n.a.	0.02	0.00	0.02	n.a.	0.09	0.01
MnO	0.30	1.29	0.20	0.04	0.07	0.10	0.49	0.15	0.11
MgO	32.03	16.35	32.26	33.68	37.90	35.92	27.9	36.58	35.94
CaO	0.05	4.38	0.03	0.73	0.39	0.07	0.9	0.05	0.07
Na$_2$O	0.07	4.63	0.10	0.42	n.a.	0.03	0.9	0.00	0.05
K$_2$O	0.00	0.01	0	0.18	n.a.	0.01	0.04	0.00	0.01
P$_2$O$_5$	n.a.	n.a.	n.a.	n.a.	n.a.	0.00	n.a.	0.00	0.00
Total	99.94	99.94	99.68	99.16	99.58	97.71	100.05	100.48	97.87
fe	0.136	0.119	0.130	0.073	0.040	0.050	0.216	0.043	0.050
mg	0.864	0.881	0.870	0.927	0.960	0.950	0.784	0.957	0.950
References	Hutchison (1997)		Kaminsky et al. (2001)	Burnham et al. (2016)	Davies et al. (2004)	Stachel et al. (2000)		Tappert et al. (2005a)	Tschauner et al. (2014)

Notes: *n.a.* not analyzed, *Akm* akimotoite, *Brd* bridgmanite, *CaSiPrv* CaSi-perovskite, *fPer* ferropericlase, *Jbn* jeffbenite, *Maj* majorite, *Msk* maskelynite, 'Ol' phase with a composition of olivine, *Rng* ringwoodite; *Sid* siderite
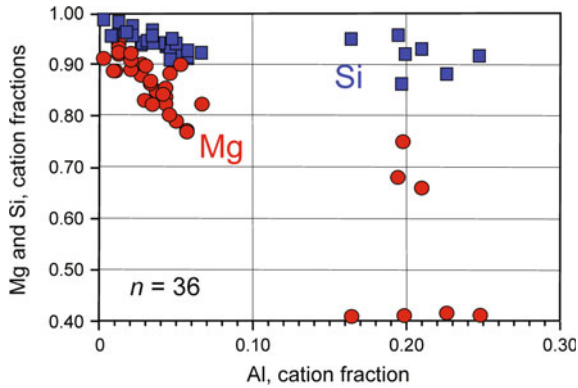
Fig. 4.2 Cation fractions of Mg (*red circles*), Si (*blue squares*) and Al in natural bridgmanite from diamond inclusions. The formula is on the basis of three oxygens

both A and B sites (Fig. 4.2). A permanent small deficit in the A site points to the presence of Fe, independent of its valence state, only in this site. An experimental single-crystal XRD study confirmed the presence of both Fe^{2+} and Fe^{3+} only in the A site (Vanpeteghem et al. 2006). Representative chemical compositions of natural bridgmanite are shown in Table 4.1.

The composition of the bridgmanite from the Tenham L6 meteorite is also included in the table. It significantly differs from the terrestrial bridgmanite (low Al and high *fe* first of all). It also differs from the 'mafic' bridgmanite (see Sect. 5.2.1). The specific composition of the meteoritic bridgmanite is most likely to have been caused by its occurrence in a shock-melt vein in the meteorite and its impact origin under non-equilibrium conditions.

Concentration of iron and magnesium index in bridgmanite. Iron, mainly in a divalent ferrous form of Fe^{2+}, enters into the pseudo-dodecahedral site A, as a substitute for Mg^{2+} because of their similarity in ionic radii (Shannon and Prewitt 1969; Fei et al. 1996). Although the modeled solubility of iron in bridgmanite reaches $fe = Fe/(Mg + Fe)_{at.} = 0.68$ (Dorfman et al. 2013), its concentration in natural bridgmanite is 2.85–10.40 wt% in total as FeO; and $fe = 0.04$–0.16. It was demonstrated experimentally that even great concentrations of Fe (Fe^{2+} or Fe^{3+}) do not occur in the octahedral B site; Fe replaces Mg only in the A site: $Fe_A^{2+} \leftrightarrow Mg_A^{2+}$ (Vanpeteghem et al. 2006).

The magnesium index in bridgmanite, $mg = Mg/(Mg + Fe)_{at.}$, is relatively uniform, varying within a range of 0.84–0.96 (average: 0.917 ± 0.066 (2σ)) (Fig. 4.3). The magnesium index in bridgmanite appears to show regional differences: for example, bridgmanites in Guinea and Canada are more magnesium rich ($mg = 0.92$–0.96) than bridgmanites in Brazil, where samples show lower Mg contents, with $mg = 0.84$–0.94. This possibly reflects different depths and/or sources of origin of bridgmanite in different areas. On the other hand, experimental mineral physics data suggest a lower magnesium index for bridgmanite, at 0.80–0.88 (Fei 1996; Lee et al. 2004; Irifune et al. 2010; Lin et al. 2013). In the
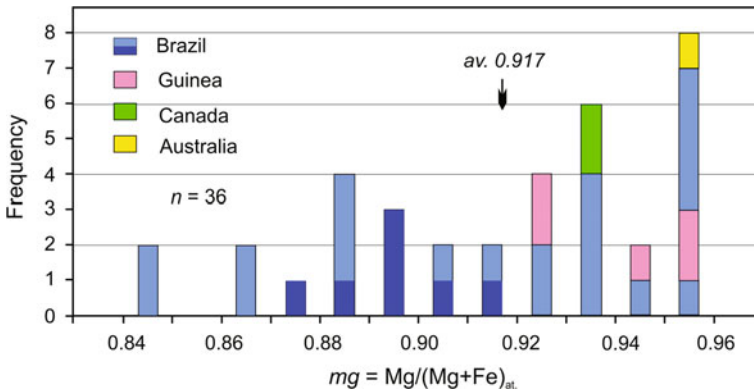
Fig. 4.3 Distribution of the magnesium index *mg* in natural bridgmanite from different areas. Data from Hutchison ([1997](#)), Stachel et al. ([2000](#)), Kaminsky et al. ([2001](#)), Davies et al. ([2004](#)), Hayman et al. ([2005](#)), Tappert et al. ([2009b](#)), Zedgenizov et al. ([2014a](#), [2015](#)), Burnham et al. ([2016](#)). *Deep blue color* indicates high-Al samples from Brazil

lowermost mantle, more Mg-rich bridgmanite was expected owing to the substantial decrease of the suggested Fe–Mg partition coefficient between bridgmanite and melt $K_D^{Brd-melt} = (Fe/Mg)^{Brd}/(Fe/Mg)^{melt}_{at.}$ from 0.25–36 GPa to 0.06–0.08 above 76 GPa, corresponding to a depth of $\sim$1800 km (Irifune et al. [2010](#); Nomura et al. [2011](#)). Similar values of $K_D^{Brd-melt}$ were experimentally established more recently: 0.329 at 34 GPa, 0.113 at 68 GPa, and 0.085 at 88 GPa (Tateno et al. [2014](#)). Much higher values of $K_D^{Brd-melt}$ were found in experiments with Al-rich, pyrolite-like glass at pressures from 40 to 120 GPa (from 0.6 to 0.45) (Andrault et al. [2012](#)), but they also show the same tendency of decrease of Fe–Mg partition, leading to crystallization of bridgmanite with higher magnesium index than the sourcing liquid.

In one of the diamonds from pipe Pandrea-2 in the Juina area, Brazil, two grains of a phase with Mg–Ca–Si composition were identified (Kaminsky et al. [2009a](#)). Conventionally, they may be attributed as a perovskite phase only, by analogy with other perovskite phases met as inclusions in diamonds from the Juina area (Harte et al. [1999](#); Kaminsky et al. [2001](#); Hayman et al. [2005](#)). The *mg* numbers of these grains are higher than usual in bridgmanite (0.966 and 0.969). The only noticeable admixture is Al; in one of the grains, Al$_2$O$_3$ = 2.04 wt% (Table [4.2](#)). Since the grains are opaque, and the two analyses show a spread, especially in Al and Ca, it is possible that the grains were originally a mixture of bridgmanite and CaSi-perovskite, and are now a fine-grained mixture due to decompression breakdown, as described by Harte and Cayzer ([2007](#)) for majoritic garnets from the Sao Luiz diamonds.

Concentration of ferric iron Fe^{3+} in bridgmanite. According to mineral physics and geochemical results, which suggest relatively low oxygen fugacity in the lower mantle, one should expect a very low (if any) concentration of ferric iron Fe^{3+} in bridgmanite. However, it has been shown that the Al admixture in

Table 4.2 Chemical compositions of Mg–Ca–Si phase from a diamond in pipe Pandrea-2, Juina area, Brazil (wt%) (Kaminsky et al. 2009a)

Sample No.	014-2a	014-2a-1
SiO_2	55.70	57.65
TiO_2	0.04	0.03
Al_2O_3	2.04	0.10
Cr_2O_3	0.01	0.02
FeO	1.01	0.90
NiO	0.09	0.07
MnO	0.06	0.08
MgO	22.50	21.89
CaO	12.64	17.56
Na_2O	0.15	0.04
K_2O	0.17	0.02
Total	94.40	98.37
mg	0.966	0.969
Reference	Kaminsky et al. (2009a)	

bridgmanite enhances the concentration of the ferric ion in the mineral even under reducing conditions. The valence states of iron in mantle minerals are typically analyzed using Mössbauer spectroscopy and/or electron energy-loss spectroscopy (EELS). It was experimentally demonstrated that the $Fe^{3+}/\Sigma Fe$ ratio may exceed 50% with the increased substitution of Al content in bridgmanite synthesized at 26 GPa (Lauterbach et al. 2000). Incorporation of ferric iron via the oxygen vacancy mechanism is not expected in bridgmanite and post-perovskite at lower-mantle conditions (Brodholt 2000). The high Fe^{3+} content in bridgmanite is enhanced by an increased Al^{3+} substitution via the charge-coupled substitution of Al for Mg and Si mechanism (McCammon 1997, 2005; Andrault et al. 2007). This means that the $Fe^{3+}/\Sigma Fe$ ratio in bridgmanite may not be caused by the oxygen fugacity conditions. However, this conclusion was challenged by the results of later experiments with Al-free bridgmanite, showing a strong dependence of Fe^{3+} incorporation in bridgmanite with f_{O_2} (Nakajima et al. 2012). Recent experiments at moderate pressure (25 GPa) and reducing oxygen fugacities (between IW-1 and IW) also demonstrated a weak correlation of Fe^{3+} content with Al content (Boujibar et al. 2016). A self-disproportionation mechanism has also been proposed to explain the co-existence of metallic iron with bridgmanite, in which Fe^{2+} disproportionates into Fe^{3+} and Fe^0, drastically increasing the amount of Fe^{3+} in the bridgmanite lattice (Frost et al. 2004).

The issue of site occupancy and valence states of iron in bridgmanite is still much debated experimentally (Shukla et al. 2015). For example, Lin et al. (2012) propose that 50% of Fe^{3+} is substituted through charge-coupled substitution in an Mg and Si site, while the remaining 50% Fe^{3+} goes in the Si site through oxygen vacancy. Hummer and Fei (2012) suggest that the ratio of Fe^{3+} in Mg and Si sites depends on total iron concentration. Hsu et al. (2012) and Sinmyo et al. (2014) concluded that all Fe^{3+} would be in an Mg site. At the same time, evidence from geological data shows that all Fe in bridgmanite exists in site A replacing Mg (Kaminsky and Lin 2017).

This was confirmed in recent high-pressure XRD experiments with single-crystal samples (Mao et al. 2017), Fe^{3+} comprises only a small share ($Fe^{3+}/\Sigma Fe$ = 9–12 at.%; Kaminsky et al. 2015b). The thermodynamic model, based on ab initio calculations, also demonstrates a very low amount of $Fe^{3+}/\Sigma Fe$ = 1–7% in Al-free bridgmanite under low-mantle conditions (Xu et al. 2015).

Concentration of Al in bridgmanite is very important. In contrast to upper-mantle enstatite, which usually shows Al_2O_3 contents of 0.3–0.9 wt% but does not exceed 1 wt%, natural bridgmanite in diamond inclusions commonly contains 1–3 wt% Al_2O_3, and in some cases this value may be up to 12.58 wt%, as observed in some samples from São Luiz in Brazil. Using the concentration of Al in bridgmanite, the studied natural samples can be clearly subdivided into two groups: low-Al and high-Al species (Fig. 4.4). Low-Al bridgmanite has 0.25–3.10 wt% Al_2O_3 (average: 1.63 wt%), while the high-Al group has 8.34–12.58 wt% Al_2O_3 (average: 10.46 wt%).

Both low-Al and particularly high-Al groups of bridgmanite show the correlation with *fe* and Fe speciation with Al substitution (Fig. 4.5a). High-pressure–temperature experiments show that significant amounts of the Fe in bridgmanite may be incorporated as Fe^{3+} depending on Al-content and, in contrast to Al^{3+}, Fe^{3+} apparently has an affinity for the 8/12-fold A site over the six-fold B site (McCammon 1997; Frost et al. 2004). The existing graph demonstrates the correlation of Al in natural bridgmanite with the total concentration of Fe.

The presence of Al enhances the ability of a perovskite structure to accept various minor and trace elements (Andrault et al. 2007; Righter et al. 2014). This explains much higher Cr concentrations in high-Al bridgmanite compared with the low-Al variety (1.16–3.14 wt% Cr_2O_3 vs. 0.04–0.45 wt% Cr_2O_3; Fig. 4.5b); some high-Al samples of bridgmanite contain high concentrations of Ca and Na as well (4.38–5.07 wt% CaO; 0.82–6.21 wt% Na_2O; Fig. 4.5c, d).
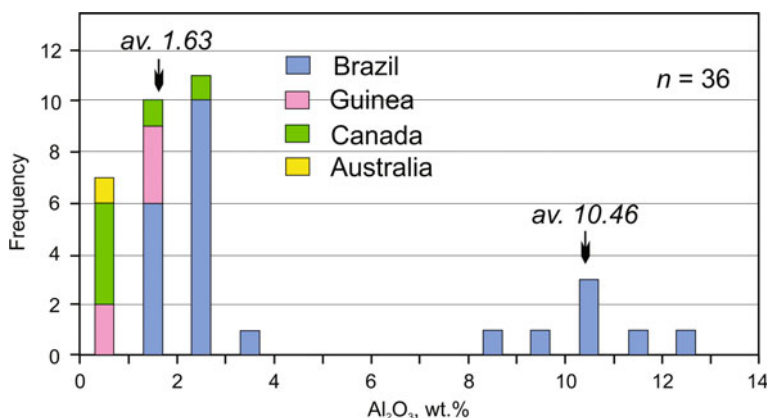
Fig. 4.4 Distribution of Al_2O_3 (wt%) in natural bridgmanite. Data from Hutchison (1997), Stachel et al. (2000), Kaminsky et al. (2001), Davies et al. (2004), Hayman et al. (2005), Tappert et al. (2009b), Zedgenizov et al. (2014a, 2015), Burnham et al. (2016)
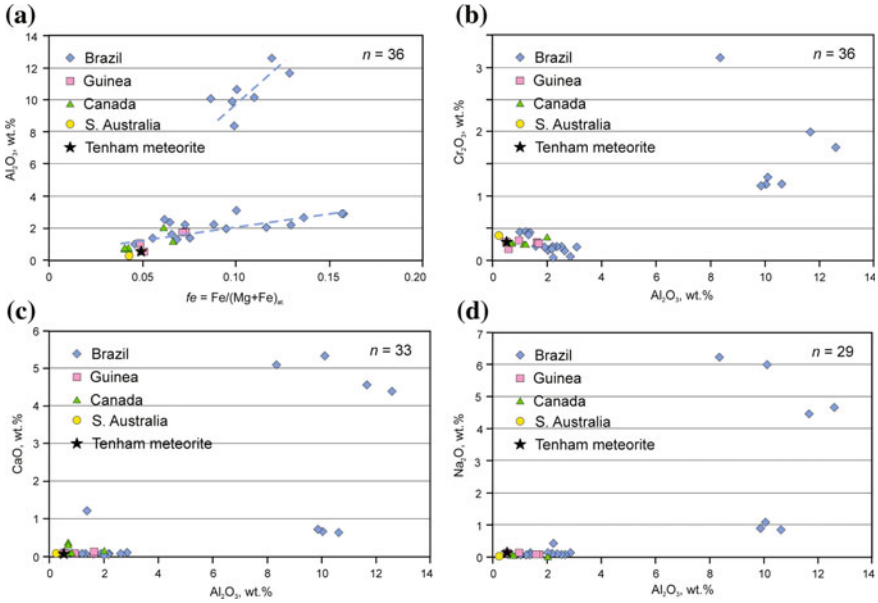
Fig. 4.5 Chemical characteristics of natural bridgmanite. **a** Al_2O_3 versus iron index *fe*; **b** Cr_2O_3 versus Al_2O_3; **c** CaO versus Al_2O_3; **d** Na_2O versus Al_2O_3. Data from Hutchison (1997), Stachel et al. (2000), Kaminsky et al. (2001), Davies et al. (2004), Hayman et al. (2005), Tappert et al. (2009b), Tschauner et al. (2014), Zedgenizov et al. (2014a, 2015), Burnham et al. (2016)

According to experimental garnet-to-perovskite transitions at c. 24–26.5 GPa pressure, in the $MgSiO_3$–Al_2O_3 system, mineral physics results indicate an increase of Al_2O_3 in bridgmanite with increasing pressure (Irifune et al. 1996; Wood 2000). For Al-free bridgmanite, the transition pressure occurs at ~23 GPa, whereas dissolution of majoritic garnet into bridgmanite can extend the transition pressure to approximately 27–28 GPa (~800 km in depth). Recently, an experimental study of the system $MgSiO_3$–Al_2O_3 under pressures of up to 52 GPa and 2000 K, with the use of sintered diamond anvils combined with in situ synchrotron X-ray diffraction observations in a multi-anvil apparatus were performed (Liu et al. 2016). This study demonstrated that the Al_2O_3 content in bridgmanite increases from 12 mol% at 27 GPa to 29 mol% at 52 GPa. These results suggest the Al_2O_3 content in bridgmanite is a good pressure indicator at pressures above 30 GPa (Liu et al. 2016). It is possible, in such a case, to find transitional compositions of natural bridgmanite.

The incorporation of Al^{3+} in bridgmanite may occur by two competing mechanisms (Richmond and Brodholt 1998; Vanpeteghem et al. 2006). The first is a Tschermak-like charge-coupled substitution (CCM) $2Al^{3+} \rightarrow Si^{4+} + Mg^{2+}$, where Al enters both pseudo-dodecahedral (A) and octahedral (B) cationic sites. The effective ionic radius of Al^{3+} lies between those of Si^{4+} and Mg^{2+} (Shannon and Prewitt 1969), and Al^{3+} substitution reduces charges of the octahedra (Al^{3+} substitutes for Si^{4+}) and increases charges in the dodecahedra (Al^{3+} substitutes for

Mg^{2+}), making local charge neutrality easier to attain. As a result, this mechanism does not require the creation of oxygen vacancies for the charge balance. In the second mechanism, Al replaces Si in the octahedral site only while oxygen vacancies are created to balance the charge: $2Si^{3+} \rightarrow 2Al^{4+} + V_O$ (OVM). In this mechanism, it is necessary to remove an oxygen ion in order to balance the charge.

Experiments performed under 26 GPa and 1973 K with the use of X-ray absorption spectroscopy (XAFS) demonstrated that the CCM substitution is preferable (Andrault et al. 1998a). Later, Stebbins et al. (2001) reported the results obtained by the use of nuclear magnetic resonance (NMR) spectra (according to which only CCM substitution was detected for the substitution mechanism of Al^{3+} into bridgmanite) and theoretical calculations also demonstrated that the CCM substitution mechanism is energetically favoured (e.g., Navrotsky et al. 2003; Akber-Knutson and Bukowinski 2004).

For high-Al bridgmanite (starting from 7.7 mol% Al$_2$O$_3$), the CCM substitution was suggested to evolve rapidly as the Al content in bridgmanite increases (Daniel et al. 2001). It was concluded that the oxygen vacancy mechanism may dominate over the coupled substitution mechanism in Al-rich bridgmanite (Daniel et al. 2004). This would be consistent with ab initio calculations by Brodholt (2000), which showed that within the experimentally investigated pressure range, oxygen vacancies are energetically favoured for a bridgmanite structure with a high Al content. Yamamoto et al. (2003) carried out first-principles density functional theory (DFT) calculations with large supercells consisting of 80 atoms and corresponding to 6.25 mol% Al$_2$O$_3$ incorporation and found that the charge-coupled substitution in bridgmanite is more favorable than the oxygen vacancies mechanism at all pressures up to 100 GPa.

The data obtained for natural assemblages demonstrate that it is possible that both mechanisms are realised: oxygen vacancy mechanism with Al replacement of Si only in site B is characteristic for low-Al bridgmanite; while, according to the mineral stoichiometry, Al-rich samples show Al^{3+} replacement in both sites, A (for Mg^{2+}) and B (for Si^{4+}).

Admixtures of minor elements in bridgmanite. In addition to Fe and Al, there are admixtures of minor elements in bridgmanite such as of Cr and Ni; Cr$_2$O$_3$ reaches 3.14 wt% (Table 4.3; Fig. 4.5b). The admixture of Na correlates with Al: high-Al bridgmanite contains 0.82–6.21 wt% Na$_2$O (Fig. 4.5d). High concentrations of Na in bridgmanite (increasing its unit-cell volume) was observed experimentally in the MgSiO$_3$–Na$_2$CO$_3$–Al$_2$O$_3$ system at 24 GPa and 1700 °C (Bindi et al. 2016). The mechanism of such incorporation remains unknown because of the lack of sufficient crystallographic data. However, these experimental results demonstrate that bridgmanite can incorporate significant concentrations of Na and possibly other alkalis in the lower mantle.

The total trace element concentrations in bridgmanite are low, usually one to two orders of magnitude below chondritic. The REE pattern is chondrite-like, but lower than in chondrite concentrations, only showing the enrichment in heavy REE and mainly in Lu (Fig. 4.6). Considering their generally low mineral/melt partition coefficient under high-pressure conditions (from c. 10^{-3} for La to c. 1 for Lu;

Table 4.3 Minor elements in bridgmanite (wt%) (from Kaminsky 2012)

Oxides	Brazil			Guinea	Canada
	Rio São Luiz (low-Al/high-Al)	Rio Vermelho	Rio Soriso	Kankan	DO27 pipe
Al_2O_3	1.23–2.86/8.34–12.58	2.16	1.60–3.10	0.55–1.68	0.69–2.03
Na_2O	0.03–0.11/0.82–6.21	0.10	0.07–0.08	0.03–0.09	0.04–0.07
Cr_2O_3	0.04–0.45/1.16–3.14	0.17	0.20–0.22	0.17–0.29	0.23–0.36
NiO	0.01–0.03/0–0.02	<0.06	n.d.	0.01–0.02	n.d.
mg	0.843–0.945/0.871–0.913	0.870	0.900–0.938	0.927–0.951	0.934–0.960
References	Wilding (1990), Harte et al. (1999)	Kaminsky et al. (2001)	Hayman et al. (2005)	Stachel et al. (2000)	Davies et al. (2004)

Note: *n.d.* not detected
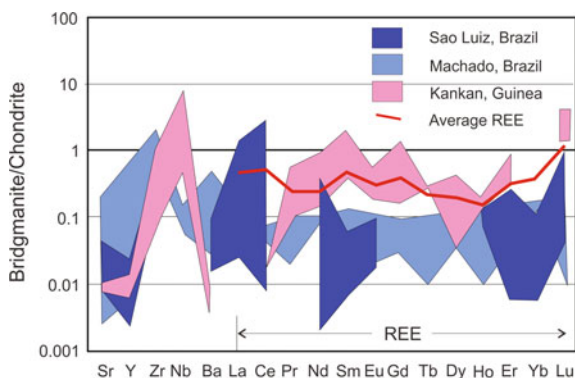
Fig. 4.6 Chondrite-normalized trace element patterns in bridgmanite. Data from Harte et al. (1999), Stachel et al. (2000) and Burnham et al. (2016). Chondrite composition here and in the other spider-diagrams (Figs. 3.10, 3.22, 3.32, 3.34, 3.37 and 3.39) are taken from McDonough and Sun (1995). Modified after Kaminsky (2012), with additions

Thomson et al. 2016), such concentrations indicate the primary origin of the analyzed bridgmanite grains, with the subsequent trapping of them from pristine ambient mantle by host diamonds. One should expect the increase of trivalent and tetravalent cations of trace elements entering the A-cite in Al-rich bridgmanite because of their high crystal-liquid partition coefficients (Wood and Corgne 2009). However, there is currently not enough data on this subject.

Water in bridgmanite. Bridgmanite can also accommodate a certain amount of water (hydroxyl), which may play a role in affecting the physical and chemical properties of the mineral in the lower mantle. From analysis of FTIR spectra at ambient conditions taken from bridgmanite that was synthesized at 25–26 GPa in a multi-anvil apparatus, the solubility of water in pure bridgmanite is ∼100 ppm

H₂O, while in Al-rich bridgmanite it increases up to 1000–1500 ppm (Litasov et al. 2003). In LHDAC experiments, bridgmanite was suggested to contain about 0.2 wt % H₂O (Murakami et al. 2002). With the use of first-principles methods, Hernández et al. (2013) suggested that pure bridgmanite can contain as much water as 1000 ppm.

It has been proposed that water can enter into the bridgmanite structure with oxygen vacancies originating from the substitution of Si by Al, potentially making this mineral the major storage for water in deep mantle (Daniel et al. 2001; Merli et al. 2016). $V_{si}(H_4)$ cation-vacancy complexes, in which four protons are placed at the site of a Si vacancy, were found most stable in the perovskite structure. Other polyvalent substitutions (e.g., $Na^{1+} \rightarrow Mg^{2+}$) can also favour the origin of $V_{Mg}(H_2)$ oxygen vacancies and subsequently water incorporation in bridgmanite (Hernández et al. 2013). Townsend et al. (2016) suggested a possibility of hydrogen incorporation for Al-free bridgmanite without oxygen-vacancy formation with the so-called "Mg–2H mechanism": $Mg^{2+} \leftrightarrow 2H^+$.

During the course of bridgmanite → post-perovskite structural transformation, water favours bridgmanite over post-perovskite by a factor of about 5:1 for Al-free system; in the Al-bearing system, in reverse, water favours post-perovskite over bridgmanite by a factor of about 3:1 at ambient mantle conditions (see Sect. 9.2.2).

4.2.3   Crystal Structure of Bridgmanite

Structure. Initially, the crystal structure of bridgmanite was suggested to be cubic with the lattice parameter $a = 3.426 \pm 0.006$ Å (Reid and Ringwood 1975). The *d*-spacing of the first synthesized 'MgSi-perovskite', however, was indexed as an orthorhombic perovskite structure (space group *Pbnm*) with $a = 4.818 \pm 0.005$ Å, $b = 4.869 \pm 0.005$ Å, and $c = 6.906 \pm 0.007$ Å with $Z = 4$ (Liu 1974) (Fig. 4.7). The bridgmanite sample from the Tenham meteorite has the orthorhombic *Pnma* perovskite structure with unit cell parameters $a = 5.02 \pm 0.03$ Å, $b = 6.90 \pm 0.03$ Å, $c = 4.81 \pm 0.02$ Å, and a unit cell volume of 167 ± 2 Å³ (Tschauner et al. 2014). The space group *Pnma* is equivalent to *Pbnm*, with the following conversion: $(a, b, c)_{Pnma} \rightarrow (b, c, a)_{Pbnm}$ (Wicks and Duffy 2016). Deviation from the ideal cubic arrangement is achieved through both rotation and tilting of the SiO_6 octahedra and the offset in position of the central Mg atom (Horiuchi et al. 1987). These structural distortions increase with increasing pressure (Fiquet et al. 2000). Addition of Al in the bridgmanite structure also increases the orthorhombic distortion (Kojitani et al. 2007; Walter et al. 2004a), while substitution of Fe^{2+} for Mg^{2+} in the A site of perovskite expands the structure and decreases the degree of distortion (Kudoh et al. 1990).

Phase transitions in bridgmanite. The possibility of phase transitions in bridgmanite has been debated for decades. Early high-pressure XRD measurements on temperature-quenched samples by Knittle and Jeanloz (1987) demonstrated the stability of bridgmanite up to 127 GPa. However, later studies reported its
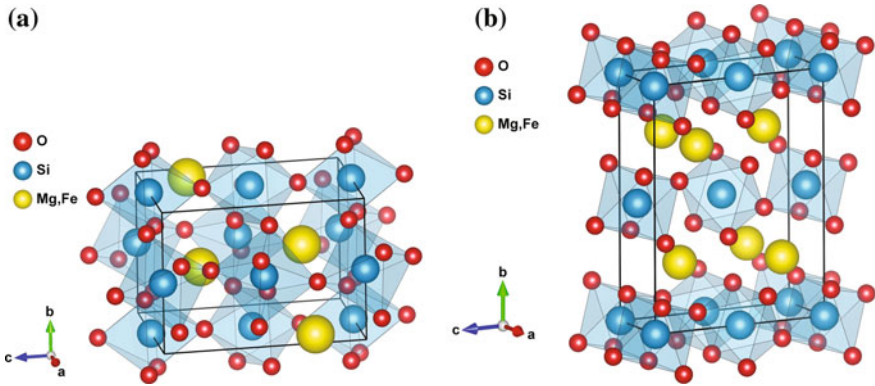
Fig. 4.7 Orthorhombic crystal structures of bridgmanite in the *Pbnm* space group (*left*) and post-perovskite in the *Cmcm* space group (*right*). Tilting of the SiO_6 octahedra results in the shortening of crystallographic axis and produces a displacement of Mg,Fe cations reducing the co-ordination from 12 (characteristic for the ideal cubic perovskite structure) to 8. *Thick lines* outline the unit cell. Lattice parameters for bridgmanite taken from Sugahara et al. (2006); for post-perovskite from Zhang et al. (2014)

dissociation into MgO and SiO_2 during the course of laser heating (temperature was not measured) at 60–70 GPa (Meade et al. 1995), at 58–100 GPa and 1900–3000 K (Saxena et al. 1996), or at 82 GPa and 1140–1250 K (Saxena et al. 1998). These conclusions appeared to be a result of technical issues, possibly because of extreme temperature gradients during the experiments and reactions between the pressure medium and samples. The several experimental studies that followed used inert pressure mediums and in situ XRD (Fiquet et al. 2000; Andrault et al. 2001; Shim et al. 2001; Ono et al. 2004). Raman measurements (Serghiou et al. 1998) have indicated the stability of orthorhombic *Pbnm* $MgSiO_3$ to pressures of 100–106 GPa. Shim et al. (2001) reported a subtle phase change of bridgmanite from *Pbnm* to one of three possible space groups, $P2_1/m$, *Pmmn*, or $P4_2/nmc$ above 83 GPa and 1700 K, but this was not confirmed by later studies. Recently, the dissociation of Fe-bearing perovskite was reported by Zhang et al. (2014). They found that in LHDAC experiments within the pressure interval of 95–101 GPa and temperatures of 2200–2400 K bridgmanite with the *mg* = 85 disproportionates into almost iron-free bridgmanite and an iron-rich phase with a hexagonal structure, named H phase, using XRD analysis. It should be cautiously noted that such a dissociation has not yet been confirmed by other groups who have tried to reproduce the study, although an analogous dissociation of ferropericlase into almost pure wüstite and an Mg-rich phase at 86 GPa and 100 K was obtained experimentally (Dubrovinsky et al. 2000, 2001a) and was observed in lower-mantle inclusion in diamond from the Soriso area, Brazil (Kaminsky et al. 2015a).

Since most scientists had believed that perovskite is stable at lower-mantle pressure–temperature (*P–T*) conditions, by the early 2000s most groups did not pursue higher-pressure experiments on the stability of perovskite toward the core–

mantle boundary conditions (the D″ layer up to 136 GPa and ∼3500 K). Interestingly, a first-order solid phase transition was proposed by a group of seismologists (Sidorin et al. 1999) to exist approximately 200 km above the core–mantle boundary (the D″ region) with a Clapeyron slope of approximately 6 MPa/K. The occurrence of such a structural transition can explain most of the observed seismic variations in travel times and the spatial intermittance of the seismic triplication (Sidorin et al. 1999). It was not until 2004 that the transition of bridgmanite to silicate post-perovskite was discovered experimentally and theoretically to occur at pressure–temperature conditions of the D″ region (Murakami et al. 2004a) (see Sect. 9.2.2). In 2004, after experiments reaching higher P–T parameters, corresponding to the D″ layer conditions, the post-perovskite crystal structure was observed at 113–125 GPa and 2200–2500 K with the use of LHDAC and in situ XRD (Murakami et al. 2004a, 2005; Oganov and Ono 2004; Tsuchiya et al. 2004b). According to first-principle computations, it has another orthorhombic, the CaIrO$_3$ structure with the *Cmcm* space group (Tsuchiya et al. 2004b).

In post-perovskite, Si^{4+} and Mg^{2+} have the same coordination environment as in bridgmanite, but there are profound differences in their structural arrangement. In contrast to the corner-sharing network in bridgmanite, the SiO$_6$ octahedra in post-perovskite share edges along the *a* axis and corners along c. The structure is thus sheet-like with layers of SiO$_6$ octahedra alternating with MgO$_8$ layers along the *b* axis (Fig. 4.7b). The Mg sites in post-perovskite are smaller and less distorted than those in bridgmanite, resulting in a volume reduction of ∼1–1.5% across the transition (Wicks and Duffy 2016).

The phase boundary between *Pbnm* and *Cmcm* phases has a Clapeyron slope of ∼7.5 ± 0.3 MPa/K at ∼2750 K and ∼125 GPa (Tsuchiya et al. 2004b) or 13–16 MPa/K at 3750 K (Li et al. 2015 and references therein) (see Fig. 9.2).

The concentration of iron suppresses the stability of bridgmanite, which was supported in early experiments (e.g., Fei et al. 1996). Dorfman et al. (2013), using double-sided LHDAC with in situ XRD, demonstrated that iron-rich bridgmanite (with fe > 0.35–0.40) decomposes into low-Fe Brd + fPer + SiO$_2$ at pressures below 70 GPa. In natural samples analyzed to date, maximal concentrations of FeO in bridgmanite reach 10.4 wt% (fe = 0.157); they do not experience such decomposition.

4.2.4   Physical Properties

The role of the chemical composition of bridgmanite. A series of experiments and theoretical calculations have been conducted on the role of the Fe and/or Al incorporation in the bridgmanite on physical properties (Zhang and Weidner 1999; Brodholt 2000; Kubo et al. 2000; Daniel et al. 2001, 2004; Andrault et al. 2001, 2007; Yamamoto et al. 2003; Jackson et al. 2004; Walter et al. 2004a; Yagi et al. 2004; Akber-Knutson and Bukowinski 2004; Gu et al. 2016), but these results have

been extensively debated and remain reconciled. For example, the substitution of Fe in bridgmanite inherently increases its density significantly because the iron ion is much heavier than the magnesium ion; however, the lattice parameters are not expected to change substantially because of their similar ionic radii. Substitution of Fe^{3+} at the A site would be preferred at a high iron content coupled with Mg vacancies and would lead to a significant distortion of the dodecahedral site. Thus, substitution of Fe^{3+} would diminish the density increase compared with the same amount of Fe^{2+} substitution. Analogically, Al incorporation into the bridgmanite structure increases the cell volume (Daniel et al. 2004; Yagi et al. 2004)

Recently, Fukui et al. (2016) studied the role of cation substitution on bridgmanite elasticity at ambient conditions and concluded that substitution of Mg with Fe^{2+} and Al influences the anti-correlation between bulk sound velocity and shear velocity. At the same time, it was shown that the effect of Fe^{3+} concentration on the bulk modulus of bridgmanite is not significant for lower-mantle pressures (Gu et al. 2016).

Volume. Independently of the composition of bridgmanite, its volume significantly (by ∼13%) decreases with increasing pressure from 30 to 90 GPa, at room temperature (Gu et al. 2016).

Elastic properties. In general, the addition of Fe in bridgmanite can cause an increase in the density, bulk modulus, and bulk sound velocity independently on the Al concentration at lower-mantle pressures. The analysis of the EoS parameters of bridgmanite at lower-mantle pressures, obtained in low-Fe (*fe* = 0.06–0.11) single-crystal samples in a hydrostatic He medium, indicates that the substitution of iron in bridgmanite will cause an anti-correlation between the enhanced density and reduced bulk sound velocity (V_Φ), whereas the combined Al and Fe substitution has a reduced effect on density and a negligible effect on V_Φ (Mao et al. 2017). In experiments with high-Fe bridgmanite the increase in concentrations of iron (*fe* = 0.25) increases the density and bulk sound velocity (V_Φ) of bridgmanite by 4–6 % and 6–7 % respectively at lower-mantle pressures (Mao et al. 2011). The presence of Fe^{3+} in the B-site of bridgmanite (if happens) can further enhance this increase (Mao et al. 2015). However, this data may not be related to natural bridgmanite because in natural samples the concentrations of Fe are significantly smaller (*fe* = Fe/(Mg + Fe)$_{at}$ = 0.04–0.16).

The role of Al seems more complex; the experimental results are controversial. Based on experiments in cubic-anvil apparatus, Zhang and Weidner (1999) reported that bridgmanite with only 5 mol% Al_2O_3 might have a bulk modulus K_T 10% lower than pure bridgmanite, showing that the addition of aluminium can drastically decrease the incompressibility of bridgmanite. Such a large effect on the K_T of bridgmanite, resulting from a relatively low concentration of Al, has also been reported in DAC experiments with higher Al contents (up to 7.7–10.3 mol% Al_2O_3) (Kubo et al. 2000; Daniel et al. 2001). However, later XRD experimental studies performed at lower-mantle pressure conditions in a DAC showed that the K_T of aluminous bridgmanite is, in reverse, higher than that of pure bridgmanite, and hence, dissolution of Al makes it even more incompressible than pure $MgSiO_3$ (Andrault et al. 2001). In another publication, Daniel et al. (2004) demonstrated, on

the basis of monochromatic synchrotron XRD from bridgmanite with 5 mol% Al$_2$O$_3$, that its bulk modulus K_T is decreased under pressure conditions of up to 40 GPa only by 1.8% at most, i.e., it is affected little if at all by the presence of Al^{3+}. Daniel et al. (2004) suggested that the relative proportions of the minerals characteristic of the lower mantle, as inferred from seismological models, are unlikely to be significantly altered by the introduction of Al in the system.

However, the experiments performed in DAC by Yagi et al. (2004) again confirmed the results made by Zhang and Weidner (1999), Kubo et al. (2000) and Daniel et al. (2001), and were opposite to the results obtained by Andrault et al. (2001). The results of experiments performed by Yagi et al. (2004) in DAC at pressures of up to 33 GPa have shown that the dissolution of Al$_2$O$_3$ into MgSiO$_3$ decreases the bulk modulus considerably. This effect is highly nonlinear with Al$_2$O$_3$ content; the bulk modulus decreases by as much as 7% with only 1% Al$_2$O$_3$. Walter et al. (2004a) found in their experiments a decrease in bulk modulus of bridgmanite with the addition of Al in its structure; however, they found this decrease to be "mild" and established its rate at -67 ± 35 GPa/X$_{Al}$. The general results of major experiments on the elastic properties of bridgmanite under high-pressure conditions are summarized in Table 4.4.

The discrepancies between the different series of experiments may be caused by sample chemistries and/or technical problems, including experimental P–T conditions, pressure medium and calibrant, starting sample conditions, P–T effects on solubility of cations, and types of stable defects at high P–T conditions (Yagi et al. 2004; Walter et al. 2004a). For example, the amorphization of bridgmanite can occur in response to grinding the sample by mortar and pestle under atmospheric pressure, or by heating to above 400 K at atmospheric pressure (Yagi et al. 2004). Use of such a sample would cause problematic results at high pressures. The experiments performed by Walter et al. (2004a) demonstrated that Al^{3+} substitution increases orthorhombic distortion and unit cell volume, which causes a decrease in K_{0T} at a rate of $\sim 67 \pm 35$ GPa/X$_{Al}$ and, as a result, a mild increase in compressibility. This relatively mild increase in compressibility is in good agreement with theoretical calculations if Al^{3+} substitutes into the bridgmanite structure by means of a charge-coupled substitution mechanism ($2Al^{3+} \rightarrow Si^{4+} + Mg^{2+}$). By contrast, the much lower incompressibility for aluminous bridgmanite measured in several other studies is consistent with Al^{3+} substitution by oxygen-vacancy formation ($2Al^{3+} \rightarrow 2Si^{4+} + O^{2-}_V$). The formation of vacancies in the structure of bridgmanite caused by the latter mechanism makes the concentration of vacancies increase in proportion to the Al concentration. At a low concentration, the vacancies are randomly distributed; above a certain concentration threshold, they are ordered, as shown by Becerro et al. (1999), for Fe in solid solution between CaTiO$_3$ (perovskite) and Ca$_2$Fe$_2$O$_5$ (brownmillerite). The formation of vacancies can decrease the incompressibility considerably. Brownmillerite, for example, is approximately 25% more compressible than expected from the systematics of unit cell volume versus bulk modulus relation in bridgmanite (Ross et al. 2002). Brodholt (2000) made theoretical calculations for (Mg$_3$Al)(AlSi$_3$)O$_{12}$ perovskites and Mg$_2$Al$_2$O$_5$

Table 4.4 Results of major experiments on elastic properties of bridgmanite under high pressure conditions

References	Method	Conditions	Al_2O_3 mol%	Results
Zhang and Weidner (1999)	Multi-anvil No medium	1–10 GPa	5.0	Brd with 5 mol% Al_2O_3 has a bulk modulus K_T 10% lower than pure Brd
Kubo et al. (2000)	DAC Medium: Alcohol mixture	1–9 GPa	10.3	Same
Daniel et al. (2001)	DAC Medium: Ar, He Synchrotron XRD	1–32 GPa	7.7	Same Al^{3+} is likely to be incorporated in place of Si^{4+} in the octahedral site of Brd, hence requiring the creation of oxygen vacancies for charge balance. As a consequence, Al-Brd may have a high affinity for water
Andrault et al. (2001)	LHDAC Medium: Ar Monochromatic synchrotron XRD	29–57; 29–69 GPa	5.0; 11.0	Opposite Al increases bulk modulus K_T of Brd in comparison to that of pure Brd; i.e., dissolution of Al makes Brd even more incompressible than pure Brd
Daniel et al. (2004)	DAC Medium: Ne Monochromatic synchrotron XRD	Up to 40 GPa Ambient temperature	5.0	K_T is affected little if at all by the presence of Al^{3+}. Hence, seismological models should not be significantly altered by the introduction of Al in the system
Jackson et al. (2004)	Multi-anvil Brillouin spectroscopy	∼25 GPa, 1873 K	5.1 ± 0.2	The presence of 5.1 wt% does not affect bulk modulus and decreases the shear elastic modulus (μ) by 5.6%
Yagi et al. (2004)	LHDAC Medium: He Synchrotron XRD	2–33 GPa	1–10	The dissolution of Al_2O_3 into Brd decreases the bulk modulus considerably. The effect is highly nonlinear with Al_2O_3 content; the bulk modulus decreases by 7% with only 1% Al_2O_3
	Multi-anvil cell No medium	17–23 GPa.	0–5	The dissolution of Al_2O_3 does not decrease the bulk modulus of Brd
Walter et al. (2004a)	LHDAC Medium: KBr In situ angle-dispersive XRD	30–100 GPa 2000–2600 K	0–25	Al^{3+} substitution causes a mild decrease in bulk modulus K_0 at a rate of -67 ± 35 Ga/X_{Al}
Andrault et al. (2007)	LHDAC Medium: Ar	Up to 60 GPa. 2300 K	0–5	Al–Brd synthesized in the SiO_2-rich system is more compressible than Al–Brd synthesized in the MgO-rich system

(continued)

Table 4.4 (continued)

References	Method	Conditions	Al$_2$O$_3$ mol%	Results
Mao et al. (2011)	LHDAC Medium: Ne Synchrotron XRD	Up to 135 GPa. 1300–1600 K	0; 0–25 Fe	The isothermal bulk modulus of Brd with 25% FeSiO$_3$ is $\sim$20% larger at high pressures than that of the pure Brd
Mao et al. (2015)	LHDAC Medium: Ne In situ synchrotron XRD	30–125 GPa	10 Fe	The addition of Fe causes an increase in the density, bulk modulus, and bulk sound velocity in both Al-free and Al-bearing bridgmanite at lower-mantle pressures. The presence of Fe^{3+} in the B-site of bridgmanite can further enhance this increase
Mao et al. (2017)	LHDAC Medium: Ne Synchrotron XRD and Mossbauer spectroscopy	Up to 130 GPa	1–11; 6–11 Fe	The substitution of Fe in Brd causes an anti-correlation between the enhanced density and reduced bulk sound velocity (V_Φ), whereas the combined Al and Fe substitution has a reduced effect on density and a negligible effect on V_Φ

Notes: *Brd* bridgmanite, *DAC* diamond-anvil cell, K_T bulk modulus, *XRD* X-ray diffraction

with the brownmillerite structure. He showed that the bulk modulus of (Mg$_3$Al) (AlSi$_3$)O$_{12}$, which forms by the charge-coupled mechanism and contains no vacancies, is approximately 6% smaller than that of pure bridgmanite. On the other hand, in Mg$_2$Al$_2$O$_5$, in which 1/6 of the oxygen sites are vacant, the bulk modulus is approximately 40% lower than that of pure MgSiO$_3$. With regards to aluminous bridgmanite, there have been extensive considerations concerning the dominant substitution mechanism, while experimental results have suggested that at least some vacancies are formed by the dissolution of alumina. However, on the basis of this idea alone, it is difficult to explain the large drop in the bulk modulus (7%) for the sample with only 1% Al$_2$O$_3$ because the maximum concentration of vacancies, expected from this composition, is very small (Yagi et al. 2004).

In addition, most of the experimental studies of bridgmanite elasticity have been performed in static compression experiments using XRD in a DAC, which yield the isothermal bulk modulus (K_T) through modeling the pressure–volume relationship. The EoS, using Birch-Murgnahan EoS Brillouin Light Scattering (BLS), is a powerful technique to measure the sound velocities of the mantle samples and to derive elasticity, including single-crystal elastic constants at high pressures in a DAC (Bass 2008). This method, using the measured V_p and V_s velocities (from Brillouin) and density (from diffraction and chemical analysis), provides a direct means of determining the adiabatic bulk modulus (K_S) that is quite different in methodology from the static compression pressure–volume methods

that give the K_T based on EoS modeling (Bass 2008). The sound velocity of the same sample of bridgmanite used by Daniel et al. (2004), which had almost the same Al content (5.1 mol% Al_2O_3), was investigated using Brillouin spectroscopy at ambient conditions by Jackson et al. (2004). The performed Brillouin scattering measurements in bridgmanite under room P–T conditions demonstrated the lack of a reduction in bulk modulus K_S caused by the presence of 5.1 wt% of Al_2O_3; that is, they did not support an increase of the bulk modulus with increasing Al content. The presence of 5.1 wt% of Al_2O_3 is also shown to decrease the shear elastic modulus (μ) by 5.6% compared with Al-free bridgmanite samples (Jackson et al. 2004). Based on the Brillouin results, the end-member polycrystalline pure $MgSiO_3$ bridgmanite exhibits K_S = 253(3) GPa and μ = 175(2) GPa, which are 4 and 1% lower, respectively, than the commonly accepted values (K_S = 264 GPa, μ = 177 GPa) (Sinogeikin et al. 2004).

Static first-principles DFT, as well as atomistic calculations, in general, confirm the experimental data on the decrease of bulk modulus with the incorporation of Al in bridgmanite (Brodholt 2000; Yamamoto et al. 2003; Akber-Knutson and Bukowinski 2004). They have demonstrated that the dissolution of Al^{3+} into bridgmanite should increase its compressibility. Later lattice dynamic methods found no effect of the Al incorporation on thermodynamic properties of bridgmanite (Tsuchiya and Wang 2013).

This means that, despite some contradictions in high-pressure experimental results, one may suggest a decrease in bulk modulus of bridgmanite with the incorporation of Al in its structure, i.e. a decrease in incompressibility of the mineral. This effect seems weak, and thus should be not significant for seismologic interpretations. However, this problem needs further study.

Ferroelasticity. It is known that many distorted perovskite samples exhibit ferroelastic behavior, in which acoustic velocity, thermal expansio, and heat capacity show large anomalies near the phase transitions to higher symmetric structures (Carpenter and Salje 1998). However, bridgmanite has been shown to be far from a ferroelastic phase transformation by both theory (Karki et al. 2001; Oganov et al. 2001; Shim et al. 2001) and experiments (Stixrude and Cohen 1993; Wolf and Jeanloz 1985; Wentzcovitch et al. 1995).

Thermoelasicity. Experimental data on the thermoelasticity of bridgmanite is scarce (Murakami et al. 2012) and the uncertainty could be largely due to technical issues relating to the extreme conditions. Currently, there is only theoretical elastic constants data available for the extended P–T range of the lower mantle. In recent years, there have been several theoretical studies on the effects of ferrous and ferric iron on the thermoelastic properties of bridgmanite and post-perovskite (Metsue and Tsuchiya 2011; Tsuchiya and Wang 2013; Shukla et al. 2015); however, an agreement with seismological models of the lower mantle has not been reached. One potential reason is that the influence of Al^{3+} has not yet been included in calculations, another reason could be related to the possible inadequacy of using the quasi-harmonic approximation (QHA) in computing thermoelasticity at high P–T levels. There has been one study that used density functional molecular dynamics (DFT-MD) to calculate the properties of bridgmanite and post-perovskite enriched

with ferrous iron (Muir and Brodholt 2015); however, it calculated values at only one pressure, exceeding the bridgmanite stability field (136 GPa). Recently, calculations with the use of ab initio molecular dynamics elastic and seismic properties of pure, Fe^{3+}-, Fe^{2+}-, and Al^{3+}-bearing bridgmanite and post-perovskite over a wide range of pressures (up to 137 GPa), temperatures and Fe/Al compositions were performed, in which the high-spin Fe^{3+} and Fe^{2+} in various possible spin states and compositions were considered (Zhang et al. 2016a). The results demonstrated that a mineral assemblage resembling pyrolite (neglecting some phases, such as $CaSiO_3$) fits a 1D seismological model well, down to at least the top of the D″ layer (Zhang et al. 2016a).

Thermal and electrical conductivity. Ohta et al. (2017) experimentally demonstrated that bridgmanite (and post-perovskite) is the best heat conductor in the Earth's lower mantle, while the electronic thermal conduction in ferropericlase is negligible.

Electrical conductivity of bridgmanite has the general increase with temperature (Deschamps and Khan 2016). The increase of the Fe^{3+} iron content in aluminous bridgmanite makes an electrical conductivity greater than that of an Al-free bridgmanite. In experiments at 25 GPa and 1400–1600 °C, bridgmanite with $fe = 0.085$ containing 2.89 wt% Al_2O_3 has an electrical conductivity approximately 3.5 times greater than that of Al-free bridgmanite with the same iron index (Xu et al. 1998). Further experiments on Al-bridgmanite with $fe = 0.010$ under 26–28 GPa pressure and up to 2000 K temperature confirmed the significant increase in its electrical conductivity with respect to the quantity of Al and established the increase of the electrical conductivity with the increase of iron content in bridgmanite (Yoshino et al. 2016). The resulting conductivity of Al-bearing bridgmanite first increases up to 0.06 Al atoms per formula unit and then remains constant or increases with increasing Al content at higher temperatures. These results are in agreement with the observed 1D conductivity-depth profiles from the Earth's surface to the deep mantle, which have shown that conductivity (σ) increases from 10^{-3} to 10^0 S/m with increasing depth from 500 up to 1000 km and becomes constant at greater depths (Civet et al. 2015).

4.3 Periclase–Wüstite Solid Solution Phases (Mg,Fe)O

4.3.1 General

According to experimental and theoretical data based on the pyrolite composition, another abundant mineral in the lower mantle is ferropericlase, which should comprise approximately 16–20 wt% of the lower mantle (Irifune 1994; Fei and Bertka 1999; Wood 2000; Irifune et al. 2010) (Figs. 2.2 and 2.3). However, ferropericlase grains included in deep-mantle diamond inclusions account for 50–56% of all identified lower-mantle inclusions and are more frequently found than bridgmanite, which is believed to be the most abundant mineral, accounting for
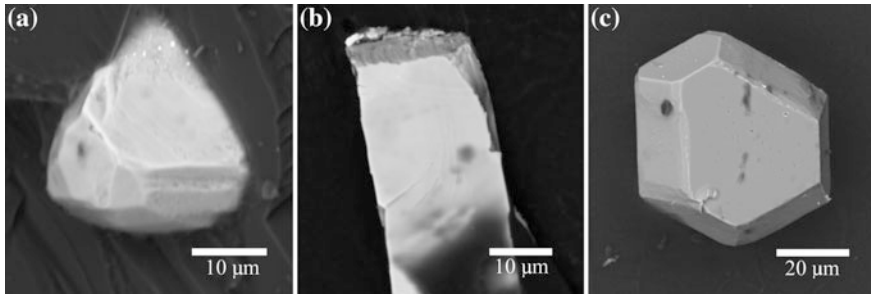
Fig. 4.8 Grains of ferropericlase extracted from diamonds of the Rio Soriso area, Brazil. SEM image. From Hayman et al. (2005)

75% of the region. Compositionally, these ferropericlase grains occupy a much wider range in FeO content than what is expected for ferropericlase, with approximately 20% FeO in the pyrolite model; some of these grains even contain more than 50% FeO and should be referred to as magnesiowüstite. These yellow-orange small (<1 mm) grains are usually euhedral with octahedral, cubic or cubic-octahedral crystal habit that reflects the rocksalt crystal structure of the lattice (Fig. 4.8). Their occurrences are either as single inclusions in diamond or form associations with bridgmanite, $CaSiO_3$ perovskite, stishovite (SiO_2), jeffbenite (formerly called TAPP), a phase with the composition of olivine, chrome spinel, ilmenite and native nickel (Kaminsky 2012 and references therein).

4.3.2 Chemical Composition of Natural (Mg,Fe)O

Representative chemical analyses of the chemical composition of ferropericlase–magnesiowüstite seria (which, for short, we refer to as 'ferropericlase') are presented in Table 4.5.

Magnesium index. According to high P–T experimental results in pyrolitic systems in the pressure range 25–60 GPa, the magnesium index of ferropericlase in lower-mantle material with $mg = Mg/(Mg + Fe)_{at.} = 0.80$–$0.95$ should be 0.73–0.88 (e.g. Wood 2000; Lee et al. 2004, Irifune et al. 2010). In the lower mantle with the most likely lower-mantle magnesium index of $mg = 0.89$–0.92, the magnesium index of ferropericlase would lie within a much narrower range, at c. 0.90 (Kesson and Fitz Gerald, 1991). However, lower-mantle geological samples of ferropericlase grains that originated from different regions of the lower mantle varied in iron contents from a 'normal' iron index to more iron-rich compositions with $mg = 0.36$–0.90 (Fig. 4.9); one of the analyzed samples had a magnesium index as low as 0.16 (Zedgenizov et al. 2014a), which is close to the end-member wüstite stoichiometry. Interestingly, this range is very similar to the compositional ranges of olivine and low-Ca pyroxene in anhydrous interplanetary dust particles ($mg = 0.46$–1.00), which represents the entire solar protoplanetary disk (Flynn et al. 2016).

Table 4.5 Representative compositions of ferropericlase-magnesiowüstite inclusions in diamond from different areas (wt%)

Country	Brazil				Machado	Canada	Guinea	Australia
Area	Juina	Sao Luiz placer		Rio Soriso placer	Machado placer	Northwest Territories	Placer	Orroroo
Location	Collier-4 pipe					DO27 pipe	Placer	Dyke Eurelia K7
Sample No.	C-18	BZ207B	BZ66	3-2G	P15-1	DO2700100	KK-16a	FBS5-11
Mineral association	fPer	fPer + Brd + Jbn	fPer	fPer + Brd + CaSiPrv + 'Ol' + Jbn	2fPer + Brd + Dol	fPer + Brd + CaSiPrv + SiMg	2fPer + Brd + Sid	6fPer + Brd
SiO_2	0	0.03	0.01	0.08	0.07	0	0.02	0.02
TiO_2	0	0.02	0.01	n.a.	<0.02	n.a.	0.00	0.02
Al_2O_3	0.01	0.11	0.13	n.a.	0.06	n.a.	0.01	0.00
Cr_2O_3	0.25	0.51	1.06	0.35	0.69	0.67	0.49	0.14
FeO	22.91	43.14	73.56	24.67	19.44	16.80	22.47	23.78
NiO	1.48	0.90	0.10	1.36	0.16	1.13	1.42	1.16
MnO	0.16	0.43	0.80	0.22	1.11	0.19	0.18	0.14
MgO	75.55	54.84	23.13	72.41	79.07	81.60	75.20	73.96
CaO	0	0.01	0.01	n.a.	0.01	n.a.	0.00	0.01
Na_2O	0.03	0.14	1.05	0.18	0.03	0.26	0.12	0.00
K_2O	0	0.01	0	n.a.	<0.02	n.a.	0.00	0.00
P_2O_5	n.a.	n.a.	n.a.	n.a.	n.a.	n.a.	0.01	0.00
Total	100.39	100.14	99.86	99.27	100.64	100.65	99.93	99.23
fe	0.145	0.306	0.641	0.160	0.121	0.103	0.143	0.153
mg	0.855	0.694	0.359	0.840	0.879	0.897	0.857	0.847
References	Kaminsky et al. (2009b)	Hutchison (1997)		Hayman et al. (2005)	Burnham et al. (2016)	Davies et al. (2004)	Stachel et al. (2000)	Tappert et al. (2005a)

Notes: *n.a.* not analysed, *Brd* bridgmanite, *CaSiPrv* CaSi-perovskite, *Dol* dolomite, *fPer* ferropericlase, *Jbn* jeffbenite, '*Ol*' phase with a composition of olivine, *Sid* siderite, *SiMg* phase with a Si–Mg composition
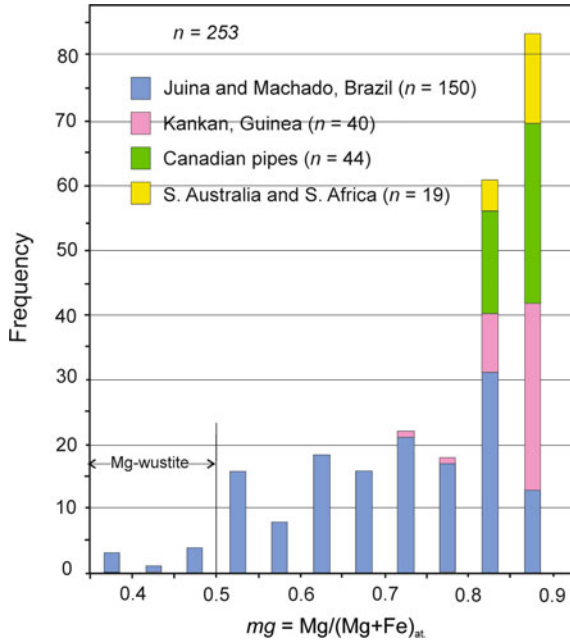
Fig. 4.9 Distribution of magnesium index *mg* in ferropericlase-magnesiowüstite inclusions in diamond. Data from Scott Smith et al. (1984), Moore et al. (1986), Wilding (1990), Hutchison (1997), Stachel et al. (2000), Hutchison et al. (2001), Kaminsky et al. (2001, 2009b), Davies et al. (2004), Hayman et al. (2005), Tappert et al. (2005a, 2009a), van Rythoven and Schulze (2009), Thomson et al. (2014), Zedgenizov et al. (2014a), Burham et al. (2016). Modified after Kaminsky (2012), with additions

There are systematic differences in ferropericlase *mg* values from different regions. Ferropericlase grains from Canada, South Australia and South Africa have *mg* in the range of 0.80–0.90, close to the expected values, while ferropericlase from Guinea, along with similar *mg* values, may show *mg* values as low as 0.75. On the other hand, almost half of all ferropericlase grains from Brazil (c. 46.5%) are iron-rich; their compositions may be magnesiowüstite. It has been suggested that such great deviations may reflect the compositional variations of bridgmanite, from which iron-rich ferropericlase and SiO_2 were formed as a result of decomposition (Fei et al. 1996; Harte et al. 1999). However, this model, while potentially explaining one discrepancy, actually raises another, that is: how can highly iron-rich bridgmanite be in equilibrium in the lower mantle whose bulk *mg* = 0.80–0.95? Liu (2002) proposed a model that involves the decarbonation of ferromagnesite (with variable iron content), to result in the formation of ferropericlase with a correspondingly variable magnesium index, along with carbon (in the form of diamond) and oxygen. Considering the complexity of this model and even assuming the presence of ferromagnesite in the lower mantle, the notion of variability in its iron content remains enigmatic.

The value of the magnesium index $mg = Mg/(Mg + Fe)_{at.}$ in ferropericlase–magnesiowüstite strongly correlates with the content of Ni in the mineral, varying from 0.08 wt% in most iron-rich magnesiowüstite to more than 1 wt% in ferropericlase (Fig. 4.10). The concentration of Ni in ferropericlase with $mg > 0.8$ is close to 1%, which is significantly higher than that estimated for lherzolite with 1% of the metal alloy.

Several explanations can be offered for such a high variability of mg values in lower-mantle ferropericlase. First, variations in mg may be caused by the occurrence and concentration of the metallic phase in the lower mantle, which should result in an increase of mg in both ferropericlase and bridgmanite (Ryabchikov and Kaminsky 2013a, 2014). The content of the iron–nickel alloy is suggested to be close to 1% under lower mantle conditions (Frost and McCammon 2008). The concentration of Ni in iron-rich ferropericlase should decrease remarkably due to its transition into the metal phase, as was demonstrated in Ryabchikov (2011) and Ryabchikov and Kaminsky (2013b). Second, different bulk compositions of host rocks are another factor that may control the compositional variations of sub-lithospheric ferropericlase. The abundance of the lower mantle minerals included in diamonds (ferropericlase, 56%; bridgmanite, 8%; CaSi-perovskite, 12%; SiO$_2$, 8%; other minerals, 17%) differs significantly from the calculated values for pyrolite (ferropericlase, 18–20%; bridgmanite, 70–74%; CaSi-perovskite, 8–10%), which points to the difference between the compositions of the lower mantle and the upper mantle. In particular, the presence of more high-temperature rocks, such as
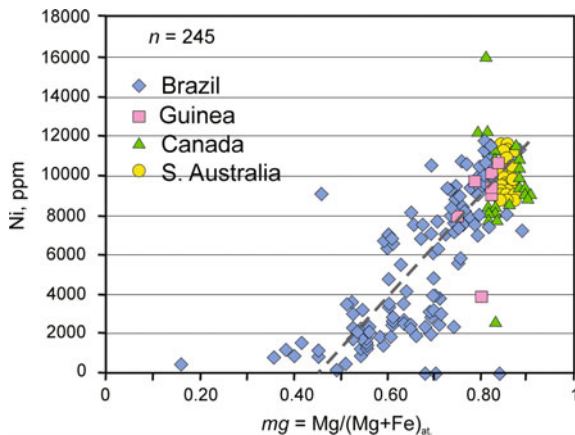
Fig. 4.10 Dependence of the nickel concentration on mg for ferropericlase-magnesiowüstite in diamond inclusions from various regions worldwide. Data from Scott Smith et al. (1984), Moore et al. (1986), Wilding (1990), Hutchison (1997), Stachel et al. (2000), Hutchison et al. (2001), Kaminsky et al. (2001, 2009b), Davies et al. (2004), Hayman et al. (2005), Tappert et al. (2005a, 2009a), van Rythoven and Schulze (2009), Thomson et al. (2014), Zedgenizov et al. (2014a), Burham et al. (2016). Modified after Ryabchikov and Kaminsky (2013a), with additions

harzburgite in addition to primitive lherzolite in the lower mantle, may result in the appearance of ferropericlase with different compositions compared to the mineral in the pyrolite bulk environment. The third scenario is that iron-rich ferropericlase may be formed as a result of magma fractional crystallisation directly in the lower mantle. Such a possiblility is supported by the experimental data. High P–T DAC results from Nomura et al. (2011) and Andrault et al. (2012) demonstrated that the partitioning coefficient of Mg/Fe between lower mantle phases and melt $K_D = (Mg/Fe)^{crystal}/(Mg/Fe)^{melt}$ are always >1, which is similar to those for olivine and pyroxenes under crustal conditions; consequently, the Fe/Mg ratio increases during fractional crystallization.

It should be noted that some researchers assume the presence of cumulates of iron-rich magnesiowüstite near the core–mantle boundary, the origin of which results from the solidification of the basal magmatic ocean at the early stages of the Earth's history (e.g., Nomura et al. 2011). As a whole, comparisons from the results of model calculations within the database of the composition of ferropericlase inclusions in diamonds demonstrates that the lower mantle is mainly composed of rocks of peridotitic composition, most likely including fertile varieties close to pyrolite, as well as more refractory rocks of a harzburgitic composition (Irifune et al. 2010).

Distribution of ferrous and ferric ions in ferropericlase. The distribution of ferrous and ferric ions in the structure of ferropericlase was revealed recently in studies by A. Abakumov involving ferropericlase grains from inclusions in diamonds from the Juina kimberlites (Kaminsky et al. 2015b). High-angle annular dark-field scanning transmission electron microscopy (HAADF-STEM) images demonstrated the presence of iron Fe^{3+}-rich octahedral-shaped clusters, varying in size from 5 to 10–20 nm and numerous smaller shapeless clusters with a size of 1–2 nm, within natural ferropericlase grains (Fig. 4.11a, b). The clusters are faceted by the {111} crystal planes delimiting truncated octahedra. High-resolution HAADF-STEM images demonstrated that the clusters have an Mg/Fe ordered structure, which is responsible for the superlattice reflections causing doubled $a \approx 8.4$ Å supercell (Fig. 4.11c). Both EDX analysis and STEM–EELS compositional mapping showed that the clusters are Fe-enriched and Mg-depleted (Fig. 4.11d, e).

The observed Fe/(Fe + Mg) ratio in the octahedral clusters corresponds to non-stoichiometric $Mg_{1+x}Fe_{2-x}O_{4-x/2}$ compounds with the structure intermediate between those of the B1 (rock salt) and H1$_1$ (spinel) structure types (Moran et al. 2002). The end member wüstite ($Fe_{1-x}O$) is well known to be highly nonstoichiometric. Commercially available wüstite typically has a composition of $Fe_{0.88}O$; there is relatively high ferric iron content in its lattice (Fei 1996). Relatively high stoichiometric wüstite, with a composition as high as $Fe_{0.98}O$ has been synthesized at high P–T conditions near the iron-wüstite buffer (McCammon 1993).

High-energy resolution EEL spectra demonstrated that signals from the non-stoichiometric clusters clearly showed that both the L$_3$ and L$_2$ peaks shift to higher energies, characteristic of Fe^{3+} ions, which are octahedrally coordinated (van
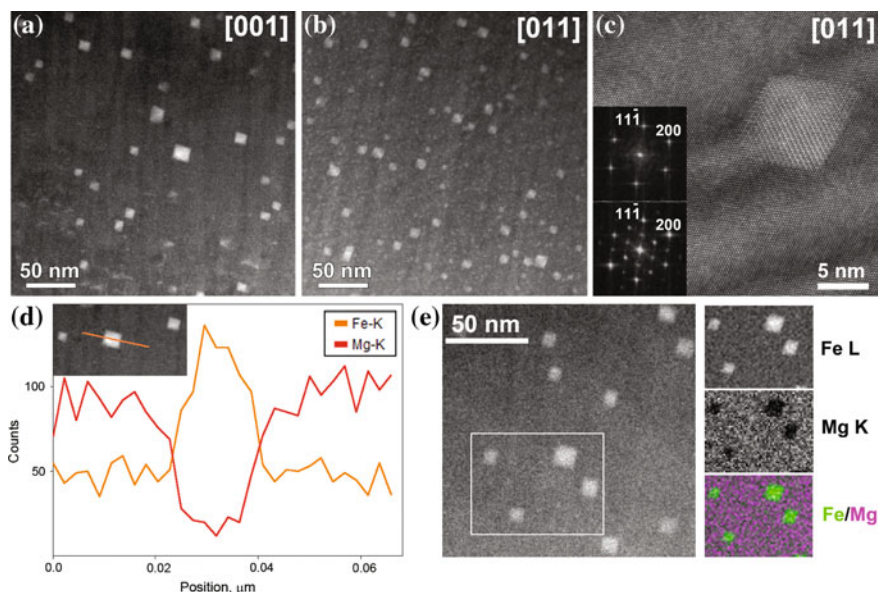
Fig. 4.11 Low magnification HAADF-STEM image of ferropericlase #C-143 in [001] pattern (**a**) and low magnification HAADF-STEM image of sample #7-100 in [011] pattern (**b**). The octahedral clusters on these images look prominently brighter due to a higher Fe content than in the surrounding ferropericlase matrix. High resolution HAADF-STEM image of a cluster in sample #7-100 with [011] pattern (**c**). Fourier transforms from the areas of the ferropericlase matrix and the cluster are shown as *top* and *bottom inserts*, respectively. The superlattice reflections originate exclusively from the cluster. The intensity profiles of the EDX Fe K and Mg K lines across the octahedral cluster in sample #C-143 showing Mg-depletion and Fe-enrichment (**d**). The insert shows the corresponding HAADF-STEM image with the line selected for acquiring the STEM EDX signal. HAADF-STEM image of the sample #7-100 with the area selected for EELS compositional mapping (**e**); the signal maps of the Mg K, Fe L edges and their color-coded mixed image. From Kaminsky et al. (2015b). © Elsevier

Aken and Liebscher 2002). According to the same EEL spectra collected from the ferropericlase matrix, the iron cations in the matrix are in the ferrous Fe^{2+} state.

Weak superstructure reflections were observed in both the [001] and [011] electron diffraction patterns. These reflections require a doubling of the unit cell parameter, resulting in a face-centered cubic unit cell with $a \approx 8.4$ Å. With the exception of reflection conditions imposed by *F*-centering, the $hk0$: $h + k = 4n$ reflection condition is deduced from the [001] ED pattern, suggesting that the most symmetric space group is $Fd\bar{3}m$. This unit cell parameter and the space group symmetry are characteristic of the $H1_1$ magnesioferrite structure. In other fPer inclusions in diamonds, collected from the same Juina area in Brazil, crystals of magnesioferrite, 10–50 nm in size, were observed to exhibit cubic and octahedral forms along dislocation lines (Wirth et al. 2014; Kaminsky et al. 2015a; Palot et al. 2016).

These results demonstrate the inhomogeneous distribution of ferric ions in ferropericlase and its concentrations in iron-rich, magnesioferrite-like clusters.

In early works, which used Mössbauer spectroscopy, the ferric iron proportion ($Fe^{3+}/\Sigma Fe$) in MgO-rich ferropericlase was low, approximately 0–7% of the total iron content (McCammon et al. 1997; Jacobsen et al. 2002), which is much lower than in the FeO-rich magnesiowüstite and wüstite samples (Fei 1996). Recent use of synchrotron radiation facility to collect energy domain Mössbauer spectra of ferropericlase inclusions in diamond gained similar results ($Fe^{3+}/\Sigma Fe$ = 3–9%; Nestola et al. 2016a). However, Mössbauer spectra of Fe^{3+}-rich magnesioferrite clusters within ferropericlase are magnetically split, with absorption divided over many lines with intensities similar to the baseline scatter. Hence, the signal from the magnesioferrite/Fe^{3+} cluster is not included in the Mössbauer spectrum of ferropericlase, and the concentration of Fe^{3+} in ferropericlase, established with the use of Mössbauer spectroscopy, is less than the total by 2–3% (according to the share of magnesioferrite/Fe^{3+} clusters in the matrix of ferropericlase; Kaminsky et al. 2015b).

Flank method was used for the determination of $Fe^{3+}/\Sigma Fe$ in ferropericlase with the use of an electron microprobe. This method has an advantage over Mössbauer spectroscopy because it has better spatial resolution ($\sim$1–10 μm against $\sim$100 μm) and a possibility to measure single ferropericlase samples containing exsolved clusters ('magnesioferrite'), even when these materials are too small to be resolved by electron microprobe measurements (Longo et al. 2011). The results demonstrated that values of $Fe^{3+}/\Sigma Fe$ in ferropericlase varied from 8 to 12%, and samples analyzed earlier, corrected for Fe^{3+} in clusters, comprised 3–10% (Kaminsky et al. 2015b).

Minor elements in ferropericlase. The most abundant minor elements in ferropericlase, in addition to Ni, are Cr, Mn and Na, each comprising up to 1–2.5 wt% of the total (Table 4.6). This corresponds to the experimentally established high values of $K_D^{fPer-Melt}$ for Cr and Mn, according to which ferropericlase may be a host phase for these elements (Righter et al. 2014 and references therein). Mn has a negative covariance with mg. Na is positively related to Cr.

Trace element contents in ferropericlase show an irregular distribution that vary considerably in abundance and are usually below chondrite level; only Li, Ta, Th, and U are consistently enriched. REE patterns show the enrichment in heavy REE around the chondrite level (Fig. 4.12). Walter et al. (2004b) earlier determined ferropericlase-melt partition coefficients for a series of trace elements in ferropericlase. Despite large measurement uncertainties, most minor and trace elements, with the exceptions of Cr and Ni, were considered to be incompatible in fcrropericlase. In particular, REE have experimental K_D values below 0.1; however, natural samples do not confirm this finding (Fig. 4.12). U and Th were not measured but were expected to be highly incompatible based on the results obtained for other tetravalent cations (Si, Ti, Zr, and Hf). However, natural samples show the reverse.

Table 4.6 Minor elements in ferropericlase (wt%) (from Kaminsky 2012)

Oxides	Brazil					Gunea	Canada	
	São Luiz	Rio Mutum. Vermelho. Chicoria	Rio Soriso	Pandrea pipes	Collier-4 pipe	Kankan	DO27, DO18, A21, Ranch Lake pipes	Panda pipe
Cr_2O_3	0.19–2.56	0.11–2.26	0–1.30	0.10–0.65	0.09–0.27	0.12–1.04	0.41–2.56	0.69–0.75
NiO	0.10–1.49	0.02–1.37	0.11–1.46	0.59–1.34	1.02–1.48	0.51–1.46	0.33–1.55	1.34–2.14
MnO	0.07–0.81	0.19–0.94	0.16–1.46	0.15–0.42	0.14–0.18	0.16–0.26	0.13–0.34	0.12–0.24
Na_2O	0.02–1.25	0.04–1.35	0–1.20	0.01–0.24	0–0.03	0.07–0.79	0.04–1.11	0.07–0.19
mg	0.36–0.87	0.49–0.83	0.45–0.89	0.75–0.81	0.76–0.86	0.75–0.92	0.84–0.90	0.80–0.87
References	Wilding (1990), Harte et al. (1999)	Kaminsky et al. (2001)	Hayman et al. (2005)	Kaminsky et al. (2009a)		Stachel et al. (2000)	Davies et al. (2004)	Tappert et al. (2009a)
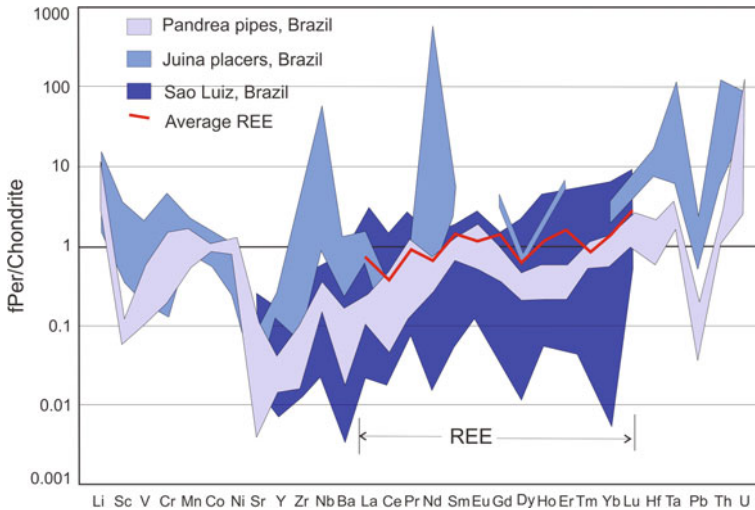
Fig. 4.12 Chondrite-normalised trace element patterns in ferropericlase-magnesiowüstite. Data from Harte et al. (1999), Kaminsky et al. (2001, 2009a). Chondrite composition from McDonough and Sun (1995). Modified after Kaminsky (2012), with additions

4.3.3 Crystal Structure and Phase Transitions of Ferropericlase–Magnesiowüstite at High Pressures and Temperatures

Cubic crystal structure. MgO–FeO forms a complete solid solution series with a gradual compositional transition between the end-member periclase and wüstite in the cubic crystal structure B1 with space group $Fm\bar{3}m$ (NaCl type with $Z = 4$) (Fig. 4.13), in which end-members differ only in crystal parameters: $a = 4.203$–4.212 Å for pure periclase and $a = 4.296$ Å for pure wüstite. For intermediate compositions, the structure consists of interpenetrating face-centered-cubic lattices producing alternating Mg^{2+}/Fe^{2+} cations and O^{2-} anions. The structure can also be described as an edge-share array of $(Mg,Fe)O_6$ octahedra in which all edges are shared with neighbouring octahedra (Wicks and Duffy 2016).

In natural ferropericlase–magnesiowüstite samples found in diamond inclusions, the series occupies a composition range, almost reaching both end-members. The magnesium end-member periclase MgO was found to be stable as the cubic rocksalt (B1) structure ($Fm\bar{3}m$ space group) to at least 227–250 GPa along the Hugoniot curve in early shock wave experiments or to 250 GPa in static DAC experiments, i.e., to pressures in the bottom of the lower mantle and in the outer core (Duffy et al. 1995; Dorfman et al. 2012). Its transition to the cubic CsCl-type (B2) phase (space group $Pm\bar{3}m$) is observed only at ~ 600 GPa, and the B2 phase is found to be stable up to 900 GPa (Coppari et al. 2013). Theoretical calculations, performed with the use of an evolutionary algorithm demonstrated that at pressure 116 GPa,
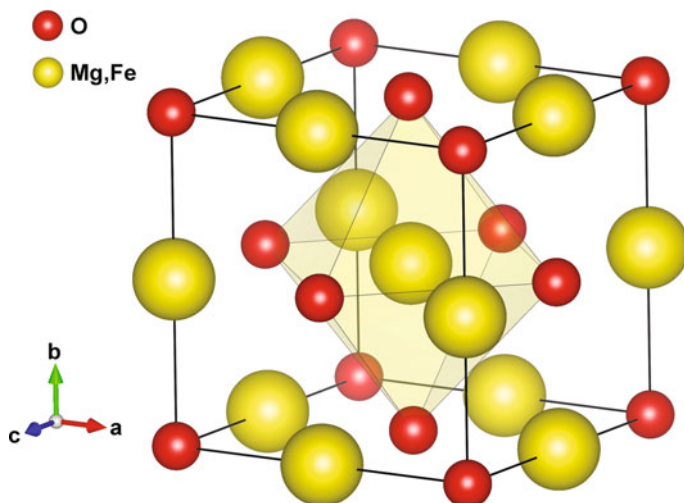
Fig. 4.13 Crystal structure of ferropericlase with cubic rock-salt structure (space group $Fm–3m$). Lattice parameters from Mao et al. (1996)

magnesium peroxide MgO_2 becomes stable, and contains transitional ions $[O–O]^{2-}$ (Zhu et al. 2013). Recently these calculations were confirmed experimentally with the use of DAC and synchrotron XRD (Lobanov et al. 2015). Raman spectroscopy detected the presence of a peroxide ion (O_2^{2-}) in the synthesised material as well as in the recovered specimen. MgO_2 forms as a result of the reaction for $2MgO + O_2 \rightarrow 2MgO_2$ in the presence of free oxygen at a pressure 94 GPa and temperature 2150 K. The resulting magnesium peroxide MgO_2 has a tetragonal structure with space group $I4/mcm$, which is significantly denser than the periclase with the $Fm3m$ structure (Lobanov et al. 2015). The formation of magnesium peroxide may happen only under high oxygen fugacity conditions.

Rhombohedral structure. By contrast, the iron end-member wüstite FeO experiences various phase transitions under high-pressure conditions. FeO transition to the rhombohedral $R\bar{3}m$ structure (Fig. 4.14a–c) occurs at a pressure above 9–18 GPa at 300 K (Zou et al. 1980; Yagi et al. 1985; Mao et al. 1996; Shu et al. 1998; Kantor et al. 2004). The B1 → rhombohedral transition has also been observed at approximately 16 GPa not only in pure wüstite, but also in iron-rich Fe–Mg solid solutions ($fe = Fe/$(Mg + Fe) = 0.80–0.95) using in situ XRD in DAC experiments (Mao et al. 2002; Kondo et al. 2004; Kaercher et al. 2012). At the initial stage of the B1 → rhombohedral transition (still in cubic structure), a magnetic ordering transition was observed by Mössbauer spectroscopy and neutron powder diffraction at approximately 4.5 GPa, which is associated with an unusual discontinuity in the elastic constants as a function of pressure (Kantor et al. 2004). The B1 → rhombohedral structural transition in FeO can be viewed as an elongated distortion along <111> direction of the B1 lattice (Fig. 4.14b, c) such that it is also
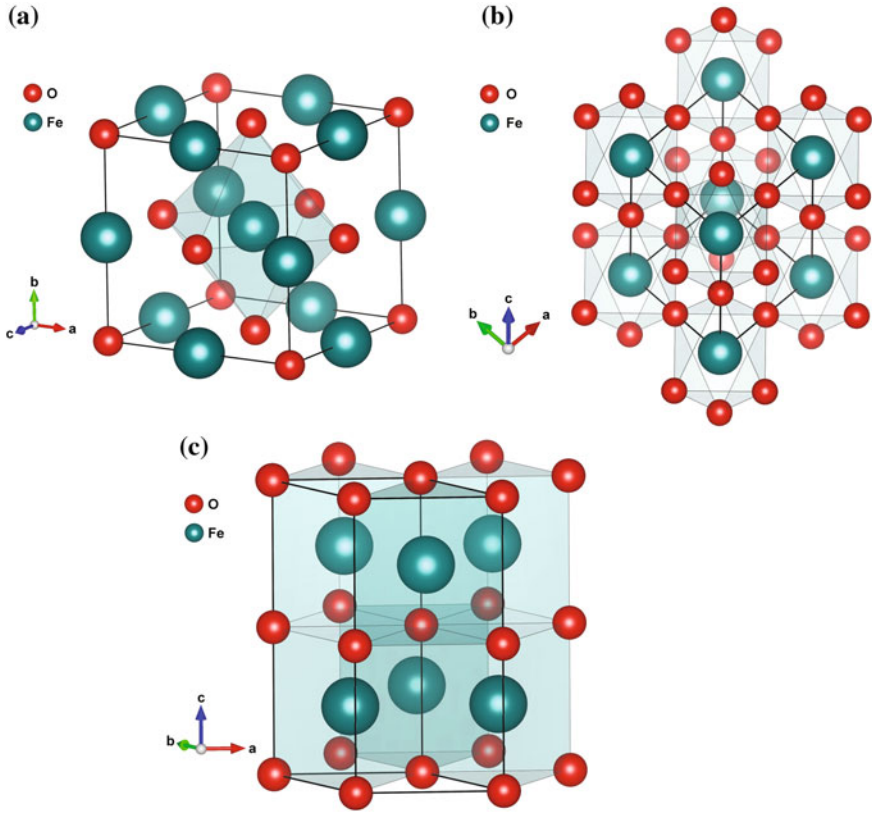
Fig. 4.14 Crystal structures of FeO phases under high pressure: cubic B1 with space group *Fm–3m* (*left*), B-rhombohedral with space group *R$\bar{3}$m* (*center*) and hexagonal B8 with space group *P6$_2$/mmc* (*right*). Lattice parameters from Mao et al. (1996)

found to be fairly sensitive to the pressure medium and thus hydrostaticity in the sample chamber as well as stoichiometry of the sample.

Hexagonal structure. At higher pressures ($\sim$70–75 GPa and 600–1600 K temperatures), the B1 wüstite transforms to the hexagonal NiAs (B8) structure (space group *P6$_3$/mmc*) (Fei and Mao 1994; Sherman and Jansen 1995; Kondo et al. 2004; Murakami et al. 2004b; Fischer et al. 2011b; Kaercher et al. 2012) and the lattice parameters of the high-pressure hexagonal B8-structured FeO, established at 96 GPa and 800 K in the first synthetic crystals with the use of in situ synchrotron XRD, were: $a = 2.574$ Å and $c = 5.172$ Å (Fei and Mao 1994) (Fig. 4.15). However, the location and the Clapeyron slope of the phase boundary at high *P–T* remain extensively debated: earlier results suggested the transition from a vertical slope near 70 GPa (Murakami et al. 2004b) to a strongly positive slope in *P–T* space (Kondo et al. 2004; Ozawa et al. 2010). Some experiments have failed to obtain the transition to the B8 phase at all (Mao et al. 1996; Seagle et al. 2008) and

Fig. 4.15 Phase diagram for wüstite at high pressures and temperatures. Data from Fei and Mao (1994), Mao et al. (1996), Kondo et al. (2004), Fischer and Campbell (2010), Fischer et al. (2011a, b), Ozawa et al. (2010), Ohta et al. (2014), Wicks et al. (2015). Mantle adiabate after Katsura et al. (2010)
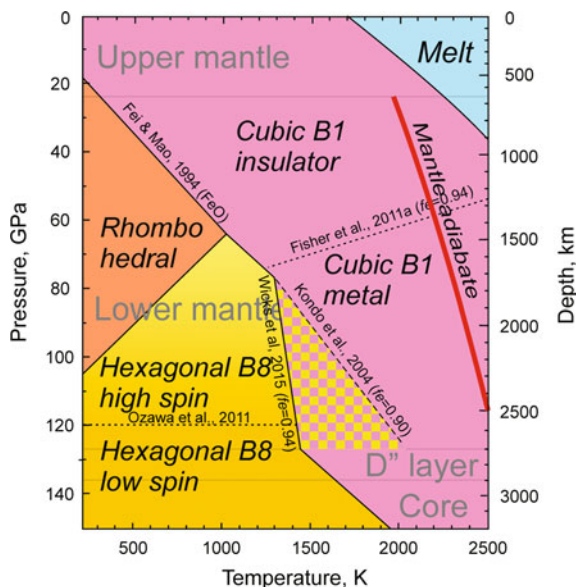
have attributed this to kinetic barriers at room temperature (Mao et al. 1996) or to differences in stoichiometry (Seagle et al. 2008).

The transformation from the B1 to the B8 structure has been observed only for the Fe end-member, and was not observed to occur in less iron-rich samples (*fe* = 0.61–0.75) up to 86–102 GPa and 2500 K (Lin et al. 2003; Kondo et al. 2004). Recent experiments with polycrystalline magnesiowüstite with *fe* = 0.94 obtained from XRD under heating up to 122 GPa and 2100 K demonstrated that the addition of Mg to FeO stabilizes the B1 phase with respect to the B8 phase at these conditions (Wicks et al. 2015).

In the deep Earth, wüstite can undergo the B1 → B8 phase transition at temperatures well below the geotherm and may occur only in the subsolidus conditions of the lower mantle (Fig. 4.15).

Based on the thermodynamic analysis of the MgO–FeO solid solution at high pressures and temperatures, an immiscibility gap has been proposed to exist between the B8 and B1 structures (McCammon et al. 1983). XRD experiments demonstrated that intermediate solid solutions (*fe* = 0.20–0.50) dissociate, at least partially, at conditions near 83–86 GPa and 1000 K (corresponding to a depth of 1900–2000 km) to an Mg-enriched composition and an almost pure wüstite (FeO) composition (Dubrovinsky et al. 2000, 2001a). However, this finding was initially not confirmed by other groups. Experiments on peridotite compositions of up to 124 GPa have reported no evidence of the dissociation (Murakami et al. 2005) and diffraction experiments on more Fe-rich compositions (*fe* = 0.61–0.75) at 86–102 GPa and 2500 K found no evidence of such a dissociation (Lin et al. 2003). More recently, an iron-rich composition (*fe* = 0.96) was found to decompose into hexagonal B8-FeO and $(Mg_{0.06}Fe_{0.94})O$ in a diffraction pattern at 123 GPa after

heating up to 2800 K; this effect was explained by the metallization of the FeO component. This sample was also recovered to 1 bar for ATEM measurements and was shown to have these two distinct phases (Ohta et al. 2014). In addition, recently, Martirosyan et al. (2016) confirmed the immiscibility gap in the FeO–MgO system at pressures greater than 70 GPa.

Observations in natural samples confirm decomposition of ferropericlase into iron- and magnesium-rich phases. In one of the samples from the Juina area in Brazil, coexisting grains of almost pure wüstite and periclase were identified: wüstite with $mg = 0.02–0.15$ and periclase with $mg = 0.85–0.92$ (confirmed by electron diffraction data); no ferropericlase or magnesiowüstite of intermediate composition were observed (Kaminsky et al. 2009b). The analyzed grains exhibited some compositional variation (Table 4.7).

On a histogram (Fig. 4.16), inclusions form two groups with respect to their magnesium index. Most of the grains are highly enriched in Mg with low Fe concentrations ($mg = 0.85–0.92$). However, a significant part of the grains analyzed (approximately 25%) are low-Mg, high-Fe wüstite with $mg = 0.02–0.15$. A subset of these have extremely high ferrogenosity ($fe = 0.96–0.98$), close to stoichiometric wüstite.

In another sample from the same Juina area in Brazil, a single crystal of almost pure wüstite with composition $(Mg_{0.07}Fe_{0.93})O$ completely encapsulated by

Table 4.7 Chemical compositions of coexisting wüstite and periclase inclusions in diamond from the Juina area, Brazil (at.%; AEM data; from Kaminsky et al. 2009b)

Grain #	Mg	Mn	Fe	Total
Wüstite				
1	3.4	0	96.6	100.0
2	15.3	0.4	84.3	100.0
3	13.2	0	86.8	100.0
4	13.0	0.6	86.4	100.0
5	1.9	0	98.1	100.0
Periclase				
6	85.4	0.4	14.2	100.0
7	91.2	1.2	7.6	100.0
8	85.5	0.4	14.1	100.0
9	92.1	1.0	6.9	100.0
10	87.7	1.2	11.1	100.0
11	85.5	0.5	14.0	100.0
12	84.9	0.2	14.9	100.0
13	86.7	0.9	12.4	100.0
14	89.7	0.6	9.7	100.0
15	86.4	0.4	13.2	100.0
16	87.8	1.2	11.0	100.0
17	91.3	0.6	8.1	100.0
18	91.5	1.1	7.4	100.0
19	90.3	0.4	9.3	100.0
20	86.8	0.6	12.6	100.0
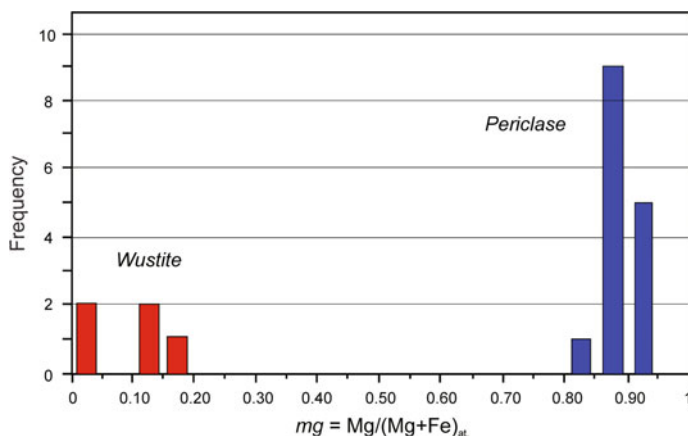
Fig. 4.16 Magnesium index *mg* in coexisting wüstite and periclase inclusions from diamond #8/103

polycrystalline periclase $(Mg_{0.93}Fe_{0.07})O$ was observed in a lower-mantle inclusion in diamond (Kaminsky et al. 2015a) (Fig. 4.17). These findings in natural samples indicate that ferropericlase can decompose into Mg- and Fe-rich phases at certain *P–T* conditions, such that natural ferropericlase samples with intermediate compositions were formed, most likely, under pressure conditions of less than 83–86 GPa, i.e. at depths shallower than 1900–2000 km. A possible explanation for the dissociation is the metallization of the FeO end-member component that promotes this dissociation process. In this scenario, the highly conductive iron-rich (Mg,Fe)O magnesiowüstite and metallic FeO rocks located at the base of the mantle may play an important role for the dynamics and evolution of Earth's mantle and core (Ohta et al. 2012, 2014).

Metallization of B1-FeO. Theoretical studies predicted the metallization of B1-FeO at high pressures (Ringwood 1977; Sherman 1989; McWilliams et al. 2012); however, the location of this transition has not been predicted. The electronic transition, interpreted as metallization, was initially thought to coincide with the B1 → B8 transition (Fei and Mao 1994; Murakami et al. 2004b); however, with new data on the location and slope of the B1/B8 phase boundary (Fig. 4.15), it has become apparent that this is not the case. Other studies found that B1-FeO is a semiconductor up to ∼70 GPa and 1500–1760 K, while B8-FeO is metallic (Ohta et al. 2010; Fischer et al. 2011a). More recent experiments in a LHDAC demonstrated that B1-structured FeO metallizes at around 70 GPa and 1900 K without any structural phase transition (Ohta et al. 2012). Despite a high electric conductivity above 85 GPa and 1300 K, more Mg-rich samples (*mg* = 0.05–0.20) remain insulators (Ohta et al. 2014).

The melting curve of $Fe_{1-x}O$ has been determined up to pressures and temperatures of 77 GPa and 3100 K (Fischer and Campbell 2010).

Fig. 4.17 Spherical inclusion of wüstite (core) + periclase (rim) in a dolomite matrix. *Irregular dark areas* are pores. Elemental map. Scale bar is 500 nm. Sample #8/108 from the Juina area, Brazil. From Kaminsky et al. (2016). Used with a permission of Springer
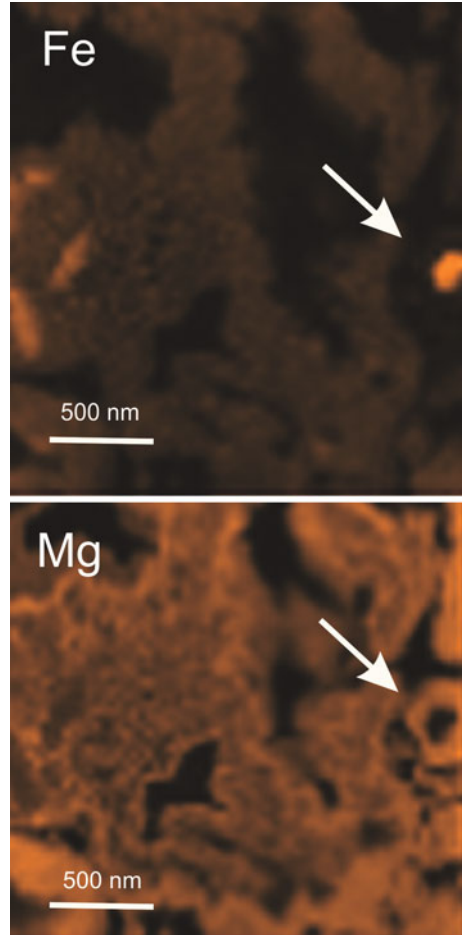
4.3.4   Physical Properties of Ferropericlase-Magnesiowüstite

The role of the chemical composition of ferropericlase. The substitution of FeO in (Mg,Fe)O inherently affects physical properties of the ferropericlase–magnesiowüstite system in the Earth's interior. Iron is the most abundant transition metal on the planet and can exhibit various spin and valence states based on thermodynamic environments. Ferrous iron is more than twice as heavy than the magnesium cation in the ferropericlase, but its ionic radius is only slightly larger than that of Mg^{2+}, such that the addition of FeO is expected to slightly expand the lattice parameters while the density is more significantly enhanced (Jacobsen et al. 2002).

Density. Based on static compression data at 70 GPa and 900 K (Fei and Mao 1994), the density of B8-type hexagonal FeO as a result of the B1 → B8 structure transition increases by 4%, which is consistent with the original evaluation of the shock compression data (Jeanloz and Ahrens 1980). The 4% density increase can be explained by geometric rearrangement from the rock salt to NiAs structure and the change in the *c/a* ratio of the B8 phase (Jackson et al. 1990).

Elastic properties. The bulk modulus (the incompressibility) of (Mg,Fe)O was studied as a function of pressure and composition using pressure–volume relations in XRD measurements and the V_P and V_S profiles using ultrasonic interferometry (Richet et al. 1989; Jacobsen et al. 2002; Lin et al. 2005, 2013; Zhang and Zhao 2005). Studies of non-stoichiometric, iron-rich (Mg,Fe)O showed that both adiabatic bulk modulus (K_S) and isothermal bulk modulus (K_T) decrease as a function of Fe concentration (Richet et al. 1989; Jacobsen et al. 2002). The trend is opposite for stoichiometric samples, where ultrasonic interferometry studies for iron-poor samples display a positive trend of K_S with increasing iron content (Jacobsen et al. 2002). In the wüstite end-member, K_T does depend on stoichiometry in the B1 phase, with $Fe_{0.99}O$ being much less compressible than $Fe_{<0.98}O$ (Fei 1996; Zhang and Zhao 2005). The initial studies of the elasticity of (Mg,Fe)O have shown that the shear modulus, G, is much more sensitive to iron content than the bulk modulus (e.g., Jackson et al. 2006).

Thermal and electrical conductivity. Ohta et al. (2017) examined the lattice thermal conductivity of (Mg,Fe)O containing 19 mol.% Fe up to 111 GPa and 300 K by means of the pulsed light heating thermoreflectance technique in a DAC. They demonstrated a strong reduction in the lattice thermal conductivity of ferropericlase due to iron substitution. Ohta et al. (2017) also measured the electrical conductivity of an identical ferropericlase sample up to 140 GPa and 2730 K and found that ferropericlase remains an insulator throughout the experimental conditions, indicating the electronic thermal conduction in ferropericlase is negligible. This data indicates that bridgmanite (and post-perovskite) is the best heat conductor in the Earth's lower mantle, and distribution of iron and its valence state among the lower mantle minerals are key factors to control the lower mantle thermal conductivity.

Electronic iron spin transition. Physical properties of ferropericlase can also be affected by the electronic spin transition of iron at high pressures, including changes in elasticity, iron partitioning and electrical and thermal conductivities (see Lin et al. 2013 for a review) that may contribute to seismic heterogeneities of the region (for a detailed discussion about the spin transition see Chap. 8). There have been a number of early experimental and theoretical studies on the incompressibility, equation of state and elastic constants of single-crystal ferropericlase across the spin transition at high pressures using various techniques, including Impulsive Stimulated Light Scattering (ISS), Brillouin Light Scattering (BLS), Inelastic X-ray Scattering (IXS), and Density Function Theory (DFT), but some results were not in agreement with others (Antonangeli et al. 2011; Crowhurst et al. 2008; Marquardt et al. 2009a, b; Yang et al. 2015; Wu et al. 2013; Wu and Wentzcovitch 2014). The most recent experimental results and DFT calculations have shown that ferropericlase exhibits significant softening in V_P, as well as the C_{11} and C_{12} elastic

constants across the spin crossover at lower-mantle P–T conditions, although V_S and C_{44} were not affected by the transition (Wu et al. 2013; Yang et al. 2015). The spin transition was associated with a significant reduction of the aggregate V_P/V_S via the aggregate V_P softening because V_s softening did not visibly occur within the transition. These results suggest that the middle to lowermost parts of the lower-mantle may exhibit enhanced seismic heterogeneities due to the occurrence of the mixed-spin and low-spin ferropericlase (Yang et al. 2015).

Iron spin crossover in ferropericlase also influences the conductivity of ferropericlase: it reduces its lattice thermal conductivity, as well as its radiative conduction (Ohta et al. 2017).

An electronic high-spin to low-spin transition of iron in B8-structured wüstite ($fe = 0.96$) was experimentally observed to occur at ~ 119 GPa with a volume reduction of $\sim 2.5\%$ in situ X-ray emission spectroscopy XES and XRD measurements (Ozawa et al. 2011). While the crystal structure of FeO remains as B8 type across such volume reductions, the atomic arrangements of Fe and O change from the inverse to the normal NiA form, with considerable decrease in c/a axial ratio. Together with recent electrical resistance measurements, these results suggest that the spin crossover, inverse-normal structural change, and insulator–metal transition occur concurrently in B8-FeO at approximately 120 GPa (Ozawa et al. 2011).

4.4 Iron Partitioning Between Bridgmanite and Ferropericlase

4.4.1 General

High P–T experiments along an expected mantle geotherm for a pyrolitic composition demonstrated that the iron index, $fe = \text{Fe}/(\text{Fe} + \text{Mg})_{at.}$, of the pyrolitic lower-mantle ferropericlase should be 0.12–0.27 (Wood 2000; Lee et al. 2004),or even lower, at c. 0.10 (Kesson and Fitz Gerald 1991). These results suggest that the iron chemistry of lower-mantle ferropericlase may not vary significantly. However, although a majority of the studied natural lower-mantle ferropericlase grains hosted within deep-diamond inclusions have $fe = 0.10$–0.20, more than 40% of them vary in a 'forbidden' range with up to $fe = 0.64$ falling into the field of magnesiowüstite (e.g., Hutchison 1997; Kaminsky 2012); one of the analyzed samples has an iron index as high as 0.9, which is almost close to the end-member wüstite stoichiometry. Some grains of bridgmanite, coexisting with iron-rich ferropericlase, also exhibit relatively high iron contents. The discovery of these iron-rich ferropericlase and magnesiowüstite grains deviates from the traditional view of the pyrolitic lower mantle composition, which argues for a homogenous iron chemistry and mineralogy, and points to a much more complex chemistry of the lower mantle (Kaminsky and Lin 2017).

4.4.2 Experimental Works on Partitioning of Iron Between Bridgmanite and Ferropericlase

A number of experimental works on iron partitioning between bridgmanite and ferropericlase in a laser-heated DAC, subjected to relevant lower-mantle conditions of up to approximately 120 GPa have been performed over the last two decades. Almost all experiments modelled the suggested pyrolitic model of the lower mantle with iron index, $fe = Fe/(Fe + Mg)_{at.} = 0.05$–0.10. The only exception was the work performed by Tange et al. (2009) in a multi-anvil apparatus with sintered diamond anvils, in which the starting material was very different from pyrolitic and had $fe = 0.50$; it resulted in a highly iron-rich association, bridgmanite with $fe = 0.16$–0.32 and ferropericlase with $fe = 0.49$–0.92. The other studies have shown disparate results on the distribution of Fe in the various minerals (Fig. 4.18a). For example, while some demonstrated a positive correlation of the iron index between bridgmanite and ferropericlase (0.070–0.234) (Katsura and Ito 1996; Kesson et al. 2002; Kobayashi et al. 2005; Murakami et al. 2005; Sakai et al. 2009), others found the opposite: a negative correlation (Irifune 1994; Kesson et al. 1998; Wood 2000; Irifune et al. 2010) (Fig. 4.18a). At $fe_{fPer} = 0.05$–0.20 for both trends, the positive correlation was obtained mainly in association with low-Fe bridgmanite ($fe = 0.010$–0.103), while the negative correlation was in association with high-Fe bridgmanite ($fe = 0.081$–0.167). Additionally, there were experimental results showing variations in $fe_{Brd} = 0.011$–0.077 that were virtually independent of fe_{fPer} (c. 0.10) (Auzende et al. 2008). The general trends (I and II) can be identified in a consolidated graph (Fig. 4.18a). The positive trend divides into two branches (trends Ia and Ib) with the same correlation but with different values of fe_{Brd}, which could be due to a different pressure range being examined. These experimental discrepancies remain unexplained.

Experimental evaluations of the partition coefficient of iron between ferropericlase and bridgmanite defined as $K_D^{Brd-fPer} = (Fe/Mg)^{Brd}/(Fe/Mg)^{fPer}_{at.}$ produce even more inconsistent results. The values of $K_D^{Brd-fPer}$ vary from 0.04 to 0.9
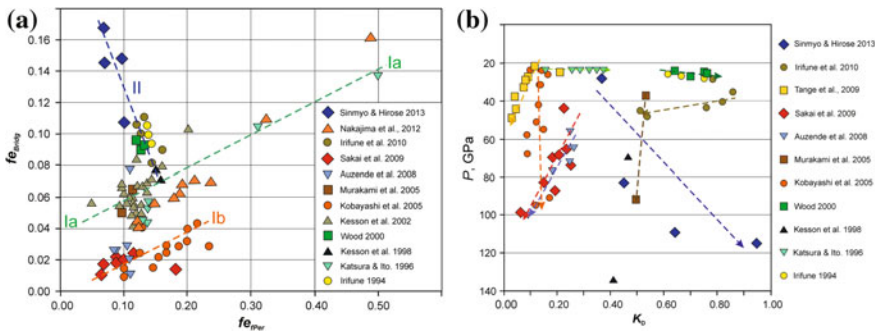
Fig. 4.18 Summary of literature experimental results of iron partitioning between bridgmanite and ferropericlase at high pressures and temperatures. **a** fe_{Brd} versus fe_{fPer}. **b** Variability of $K_D^{Brd-fPer}$ under different pressure conditions. From Kaminsky and Lin (2017). Used with a permission of the Mineralogical Society of America

(Fig. 4.18b). Some of the experiments have shown an increase of $K_D^{\mathrm{Brd-fPer}}$ with pressure (Irifune 1994; Kobayashi et al. 2005; Sinmyo and Hirose 2013), whereas others have demonstrated the reverse (Andrault 2001; Kesson et al. 2002; Murakami et al. 2005; Tange et al. 2009; Irifune et al. 2010), and a third have not found any correlation between $K_D^{\mathrm{Brd-fPer}}$ and pressure (Guyot et al. 1988; Katsura and Ito 1996; Auzende et al. 2008). Specifically, the concentration of Al^{3+} in bridgmanite has been shown to significantly affect its iron partitioning and Fe^{3+} content; it has been shown that the dissolution of Al^{3+} in bridgmanite at the top lower-mantle conditions can significantly enhance the Fe^{3+} occupancy in the A site of the lattice resulting in higher $K_D^{\mathrm{Bridg-fPer}}$ (Irifune et al. 2010). The cause of these discrepancies may be due to the differing conditions in the experiments (great thermal gradients, pressure duration, chemical homogeneity, non-thermodynamic equilibrium, etc.) and in the compositions of the starting materials, including different concentrations of Fe and Al used in the experiments.

The discovery of iron spin crossover in ferropericlase led to the suggestion that $K_D^{\mathrm{Brd-fPer}}$ would behave differently in relevant high P–T conditions found in the deep lower mantle, decreasing from the mid-lower mantle to bottom lower mantle conditions, such that most of the iron partitions into ferropericlase, leaving bridgmanite essentially iron-free (Badro et al. 2003; Speziale et al. 2005). More recent theoretical and experimental studies on a pyrolite composition have found that $K_D^{\mathrm{Brd-fPer}}$ increases from approximately 0.5 at top-lower mantle conditions to 0.7–0.9 at about 800 km in depth due to the suggested coupled substitution of Al^{3+} and Fe^{3+} in bridgmanite, but then decreases to 0.4 or even lower due to the spin crossover of iron in ferropericlase at mid-lower mantle conditions (Irifune et al. 2010; Vilella et al. 2015; Xu et al. 2017). However, a high P–T DAC study, using a pyrolite composition, has shown that $K_D^{\mathrm{Brd-fPer}}$ increases to 0.9 at bottom-lower mantle conditions; this is suggested to be due to the spin transition of Fe^{3+} in bridgmanite (Sinmyo and Hirose 2013). Recently, Fe-bearing bridgmanite has been reported to dissociate into Fe-rich phase, called H-Phase, and $MgSiO_3$-rich bridgmanite at deep lower mantle P–T conditions (Zhang et al. 2014), which can challenge the aforementioned conventional view of the iron index in the lower-mantle mineral assemblage. However, this report remains to be verified experimentally and theoretically. Thus far, a consensus on the iron partition coefficient across the spin transition in the lower-mantle assemblage has not yet been reached, especially under natural compositional, oxygen fugacity and P–T environments.

To elucidate the lower-mantle chemistry in these minerals, natural samples of bridgmanite manite and ferropericlase should be considered.

4.4.3 Natural Samples

To date, a number of bridgmanite, ferropericlase and other lower-mantle mineral grains have been identified as natural inclusions in diamonds, collected from Brazil, Canada, Guinea, Australia and some other countries, and subsequently analyzed (Kaminsky 2012 and references therein). Among them, there are 19 coexisting

bridgmanite + ferropericlase pairs, which allow for studies into the distribution and partitioning of iron and other elements within the media from which those minerals originated within the lower mantle.

Ferropericlase. As demonstrated above, ferropericlase does not always have a suggested and experimentally modelled composition with $fe = 0.08–0.11$ or even closer, at c. 0.10 (Kesson and Fitz Gerald 1991). In the natural environment, however, ferropericlase may be much more iron-rich, up to $fe = 0.64$, and sometimes even up to 0.90; as such, this does not correspond to the pyrolitic composition of the formation media. Iron in ferropericlase is predominantly in a divalent form; the share of ferric iron is $Fe^{3+}/\Sigma Fe = 8–12$ at.% (Kaminsky et al. 2015b). TEM studies with the use of EDX and EEL spectroscopy demonstrated that ferric iron in ferropericlase grains is located in exsolved non-stoichiometric Fe^{3+}-enriched clusters $Mg_{1+x}Fe^{3+}{}_{2-x}O_{4-x/2}$, varying in size from 1–2 nm to 10–15 nm and comprising ~ 3.6 vol.% of ferropericlase, while all remaining iron in ferropericlase is in the ferrous Fe^{2+} state (Kaminsky et al. 2015b) (Fig. 4.11a). These clusters, during the process of lowering pressure within the uppermost lower mantle, were released from the ferropericlase matrix and formed magnesioferrite $MgFe^{3+}{}_2O_4$ crystals, developing along dislocations in ferropericlase with a precise orientation relationship between both phases: $(022)_{mFer}//(022)_{fPer}$; $(11\text{-}1)_{mFer}//(11\text{-}1)_{fPer}$ and the zone axis for both phases is [2-11] (Kaminsky et al. 2015a) (Fig. 4.19).

Bridgmanite. Bridgmanite $^{VIII/XII}A^{2+}\,{}^{VI}B^{4+}O^{2-}{}_3$, (where VI, VIII and XII are cation fold positions), in which A larger (mainly divalent), pseudo-dodecahedral (8/12-fold) site cations mostly include Mg, Fe^{2+}, Mn, Ni, Ca and some other elements; and B smaller, six-fold site cations include Si, Al and partly Fe^{3+}. The cation compositions for the analyzed samples arepresented in Table 4.8.

Fig. 4.19 Octahedral and cubic grains of magnesioferrite $MgFe^{3+}{}_2O_4$, developed along dislocations in ferropericlase. Dark field TEM image by R. Wirth (Kaminsky et al. 2015a). Used with a permission of the Canadian Mineralogist

Magnesioferrite

Ferropericlase

50 nm
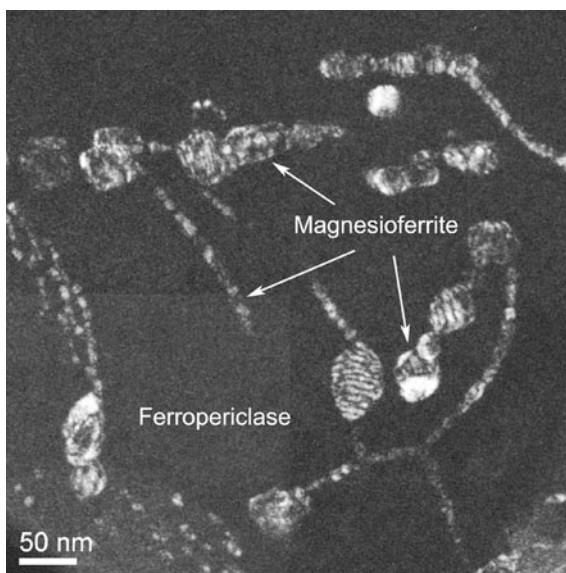
Table 4.8 Cation fractions of natural lower-mantle bridgmanite coexisting with ferropericlase (in atomic numbers) (Kaminsky and Lin 2017)

Sample No.	Mg	Fe	Ni	Mn	Ca	Na	K	A_{total} (VIII/XII)	Si	Al	Ti	Cr	B_{total} (VI)	Refs[a]
Juina area, Brazil														
BZ120	0.878	0.064	0.000	0.002	0.001	0.002	0.000	0.948	0.943	0.024	0.003	0.006	0.976	1
BZ207	0.795	0.125	0.000	0.004	0.001	0.002	0.000	0.928	0.923	0.052	0.003	0.002	0.980	1
BZ210	0.750	0.071	0.000	0.013	0.012	0.034	0.006	0.885	0.856	0.197	0.000	0.016	1.069	1
BZ241	0.674	0.075	0.000	0.018	0.012	0.027	0.000	0.805	0.903	0.201	0.000	0.015	1.120	1
BZ242	0.406	0.055	0.000	0.018	0.078	0.149	0.000	0.707	0.915	0.247	0.000	0.023	1.185	1
BZ251	0.900	0.053	0.000	0.002	0.001	0.001	0.000	0.957	0.950	0.026	0.002	0.005	0.983	1
14-2	0.833	0.068	0.000	0.002	0.021	0.004	0.000	0.928	0.946	0.027	0.001	0.006	0.980	2
1-5	0.863	0.087	0.000	0.002	0.001	0.000	0.000	0.953	0.934	0.041	0.001	0.003	0.979	3
3-2	0.830	0.059	0.000	0.002	0.001	0.000	0.000	0.891	0.969	0.031	0.003	0.003	1.006	3
3-5	0.824	0.092	0.000	0.004	0.000	0.000	0.000	0.920	0.927	0.061	0.003	0.003	0.993	3
4-3	0.877	0.059	0.000	0.001	0.000	0.002	0.000	0.941	0.933	0.048	0.003	0.004	0.987	3
Northwest Territories, Canada														
DO2700100	0.940	0.040	0.000	0.001	0.007	0.000	0.000	0.988	0.956	0.014	0.000	0.004	0.973	4
DO2700300	0.938	0.041	0.000	0.001	0.001	0.002	0.000	0.984	0.981	0.014	0.000	0.004	0.998	4
DO27-97 14A	0.896	0.059	0.000	0.001	0.002	0.001	0.000	0.959	0.953	0.040	0.000	0.005	0.998	4
Kankan area, Guinea														
KK-103	0.891	0.047	0.000	0.001	0.001	0.001	0.000	0.942	0.955	0.012	0.000	0.002	0.970	5
KK-108	0.866	0.068	0.000	0.002	0.002	0.001	0.000	0.939	0.946	0.033	0.001	0.003	0.983	5
KK-16	0.892	0.046	0.000	0.002	0.001	0.002	0.000	0.943	0.957	0.011	0.000	0.004	0.972	5
KK-44	0.911	0.049	0.000	0.002	0.001	0.002	0.000	0.965	0.962	0.023	0.001	0.005	0.991	5
Eurelia area, South Australia														
FBS5-11	0.908	0.041	0.001	0.002	0.001	0.000	0.000	0.953	0.999	0.005	0.000	0.005	1.010	6

Note. [a]References: (1) Hutchison (1997), (2) Zedgenizov et al. (2014a), (3) Hayman et al. (2005), (4) Davies et al. (2004), (5) Stachel et al. (2000), (6) Tappert et al. (2009a, b)

Most of the grains have compositions close to stoichiometric bridgmanite. Some deficit in both cation groups is probably caused by the presence of other, non-analyzed cations, such as P and REE, which are characteristic for this group of minerals. Judging by crystal-chemical calculations (Table 4.8), all iron substitutes for Mg^{2+} in the A site and, most likely, is in the divalent form Fe^{2+}, although studies based on Mössbauer spectroscopy by McCammon et al. (1997) suggested a significant portion of iron to be Fe^{3+}. There is no evidence for the presence of Fe^{3+} in the B site in natural bridgmanite. The three most Al-rich specimens (##BZ210; BZ241 and BZ242, all from Brazil) show an excess in alumina of 0.069–0.185. These amounts balance the deficit in cation site A of these specimens, suggesting that the location of this portion of Al most likely is in the site B, the 8/12-fold pseudo-octahedral coordination position.

4.4.4 Partition Coefficient of Iron in Natural Bridgmanite–Ferropericlase Assemblages

The analysis of the iron index fe in co-existing ferropericlase and bridgmanite grains and the partition coefficient of iron $K_D^{Brd-fPer}$ in all bridgmanite + ferropericlase assemblages shows that two groups of assemblages can be distinguished (Table 4.9; Fig. 4.20a). The first group (Group A; 84% of all pairs) forms an elongated cloud illustrating a general positive correlation between $fe_{Brd} = 0.032$–0.138 and $fe_{fPer} = 0.116$–0.363. The correlation trend is close to trend Ia from the experimental data, confirming the regularity in Fe exchange between the two major lower-mantle minerals. The second group (Group B; 16% of all grains) is composed of three specimens with almost constant $fe_{fPer} = 0.173$–0.193 and relatively high fe_{Brd}, varying from 0.088–0.120; all specimens are high-Al varieties. This group lies outside of any experimental trends. The increase in fe of both natural ferropericlase and bridgmanite from Group A is independent of the $K_D^{Brd-fPer}$ values (0.169–0.479), while Group B, which has fe values in the same range as Group A, has elevated values of $K_D^{Brd-fPer} = 0.433$–0.657 (Fig. 4.20b).

Such variations in the iron indices and the bulk iron contents in the co-existing major lower-mantle minerals differ drastically from what was expected for a pyrolitic lower mantle with a homogeneous distribution of iron in ferropericlase and bridgmanite (Kesson and Fitz Gerald 1991; Wood 2000; Lee et al. 2004). According to the experimental and theoretical data for a bulk pyrolitic composition, where the total iron content in the system was fixed at $fe = 0.09$–0.15 (Irifune et al. 2010; Vilella et al. 2015; Xu et al. 2017), we should expect a decrease of the iron content in bridgmanite with an increase of the iron content in ferropericlase. In reality, this is not the case, however, since both ferropericlase and bridgmanite demonstrate a simultaneous, well-correlated increase in fe values (Fig. 4.20a–d).

Both groups of assemblages are characterised by similar concentrations of Ni in ferropericlase, mainly corresponding to the bulk Ni contents in the mantle (6052–11,212 ppm from Group A and 9982–11,711 ppm from Group B) (Fig. 4.20c).

Table 4.9 Compositions of coexisting bridgmanite and ferropericlase included in lower-mantle diamonds (Kaminsky and Lin 2017)

Sample No.	Mineral association	Bridgmanite				Ferropericlase				$K_D^{Br-fPer}$	Refs[a]
		FeO, wt%	MgO, wt%	Al₂O₃, wt%	fe	FeO, wt%	MgO, wt%	Ni, ppm	fe		
Juina area, Brazil											
BZ120	Brd + fPer	4.63	35.39	1.23	0.069	42.81	55.25	6052	0.310	0.169	1
BZ207	Brd + fPer + Jeffbenite	9.02	32.03	2.66	0.138	43.14	54.84	7074	0.313	0.358	1
BZ210	Brd + fPer	5.14	30.21	10.04	0.088	27.20	69.22	9982	0.183	0.433	1
BZ241	Brd + fPer + Ruby	5.36	27.15	10.24	0.101	28.63	68.21	11,711	0.193	0.470	1
BZ242	Brd + fPer	3.95	16.35	12.58	0.120	25.50	69.30	11,083	0.173	0.657	1
BZ251	Brd + fPer	3.80	36.25	1.33	0.056	23.52	74.77	9825	0.152	0.333	1
14-2	Brd + fPer + Di?	4.87	33.59	1.37	0.086	31.50	65.60	9746	0.216	0.302	2
1-5	Brd + fPer	6.25	34.80	2.07	0.093	36.70	60.98	9137	0.258	0.298	3
3-2	Brd + fPer + CaSiPv + 'Ol'	4.21	33.43	1.60	0.066	25.27	72.21	10,336	0.166	0.360	3
3-5	Brd + fPer + 'Ol'	6.60	33.20	3.10	0.101	48.96	50.34	2437	0.363	0.204	3
4-3	Brd + fPer + 'Ol'	4.27	35.36	2.45	0.064	25.67	71.11	10,631	0.168	0.381	3
Northwest Territories, Canada											
DO2700100	Brd + fPer + CaSiPv + SiMg	2.85	37.90	0.69	0.041	16.80	81.60	8882	0.104	0.365	4
DO2700300	Brd + fPer + 'Ol'	2.97	37.80	0.72	0.042	23.60	73.70	11,083	0.154	0.245	4
DO27-97 14A	Brd + fPer + Ni	4.22	36.11	2.03	0.062	21.29	77.45	10,742	0.135	0.425	4
Kankan area, Guinea											
KK-103	Brd + fPer	3.39	35.92	0.61	0.050	20.11	76.98	11,004	0.129	0.388	5
KK-108	Brd + fPer Ga	4.90	34.90	1.67	0.037	22.15	75.61	10,049	0.143	0.479	5
KK-16	Brd + fPer + Siderite	3.34	35.94	0.55	0.050	22.68	75.34	11,212	0.146	0.343	5
KK-44	Brd + fPer + CaSiPv + 'Ol'	3.52	36.73	1.19	0.051	20.15	76.45	10,532	0.130	0.363	5
Eurelia area, South Australia											
FBS5-11	Brd + fPer	2.93	36.58	0.25	0.043	23.42	74.04	9550	0.152	0.253	6

Note [a]Reference numbers are the same as in Table 4.8
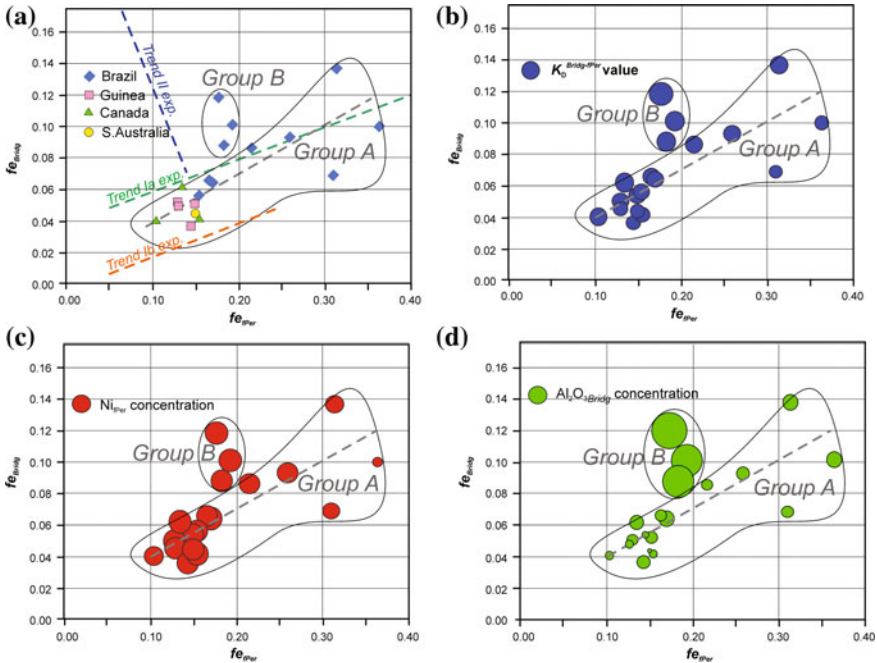
Fig. 4.20 Iron indices $fe = Fe/(Fe + Mg)_{at.}$ in coexisting ferropericlase and bridgmanite in lower-mantle diamond inclusions. **a** General plot. **b** With $K_D^{Brd-fPer}$ values, shown as *circles* proportional to the $K_D^{Brd-fPer}$ values. **c** With Ni concentrations in ferropericlase, shown as *circles* proportional to the Ni concentrations. **d** With Al_2O_3 concentrations in bridgmanite, shown as *circles* proportional to the Al_2O_3 concentrations. Four groups of samples from Brazil, Canada, Guinea, and Australia with the grains of ferropericlase and bridgmanite that associate with each other are used. From Kaminsky and Lin (2017). Used with a permission of the Mineralogical Society of America

However, one of the analyzed samples (#3-5 from Brazil) has a low concentration of Ni = 2437 ppm, and there are a number of low-Ni ferropericlase inclusions in diamond (Fig. 4.21). Analysis of the Ni content in ferropericlase as a function of the iron index shows that the ferropericlase grains with fe of approximately 0.2 in deep-diamond inclusions have Ni content close to the estimates of 8000–12,000 ppm for the bulk pyrolitic composition; however, the Ni content drastically decreases with increasing iron index in ferropericlase, especially for samples from Brazil (Fig. 4.10). The samples with fe of more than 0.6 from Brazil have Ni contents of less than 2000 ppm. Therefore, the analyses of natural ferropericlase grains show that the higher the iron index in the grain, the lower the Ni content.

There is a general (although not very strong) positive correlation between Ni and the partition coefficient of iron (Fig. 4.21). The lowest $K_D^{Brd-fPer}$ values (0.169 in sample # BZ120 and 0.204 in sample # 3-5) are characterized by the lowest Ni concentrations in ferropericlase, whereas the samples with the highest $K_D^{Brd-fPer}$ values (## BZ210, BZ241 and BZ242) are characterized by the highest Ni contents in ferropericlase.

Fig. 4.21 Variations of Ni concentrations in ferropericlase. $K_D^{Brd-fPer}$ versus Ni content in ferropericlase. From Kaminsky and Lin (2017). Used with a permission of the Mineralogical Society of America
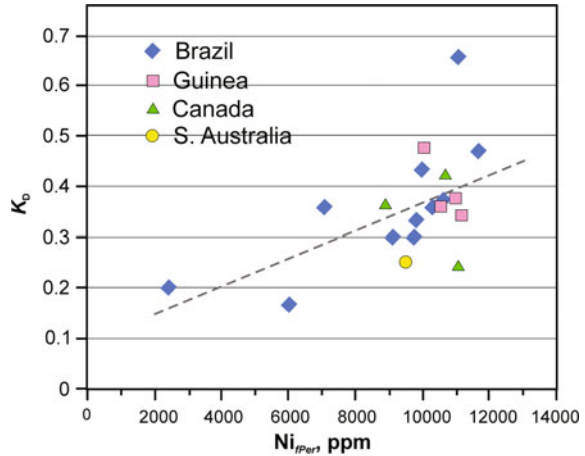
4.4.5   Role of Ni and Al in the Iron Partition Coefficient Distribution

The Ni concentration in ferropericlase indicates the presence of metallic iron phase (s) in the magmatic system of the deep mantle, as established by Frost et al. (2004). It was shown that the increasing weight fraction of the metallic phase (suggesting the conditions present within the lowermost lower mantle) leads to a decrease of Ni concentration in the lower-mantle material and also leads to a decrease in concentration of this element in coexisting ferropericlase and bridgmanite (Ryabchikov and Kaminsky 2013a, b). In this process, iron appears here as a dilutant of Ni dissolved in metal. According to experimental data (Frost et al. 2004; Frost and McCammon 2008), metal content in the lower mantle is estimated at 1 wt% (10,000 ppm) before the release of the metallic alloy. This implies that the ferropericlase grains with high Ni concentrations were formed in media that did not contain a metallic alloy (or its quantity was extremely small), suggesting that these originated within the uppermost lower mantle, while the low Ni ferropericlase grains were formed in the presence of a metallic alloy within lower parts of the lower mantle. More than 40% of the studied lower-mantle ferropericlase grains are low-Ni and high-Fe inclusions. These variations in Fe and Ni concentrations in ferropericlase point to a radial compositional gradient in the lower mantle at the time of the formation of these minerals, and the anti-correlation of Ni and Fe in ferropericlase may be applied as a qualitative criterion of the depth of its origin.

The correlation between the $K_D^{Brd-fPer}$ values and Ni concentrations in ferropericlase (Fig. 4.21) is not strong because of the presence of other elements in minerals, such as Al, Co, Mn, Na, among others. The major factor here is the Al impurity in ferropericlase and bridgmanite, which is the real cause of the existence of the two groups of associations (Fig. 4.20d). Al_2O_3 in ferropericlase and bridgmanite comprises 0.69–3.10 wt% in Group A and 10.04–12.58 wt% in Group B. In general,
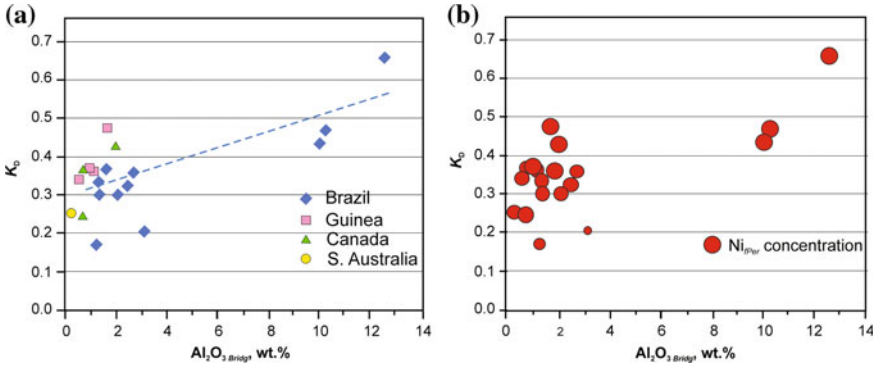
Fig. 4.22 Iron partitioning coefficient $K_D^{Brd-fPer}$ versus Al_2O_3 content in bridgmanite. **a** General plot. **b** With Ni concentrations in ferropericlase, shown as *circles*, the radii of which are proportional to the Ni contents. From Kaminsky and Lin (2017). Used with a permission of the Mineralogical Society of America

$K_D^{Brd-fPer}$ correlates with the Al_2O_3 content in ferropericlase and bridgmanite, which is particularly noticeable in the Brazilian samples (Fig. 4.22a). However, this correlation is quite weak (Fig. 4.22a, b) and is not get fully understood.

The enrichment of ferropericlase and bridgmanite with Al is strongly pressure dependent (Andrault et al. 2007). In the uppermost part of the lower mantle, Al-rich phases still exist, such as majorite and jeffbenite. In experiments at pressure conditions of 24–28 GPa, these minerals dissociate, and the released Al is incorporated into ferropericlase and bridgmanite (Irifune and Tsuchiya 2007). In the natural environment, the reverse scenario occurs: juvenile high-Al ferropericlase and bridgmanite at 24–28 GPa releases Al with the formation of Al-bearing phases, such as majorite and jeffbenite.

As a result, the following scenario can be outlined for the lower mantle. Bridgmanite has a high, 10–12 wt% concentration of Al_2O_3, which is consistent with its bulk concentration in the primitive mantle of 4–5 mol% (McDonough and Sun 1995). Al occupies its position in both cation sites, A and B. In each case, Al substitutes Si and divalent cations with oxygen-vacancy formation:

$$2^{VIII/XII}Al^{3+} + O^{2-} \rightarrow 2^{VIII/XII}(Mg, Fe)^{2+} + V^0; \text{ and}$$
$$2^{VI}Al^{3+} + V^0 \rightarrow 2^{VI}Si^{4+} + O^{2-};$$
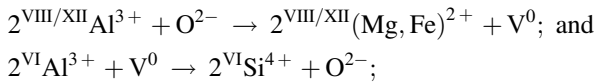
In the case of Al positioning in both A and B sites, a charge-coupled mechanism (CCS) takes place, for which no oxygen vacancies are required for charge balance (Richmond and Brodholt 1998):

$$^{VI}Al^{3+} + ^{VIII/XII}Al^{3+} \rightarrow ^{VI}Si^{4+} + ^{VIII/XII}(Mg, Fe)^{2+};$$
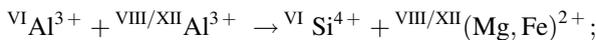
which, according to theoretical calculations, dominates at lower-mantle pressures
and temperatures (Akber-Knutson and Bukowinski 2004). The concentration of Al
in ferropericlase and bridgmanite, particularly in the A site may indicate the depth
of the minerals' origin because previous studies have shown that Al concentration
in bridgmanite increases with increasing pressure along a representative
lower-mantle geotherm (Irifune et al. 2010). Recently, an experimental study of the
system $MgSiO_3$–Al_2O_3 under pressures up to 52 GPa and 2000 K, with the use of
sintered diamond anvils combined with in situ synchrotron X-ray diffraction
observations in a multi-anvil apparatus, demonstrated that the Al_2O_3 content in
bridgmanite increases from 12 mol% at 27 GPa to 29 mol% at 52 GPa, suggesting
that the Al_2O_3 content in bridgmanite can be used as a pressure indicator at pres-
sures of above 30 GPa (Liu et al. 2016). As shown in Sect. 4.2.2, iron in fer-
ropericlase and bridgmanite is in the A site, most likely in a ferrous divalent form.
Ferropericlase with depth (and correspondingly increasing pressure) has a
decreasing concentration of Ni and increasing *fe* values, reflecting the increase in
the iron content in the lower mantle. The decrease of Ni content in ferropericlase
may be used as another qualitative geobarometer in the lower mantle. In contrast to
experimental conditions, most of which were performed with pyrolitic composi-
tions (*fe* = 0.05–0.15), the results on natural samples show that iron indices in
ferropericlase and bridgmanite have a positive correlation (Fig. 4.20), demon-
strating the total enrichments of the lower-mantle media in iron. This enrichment is
correlated with the Ni (negatively, Fig. 4.20c) and Al_2O_3 (positively, Fig. 4.20d)
concentrations, each of which is an independent criterion of the increasing pressure.
One may conclude that the Fe content of the lower mantle increases with depth, in
contrasr to the pyrolitic composition.

   This scenario plays only a small part of a more complicated picture for existing
phases within the lower mantle, which incorporates other mineral phases and is
characterized by changeable conditions within an open, natural system. It explains
the controversies in the aforementioned high P–T experimental results carried out
for standard closed systems.

4.4.6 Regional Differences in the Distribution of Iron in Ferropericlase and Bridgmanite

There are observed differences in the iron index of ferropericlase values and related
characteristics from different regions. For example, ferropericlase from Canada,
South Australia and South Africa have *fe* = 0.10–0.20, which is close to the
pyrolite values. Ferropericlase from Guinea, along with similar *fe* values, also has
higher *fe* values of 0.25. Moreover, iron-rich ferropericlase from Brazil (reaching
the composition of magnesiowüstite) comprises almost half of all grains in this
region (c. 46.5%). It has been suggested that such differences represent the different
depths of the host diamonds sampled in the lower mantle. In a pyrolitic lower

mantle, the average amount of iron in the lower-mantle minerals are commonly believed to be close to 10%, chiefly distributed between ferropericlase and bridgmanite and ferropericlase phases (Irifune et al. 2010). The analysis of the iron indices in these phases have shown that the total iron content in some of these minerals can be much higher than what is expected for a 'normal' lower mantle. As shown in Fig. 4.9, the occurrence of these 'anomalous', high-Fe ferropericlase and high-Fe ferropericlase and bridgmanite pairs with $fe = 0.17–0.36$ and $0.07–0.14$, respectively, indicates that the lower mantle is chemically inhomogeneous with respect to the iron content at least in certain regions where these assemblages originated.

4.4.7   Major Differences in Iron Partitioning Between Natural Samples and Mineral Physics Results

Recent theoretical calculations considering a wide range of oxygen fugacity conditions and different iron spin and valence states in the lower-mantle pyrolite assemblage have further indicated that the Fe^{3+} content in ferropericlase and bridgmanite decreases with increasing depth in the lower mantle; at lowermost lower mantle conditions, Fe^{3+} content in ferropericlase and bridgmanite becomes almost negligible (Xu et al. 2017). However, our analyses of the natural ferropericlase and bridgmanite and ferropericlase assemblages show that most of the iron in the A site of the ferropericlase and bridgmanite lattice is in the Fe^{2+} state, which contradicts these mineral physics studies.

High P–T experiments have shown that the partition coefficient $K_D^{Brd-fPer}$ is observed to increase from approximately 0.5 at 23 GPa up to 0.85 at approximately 28 GPa ($\sim$800 km in depth. This can be associated with the Al^{3+}–Fe^{3+} coupled substitution in ferropericlase and bridgmanite in a pyrolitic composition, where iron ions partition almost equally between the ferropericlase, and the ferropericlase and bridgmanite lattices (Irifune et al. 2010). Results from such high P–T experiments showed that the $K_D^{Brd-fPer}$ value stays almost constant at $\sim$0.85 at pressures of 28–40 GPa ($\sim$800–1000 km in depth) and then notably decreases to 0.4–0.5 with increasing pressures of 40–50 GPa (1000–1200 km in depth) (Irifune et al. 2010). This dramatic decrease is most likely associated with the spin transition of Fe^{2+} in ferropericlase, which results in a volume collapse of about 2% (Lin et al. 2013) promoting iron ions in ferropericlase and bridgmanite to favorably partition into the low-spin ferropericlase, which is energetically more stable than the high-spin ferropericlase and bridgmanite and ferropericlase. Without the alumina substitution in ferropericlase and bridgmanite at such conditions, the $K_D^{Brd-fPer}$ values decrease to approximately 0.2 (Sakai et al. 2009), i.e., lower than the value suggested from high P–T experiments using a pyrolitic composition (Irifune et al. 2010). That is, in an alumina-poor environment in the lower mantle, such as the olivine-rich peridotite environment, the $K_D^{Brd-fPer}$ value is expected to remain low at approximately 0.2

with or without the spin transition effect. If the lower mantle is chemically pyrolitic, these changes in the iron partitioning indicate that the deeper parts of the lower mantle (especially toward the lowermost parts) would likely contain iron-enriched, low-spin ferropericlase and iron-poor, alumina-rich ferropericlase and bridgmanite. By contrast, in the upper parts of the lower mantle, especially at approximately 800 km in depth, iron would almost equally partition between bridgmanite and ferropericlase (Irifune et al. 2010). However, a comparison of these experimental results with our analyses on natural samples clearly shows contradicting $K_D^{Brd-fPer}$ values; the natural samples show very diverse $K_D^{Brd-fPer}$ values that cannot be simply explained by the alumina dissolution in ferropericlase and bridgmanite and the spin transition of Fe^{2+} in ferropericlase. These major differences in the iron indices and $K_D^{Brd-fPer}$ values demonstrate the complex, inhomogeneous iron speciation and chemistry in the lower mantle, which are well beyond the knowledge of current mineral physics studies.

4.4.8   Conclusions

One may conclude, based upon determined iron contents in natural ferropericlase and bridgmanite, and on the distribution of the partition coefficient of iron in natural bridgmanite + ferropericlase assemblages that some areas in the deep lower mantle are iron-rich and differ markedly from a pyrolitic composition. In the lowermost lower mantle, ferropericlase is also Ni-poor, demonstrating the presence in the mineral-forming environment of a free metallic phase; bridgmanite is Al-rich.

The juvenile iron partitioning in the bridgmanite + ferropericlase association $K_D^{Brd-fPer}$ is as low as 0.1–0.2. During the crystallization of diamonds at a relatively more shallow depth in the lower mantle, in which $K_D^{Bridg-fPer}$ increases to 0.4–0.5, and even as high as 0.7, they trap and deliver to the surface such associations. This regularity, established in geological samples, was supported by recently published theoretical calculations by Muir and Brodholt (2016), showing a decrease of $K_D^{Brd-fPer}$ with depths from 0.32 to 0.06.

The details of the element partitioning between natural ferropericlase and ferropericlase, in the lower mantle (at least in some areas), are as follows:

- According to crystal-chemical calculations, iron in ferropericlase and bridgmanite is ferrous Fe^{2+} in the A site, substituting for Mg^{2+};
- Almost all iron in ferropericlase is ferrous Fe^{2+}; the share of ferric Fe^{3+} iron in ferropericlase is $Fe^{3+}/\Sigma Fe = 8$–12 at.%; Fe^{3+} is concentrated in exsolved clusters of $Mg_{1+x}Fe^{3+}{}_{2-x}O_{4-x/2}$, while all remaining iron in ferropericlase is in the ferrous, Fe^{2+} state;
- Iron contents in both ferropericlase and bridgmanite increase with depth (pressure), reflecting the increasing Fe content in the lower part of the lower mantle;

- Al content in ferropericlase and bridgmanite from the lower part of the lower mantle is at $\sim$10–12 wt% Al_2O_3;
- Al in bridgmanite is mainly in the cation B site and partly in the cation A site, in both cases substituting Si, Mg and Fe with vacancy formation; and in the case of Al positioning in both, B and A sites, a charge-balanced reaction takes place.

These observations in natural samples cannot be simply explained by the dissolution of Al in ferropericlase and bridgmanite and the spin transition of Fe^{2+} in ferropericlase. The differences between observations in natural samples and experimental results should be taken into account in future calculations and experimental works.

4.5   CaSiO₃ Perovskite

4.5.1   General

CaSi-perovskite $CaSiO_3$ is considered to be the third most abundant mineral in the lower mantle with a 5–10 wt% abundance in the pyrolite model (Akaogi 2007; Irifune et al. 2010; Tsuchiya and Kawai 2013). The percentage volume of CaSi-perovskite in the subducted mid-oceanic ridge basalt could be as high as 21–29%, such that its presence will lower the Mg/Si ratio of the lower mantle and thus influence the mineralogy of the region (Funamori et al. 2000; Hirose et al. 1999; Perrillat et al. 2006). Ca cation in CaSi-perovskite is much larger in the ionic radius than two other common abundance cations, Mg and Fe, and is not soluble in bridgmanite, in which its A and B sites cannot accommodate the larger Ca cation. In the relevant lower-mantle P–T conditions, CaSi-perovskite is stable in the cubic crystal structure from the transition zone to the lowermost part of the lower mantle (Shim et al. 2000a). In deep-diamond inclusions, CaSi-perovskite forms small, colorless or milky-white grains with an anhedral or characteristic 'negative' euhedral shape (Fig. 4.23). It associates with bridgmanite, ferropericlase and coesite (formerly stishovite), as well as with CaTi-perovskite, jeffbenite, merwinite, majorite, 'olivine', and native Ni (Kaminsky 2012; Zedgenizov et al. 2016). Within diamonds, delivered to the surface, CaSi-perovskite acquires a retrograde structure, like that of larnite or walstromite (Gasparik et al. 1994; Joswig et al. 1999).

Some samples, where $CaSiO_3$ associates not with bridgmanite and ferropericlase, but with Ca_2SiO_4 and $CaSi_2O_5$, were identified within several Guinean and Brazilian diamonds (Stachel et al. 2000; Hayman et al. 2005; Anzolini et al. 2016a; Burnham et al. 2016; Zedgenizov et al. 2016). This association of walstromite $CaSiO_3$ + larnite β-Ca_2SiO_4 + titanite $CaSi_2O_5$, on the basis of the in situ XRD and micro-Raman spectroscopy, combined with thermodynamic calculations, is believed to be formed at $\sim$9.5–11.5 GPa and 1500 K. In the natural environment, this may be a retrograde product of perovskite-structured $CaSiO_3$ at a pressure of 10–12 GPa.
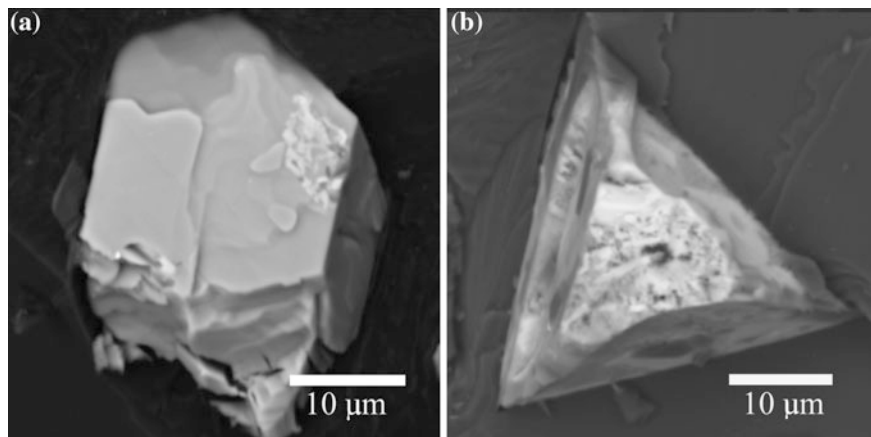
Fig. 4.23 Grains of CaSi-perovskite extracted from diamonds of the Rio Soriso area. SEM image. From Hayman et al. (2005)

4.5.2 Chemical Composition of Natural CaSiO$_3$ Perovskite

During the course of retrograde phase transitions, the composition of CaSi-perovskite remains unchanged and remarkably clean, with only minor admixtures of Mg, Ti, Al, Fe, Sr and K (Tables 4.10 and 4.11).

The major admixtures are Ti and Al. Most samples have low concentrations of these elements, less than 0.7 wt% Al$_2$O$_3$ and less than 0.6 wt% TiO$_2$, forming Group 1 (Fig. 4.24). Some samples have elevated concentrations of TiO$_2$, from 2.13 to 6.65 wt%, with a similar Al$_2$O$_3$ content (0.20–0.56 wt%), forming Group 2. Experimental data indicate that CaSiO$_3$ and CaTiO$_3$ are immiscible phases at low (below 9 GPa)-pressure conditions (Kubo et al. 1997). It is possible that at the lower-mantle conditions, the solubility of Ti increases with pressure. After the release of inclusions from host diamonds, dissociation occurs: Ti-phase forms either isolated CaTiO$_3$ grains in the CaSiO$_3$ matrix or symplectitic intergrowths of both phases (Zedgenizov et al. 2016).

A separate group is formed by Ca(Si,Ti)O$_3$ compositions with TiO$_2$ = 23–53 wt % reaching an almost stoichiometric CaTiO$_3$ composition. In individual diamonds, Ca–Ti-perovskite was found either as isolated inclusions or in association with majoritic garnet, SiO$_2$, ilmenite and a Si–Mg phase (Kaminsky et al. 2001; Hayman et al. 2005; Zedgenizov et al. 2014a, 2016). Inclusions of Ca–Ti-perovskite contain minor SiO$_2$ (1.1–3.9 wt%) and Al$_2$O$_3$ (0.6–2.3 wt%). The negative Al–Ti trend in this group indicates the replacement of Si with Ti in cation Group B. In this case, an oxygen vacancy should be expected from the result of the substitution: $2^{B}Si^{4+} \rightarrow 2^{B}Al^{3+} + V^{0}$. Some of these compositions may be titanite.

In high-pressure experiments performed on high-Al CaSi-perovskite (CaSi$_{0.5-0.6}$Al$_{0.4-0.5}$O$_{2.75-2.8}$) at pressure conditions below 18 GPa (i.e., corresponding to the

Table 4.10 Representative compositions of CaSi-perovskite inclusions in diamond from different areas (wt%)

Country	Brazil				Machado	Canada	Guinea	
Area	Juina					Northwest Territories	Kankan	
Location	São Luiz placer			Corrigo Chicoria placer	Placer	Panda pipe	Placer	
Sample No.	BZ115	13	31-1	5-104a	P28-1b	PA-50c	KK-44g	KK-87a
Mineral association	CaSiPrv	CaSiTiPrv + Brd + Jeffbenite	CaTiSiPrv + Maj + SiO2 + Ky	CaSiPrv + Ni	CaSiPrv + Di	CaSiPrv + fPer	CaSiPrv + Brd + fPer + 'Ol'	CaSiPrv + fPer
SiO$_2$	50.59	47.30	3.94	51.23	49.98	51.13	51.33	51.11
TiO$_2$	0.01	6.65	52.70	0.04	0.03	0.01	0.01	0.07
Al$_2$O$_3$	0.08	0.32	2.34	0.06	0.04	0.09	0.06	0.66
Cr$_2$O$_3$	0.01	0.03	0.00	n.a.	<0.04	0.01	0.00	0.03
FeO	0.16	0.09	0.00	0.06	0.16	0.04	0.04	0.10
NiO	0.02	n.a.	n.a.	0.03	0.02	0.00	0.00	0.00
MnO	0.02	0.00	0.00	0.05	<0.04	0.04	0.02	0.05
MgO	0.14	0.00	0.00	n.a.	0.49	0.10	0.03	0.09
CaO	48.49	43.00	40.10	48.37	47.22	47.90	47.70	45.80
SrO	n.a.	n.a.	n.a.	n.a.	n.a.	0.10	0.21	0.85
Na$_2$O	0.02	0.02	0.00	n.a.	0.04	0.02	0.07	0.05
K$_2$O	n.a.	0.01	0.00	n.a.	0.08	0.10	0.03	0.73
P$_2$O$_5$	n.a.	n.a.	n.a.	n.a.	n.a.	0.01	0.00	0.02
Total	99.54	97.47	99.14	99.84	98.06	99.54	99.50	99.57
fe	0.325	–	–	0.428	0.155	0.197	0.379	0.386
mg	0.675	–	–	0.572	0.845	0.803	0.621	0.614
References	Hutchison (1997)	Zedgenizov et al. (2014a)		Kaminsky et al. (2001)	Burnham et al. (2016)	Tappert et al. (2009a)	Stachel et al. (2000)	

Note: *n.a.* not analysed

Table 4.11 Minor elements in CaSi-perovskite (wt%)

Oxides	Brazil				Guinea	Canada	
	Rio São Luiz	Rio Vermelho and Chicoria	Rio Soriso	Juina-5 pipe	Kankan	DO-27 and A21 pipes	Panda pipe
MgO	0–0.46	n.a.	0.05–0.35	0–0.30	0.03–0.09	0	0.10
TiO_2	0–6.65	0.04–0.26	0.10–2.13	0.02–0.64	0.01–0.07	0	0.01
Al_2O_3	0–1.52	0.03–0.11	0.21–0.26	0.14–6.27	0.03–0.66	0–0.02	0.09
SrO	n.a.	0.01–0.06	n.a.	n.a.	0.06–0.85	n.a.	0.10
K_2O	0–0.02	0–0.07	0–0.14	0.01–0.11	0.01–0.73	0–0.07	0.10
References	Wilding et al. 1991, Harte et al. (1999)	Kaminsky et al. (2001)	Hayman et al. (2005)	Thomson et al. (2014)	Stachel et al. (2000)	Davies et al. (2004)	Tappert et al. (2009a)

Note: *n.a.* not analysed

Fig. 4.24 Al_2O_3 versus TiO_2 in natural CaSi-perovskite
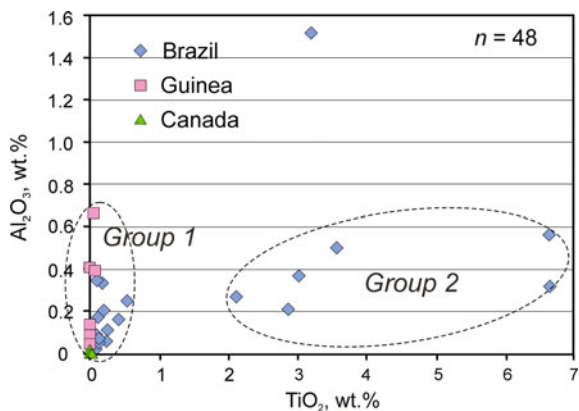
transition zone), oxygen defects occur in pseudo-cubic (111) layers in well-ordered ten- or eight-fold superstructures (Bläß et al. 2007).

Similar to bridgmanite, a charge-coupled substitution (CCM) $2Al^{3+} \rightarrow Si^{4+} + Ca^{2+}$ may also be suggested; however, for the CaSi-perovskite, the occupation of a larger calcium site by a relatively small trivalent aluminium cation is less favorable and limits the maximum amount of Al incorporated by a charge-coupled substitution to, at most, 6 mol% (Takafuji et al. 2002). The amount of Al incorporated into natural CaSi-perovskite may be limited to this amount. For CaSi-perovskite samples analyzed to date, a compositional gap between CaSi- and CaTi-perovskites occurs (Fig. 4.24), but it remains unclear whether this gap exists in nature. Furthermore, two low-Ti samples of CaSi-perovskite show anomalously high Al concentrations, 1.52 and 6.27 wt%

Al$_2$O$_3$ (Fig. 4.24). The nature of this anomaly remains unclear. The explanation that these samples belong to the mafic association has not been excluded.

The Mg concentration in CaSi-perovskite does not exceed 0.35% MgO. In some experiments, up to 10% Mg can be substituted into CaSi-perovskite at 55 GPa (Armstrong et al. 2012). This effect was enhanced with pressure, temperature, and the substitution of Ti^{4+} for Si^{4+}, with Mg–Ca forming a complete solution at 97 GPa for modest amounts of Ti substitution (Ti/(Ti + Si) = 0.05). However, in analyzed natural Ca(Si,Ti)O$_3$ compositions MgO was not detected at all.

CaSi-perovskite/melt partition coefficients for REE are much higher than those for bridgmanite (some by a factor of 1000) (Righter et al. 2014), causing high concentrations of REE (up to 2–3 magnitude orders) in CaSi-perovskite (Fig. 4.25). In contrast to bridgmanite and ferropericlase-magnesiowüstite, the REE patterns in CaSi-perovskite show significant enrichment in LREE (e.g., ratios of La/Yb = 3.6–37.7; Fig. 4.25). Some CaSi-perovskite grains show positive Eu-anomalies, which are possibly attributable to the composition of subducted lithospheric slabs. Such grains most likely belong to the mafic association. This type of pattern may be explained by a significant increase in the crystal-liquid partition coefficient for LREE, compared with HREE, with increasing pressure (Wang et al. 2000). In this case, LREE enrichment may be a potential qualitative geobarometer. The general enrichment of CaSi-perovskite in incompatible elements is caused by much larger (roughly by one order of magnitude) crystal-liquid partition coefficients of trivalent and tetravalent cations in the CaSi-perovskite in comparison with bridgmanite
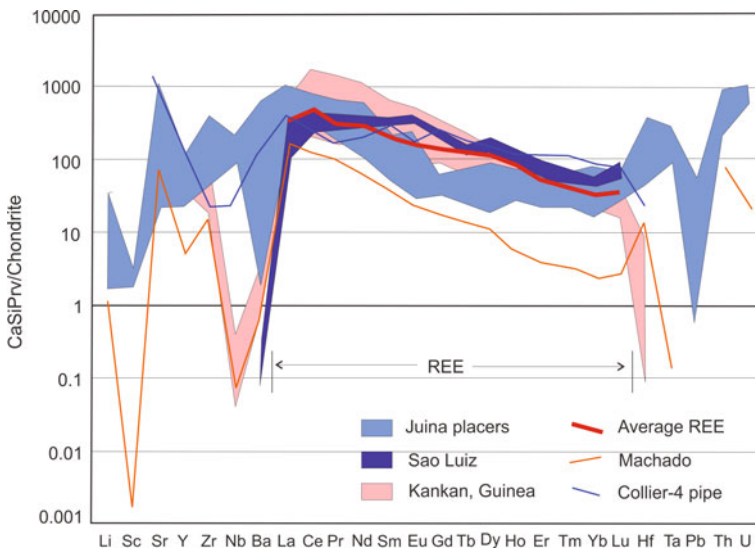
Fig. 4.25 Chondrite-normalised trace element patterns in natural CaSi-perovskite. Data from Wang et al. (2000), Kaminsky et al. (2001), Stachel et al. (2000), Bulanova et al. (2010), Harte et al. (1999), Burnham et al. (2016). Chondrite composition was derived from McDonough and Sun (1995). Modified after Kaminsky (2012), with additions

(Wood and Corgne 2009). The patterns of partitioning of trace elements into $CaTiO_3$ and $CaSiO_3$ perovskites are virtually identical (Corgne and Wood 2002). The major implication of the partitioning data is that, despite being a volumetrically minor phase, CaSi-perovskire is the major host for the heat-producing elements Th and U in the deep Earth, as well as being the principal reservoir for the REE (Corgne et al. 2005). Perry et al. (2017), on the basis of DFT calculations, suggested that CaSi-perovskite may be a concentrator of U and Th in the lower mantle.

4.5.3   Crystal Structures and Phase Transitions

Cubic structure. In early theoretical predictions and high-pressure XRD experiments including those performed in DAC, CaSi-perovskite was thought to have a cubic structure (Fig. 4.26a) with a space group $Pm3m$ under pressures of up to 134 GPa at room temperature (Liu and Ringwood 1975; Mao et al. 1989; Tarrida and Richet 1989; Wang and Weidner 1994; Wentzcovitch et al. 1995; Warren et al. 1998; Shim et al. 2000a, b). No structural transformations were observed in these studies, and CaSi-perovskite was considered as 'an invisible' component of the lower mantle in view of the similarity of its density with that given by the standard Earth model, PREM (Tarrida and Richet 1989).
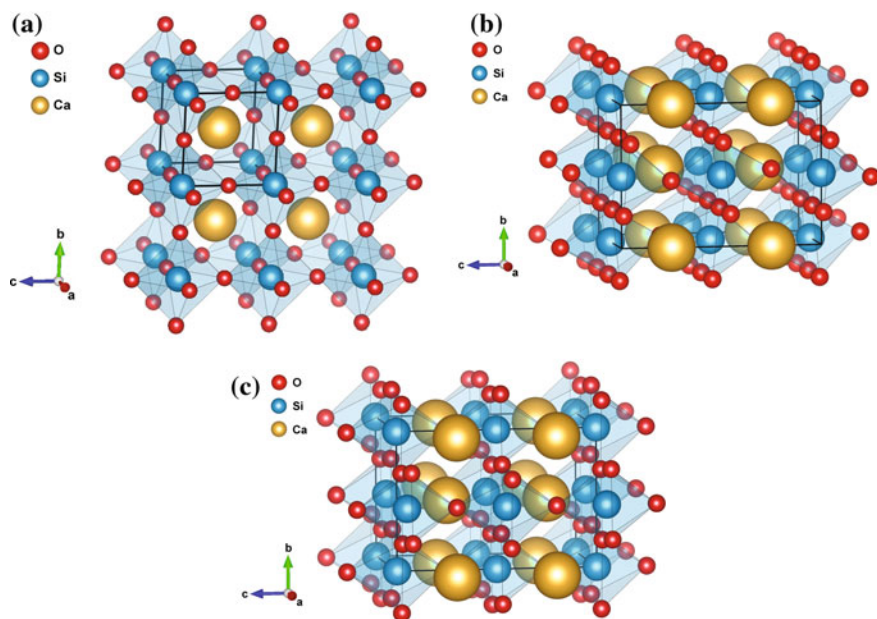
Fig. 4.26 Crystal structures of $CaSiO_3$ polymorphs: **a** Cubic B1 (space group $Pm3m$); **b** Tetragonal (space group $I4/mcm$); **c** Orthorhombic (space group $Pbnm$). Lattice parameters from Jung and Oganov (2005)

Tetragonal structure. Stixrude et al. (1996) were the first to propose, on the basis of theoretical first-principle linear-response calculations, that, as a result of slight rotations of the SiO_6 octahedra, a slightly distorted tetragonal structure with a space group *I4/mcm* should be the stable phase of $CaSiO_3$ at high pressures and 0 K, instead of the cubic phase predicted previously (Fig. 4.26b). Stixrude et al. (1996) suggested that the cubic perovskite structure undergoes a phase transition to tetragonal $CaSiO_3$ at above 2200 K at 80 GPa. However, this transition temperature estimate was apparently too high, according to further experiments and calculations (Shim et al. 2002; Kurashina et al. 2004). Later, Shim et al. (2002), using a LHDAC coupled with synchrotron angle-dispersive XRD, shows that the symmetry of $CaSiO_3$ at 20–46 GPa and at room temperature was indeed tetragonal, but the space group *I4/mcm* was not consistent with their experimental results. Subsequent theoretical first-principle calculations show again that the *I4/mcm* tetragonal structure is stable up to at least 150 GPa at 0 K (Caracas et al. 2005; Jung and Oganov 2005; Adams and Oganov 2006); this was confirmed by XRD studies that show that the cubic phase is also stable under high pressure-temperature conditions relevant to the lower mantle (Kurashina et al. 2004; Ono et al. 2004, 2005; Murakami et al. 2005; Komabayashi et al. 2007). This structural transition in CaSi-perovskite was also observed by Ono et al. (2004) and Murakami et al. (2005) in a multi-component peridotite system using XRD in a laser-heated DAC. They demonstrated that CaSi-perovskite takes a cubic structure on heating above 2000 K while it had a tetragonal structure at room temperature. In XRD experiments, the cubic phases at high temperatures exhibits a diffraction peak with a small full width at half maximum (FWHM); across the tetragonal transition, this peak splits into the 004 and 220 peaks in the tetragonal structure (Sun et al. 2016). This transition is shown to be a second-order structural phase transition. However, these studies did not put tight constraints on the *P–T* conditions of the phase transition boundary.

The summary of experimental data on $CaSiO_3$ is presented in Table 4.12; the general diagram of the established phase transactions is presented in Fig. 4.27.

According to experiments performed by Kurashina et al. (2004) and Komabayashi et al. (2007) in pure CaSi-perovskite, at a fairly low temperature of 490–580 K at 52–60 GPa, the cubic CaSi-perovskite transforms to the tetragonal $CaSiO_3$ phase. Temperature uncertainties in Kurashina et al. (2004) were significantly large because of the use of the LHDAC with a large temperature gradient and uncertainties in temperature measurements. Komabayashi et al. (2007) determined the phase transition in pure CaSi-perovskite by a combination of externally heated DAC (EHDAC) and in situ synchrotron XRD measurements. Contrary to the laser-heated DAC techniques, the uncertainty in temperature is very small (approximately 5 K) in the present EHDAC experiments.

Theoretical computations based on density functional theory suggested much higher transition temperatures at high pressures ranging from 1150 K near 0 GPa to 2450 K at 136 GPa and $\sim$1600 K at 60 GPa (Stixrude et al. 2007). The DFT calculations do not agree as well with those based on molecular dynamics

Table 4.12 Comparison of theoretical and experimental studies of $CaSiO_3$

Authors	Structure	Method[a]
Wentzcovitch et al. (1995)	Cubic	LDA pseudopotential calculation
Chizmeshya et al. (1996, 1998)	Cubic is unstable at lower-mantle conditions	DFT within LDA
Stixrude et al. (1996)	Tetragonal Cubic is unstable at all pressures	Linear augmented plane wave with LDA
Warren et al. (1998)	Cubic	LDA pseudopotential calculations
Shim et al. (2000a)	Cubic	LHDAC with double-side heating technique and energy-dispersive XRD
Shim et al. (2000a, b)	Tetragonal	LHDAC with high-resolution synchrotron energy dispersive XRD
Akber-Knutson et al. (2002)	Orthorhombic at all mantle pressures	DFT—VIB method calculations
Magyari-Köpe et al. (2002a, b)	Orthorhombic	Total-energy calculations
Kurashina et al. (2004)	Low T: tetragonal High T: cubic With Al admixture T increases and orthorhombic $CaSiO_3$ appears	LHDAC with In situ XRD
Ono et al. (2004, 2005)	Low T: tetragonal High T: cubic	LHDAC with in situ XRD
Caracas et al. (2005)	Tetragonal	DFT calculations
Hirose et al. (2005)	Low T: tetragonal High T: cubic With Al admixture T increases	LHDAC with In situ XRD
Murakami et al. (2005)	Cubic under high T = 2450 K up to 114 GPa	LHDAC with double-side heating technique and angle-dispersive XRD
Jung and Oganov (2005)	Orthorhombic up to 14.2 GPa, then tetragonal	DFT with GGA-PAW calculations
Adams and Oganov (2006)	Low T: orthorhombic Medium T: tetragonal High T: cubic	First-principles molecular dynamics calculations
Li et al. (2006)	Low T: orthorhombic, Medium T: tetragonal High T: cubic	First-principles molecular dynamics calculations
Komabayashi et al. (2007)	Low T: tetragonal High T: cubic	EHDAC with in situ XRD
Stixrude et al. (2007)	Low T: tetragonal High T: cubic Low P: orthorhombic	DFT calculations
Sun et al. (2016)	Low T: tetragonal High T: cubic	LHDAC with angle dispersive XRD

Notes: [a]*DFT* density functional theory; *EHDAC* externally-heated diamond anvil cell; *GGA* generalised gradient approximation; *LDA* local density approximation; *LHDAC* laser-heated diamond-anvil cell; *PAW* projector augmented wave; *VIB* variationally induced breathing; *XRD* X-ray diffraction

Fig. 4.27 Phase diagram for pure (*black lines*) and Al-containing (*blue lines*) CaMgSiO$_3$ under high pressure and temperature. Data from Zerr et al. (1997), Kurashina et al. (2004), Ono et al. (2004), Hirose et al. (2005), Adams and Oganov (2006); Komabayashi et al. (2007), Stixrude et al. (2007). Mantle adiabate after Katsura et al. (2010)
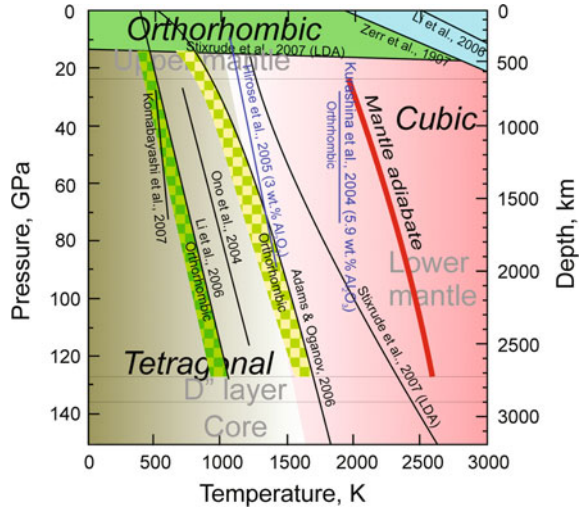
calculations (Adams and Oganov 2006; Li et al. 2006), and, in any case, these results show that the phase boundary is lower than the expected normal mantle geotherm. In the natural environment, near the normal geotherm conditions within an interval of 30–106 GPa and up to 2600 K, pure CaSi-perovskite has a cubic structure, and no phase transition occurs (Fig. 4.27). This means that the tetragonal to cubic phase transition in CaSiO$_3$ is not pressure-dependent but temperature-dependent with a slightly positive dT/dP slope of 1.1 ($\pm$1.3) K/GPa (Komabayashi et al. 2007), confirming earlier calculations with the use of DFT calculations based on the Variationally Induced Breathing (VIB) method, showing that structural and energy differences between the orthorhombic and cubic lattices under static conditions are small, and increase only slightly with pressure (Akber-Knutson et al. 2002).

   Orthorhombic structure. At the same time, Magyari-Köpe et al. (2002b) calculated, using the total-energy method, that the *Pbnm* orthorhombic phase of CaSiO$_3$ (Fig. 4.26c) at low temperatures is energetically more favourable than the cubic polymorph, and that the transition between these phases shows weak pressure dependence. Based on calculated diffraction patterns, Li et al. (2006) concluded that the orthorhombic structure (the space group was not identified) is stable at 0 K but transforms to a tetragonal structure at room temperature with a Clapeyron slope of approximately 5 K/GPa from the orthorhombic phase to the tetragonal phase (Fig. 4.27). At high pressure, the orthorhombic phase is the stable room temperature phase, while at low pressure the tetragonal field covers room temperature. To date, there has been no experimental confirmation of the orthorhombic-cubic phase transformation, and DFT calculations suggest that the observation of an orthorhombic phase in the molecular dynamics simulations is an artifact of finite reciprocal space sampling (Stixrude et al. 2007).

The admixture of Al_2O_3 enhances the distortion of the perovskite structure, and increases the transition temperature remarkably. The cubic transition boundary in $CaSiO_3$ increases from 550–1900 K at 60 GPa with increasing Al_2O_3 content from 0–5.9 wt% (Kurashina et al. 2004). For $CaSiO_3$ perovskite with 3 wt% Al_2O_3, the transition is located at approximately 1200 K at 50 GPa (Hirose et al. 2005). However, this appears to not be applicable in natural ultramafic systems because CaSi-perovskite in ultramafic association contains less than 1 wt% Al_2O_3; it varies from 0.01 to 0.66 wt% (Kaminsky 2012) such that the expected transition temperature in such Al-poor $CaSiO_3$ perovskite in the lower mantle is too low to be of any geophysical significance. The cubic–tetragonal structure transition of $CaSiO_3$ may be expected only in subducted cold lithospheric slabs for Al-rich $CaSiO_3$ perovskite containing up to 4.49 wt% Al_2O_3 (see Sect. 5.2.2).

4.5.4   Physical Properties

This phase transition in CaSi-perovskite from tetragonal to cubic is a second-order structural phase transition without any volume change since the structure of low-temperature phase (tetragonal) merges continuously with that of the high-temperature cubic phase with increasing temperature (Komabayashi et al. 2007). On the other hand, this phase transition may cause drastic changes in physical properties; in particular, it may cause a significant reduction in the shear modulus if it is accompanied by an elastic softening (Stixrude et al. 1996; Caracas et al. 2005). It is known that many distorted perovskites exhibit ferroelastic behaviour, in which acoustic velocity, thermal expansion, and heat capacity show the large anomalies near the phase transitions to higher-symmetric structures (Carpenter and Salje 1998). If the phase transition in CaSi-perovskite is also ferroelastic-type, a large decrease in S-wave velocity is expected to occur at the phase boundary.

Such a transition is possibly accompanied by significant anomalies in elastic properties (Stixrude et al. 1996) and may, therefore, have relevance for the interpretation of seismic profiles. The tetragonal to cubic transition in CaSi-perovskite, like in SiO_2 transitions (see Sect. 4.6), may be a ferroelastic-type that is associated with elastic anomalies, and may cause large seismic anomalies in a wide depth range (Hirose et al. 2005; Carpenter 2006). Acoustic velocity in such perovskites drops remarkably (up to 30%), across the structural transition from low to high symmetry phases, which are well pronounced for shear waves V_s, rather than for compressional waves V_p, resulting in unusually large ratios $d(\ln V_s)/d(\ln V_p)$ which may explain the lateral heterogeneities of seismic velocities in the lower mantle (Yeganeh-Haeri et al. 1989; Carpenter and Salje 1998). Phase transition in CaSi-perovskite possibly causes significant seismic anomalies. Since the ρ and V_Φ profiles of CaSi-perovskite are very close to PREM seismic profiles (Dziewonski and Anderson 1981), the variation in the fraction of $CaSiO_3$-perovskite with respect to the relative bridgmanite to ferropericlase ratio in the lower mantle has been suggested to not be seismically detectable (Sun et al. 2016).

4.6 Silica SiO$_2$

4.6.1 General

Free silica SiO$_2$ is not characteristic of the upper mantle that typically comprises ultramafic to mafic rock assemblages. It was not expected in the lower-mantle ultramafic assemblage model (Fig. 3.3). However, it appeared to be a common member of the natural ultramafic association where it coexists as an inclusion in diamond with ferropericlase and CaSi-perovskite and comprises 1.1–20% (average: 8.4%) (Kaminsky 2012). Silica inclusions were identified in all sets of the lower-mantle minerals observed in diamond from all regions and areas: 2.6–7.3% from Rio São Luiz (Harte et al. 1999; Zedgenizov et al. 2014a), 1.1% from Rio Soriso (Hayman et al. 2005), 4.8% from other placer deposits in the Juina area, Brazil (Kaminsky et al. 2001), 8.2% from the Kankan area, Guinea (Stachel et al. 2000), and 10–20% from Canadian kimberlites (Davies et al. 2004; Tappert et al. 2005a, b).

The composition of natural silica inclusions is found to be close to pure SiO$_2$, but some grains contain small (less than 0.09 wt%) amounts of Al, Ti, Cr, Fe, Mn, Ni, Mg, and Ca. Due to the lack of in situ structural determinations of silica from the juvenile ultramafic association, the crystal forms of these silica inclusions in association with characteristic lower-mantle minerals, such as ferropericlase and CaSi-perovskite, remain unkown. Since CaSi-perovskite is stable only at pressures greater than 14–16 GPa, i.e. in the stability field of stishovite, the SiO$_2$ should be stishovite. However, because of the instability of stishovite in these inclusions of silica after extraction from host diamonds, it typically shows up as a retrograde quartz structure.

4.6.2 Phase Transitions in Silica at High Pressures and Temperatures

Silica, a framework silicate consisting of SiO$_4$ tetrahedra, is one of the most common building blocks of crystal Earth materials. Quartz, the stable form of SiO$_2$ at ambient conditions, is expected to undergo phase transitions at high pressures with an increased coordination number from four to six, where silicon is in the octahedral coordination environment similar to that in perovskite. Theoretical studies indicate that a large number of structurally related and thermodynamically stable phases of SiO$_2$ are possible at high pressures, and that many of these phases possess similar total energies (Karki et al. 1997a; Teter et al. 1998; Klug et al. 2001; Tsuchiya et al. 2004a; Oganov et al. 2005; Driver et al. 2010). However, only three of the high-pressure SiO$_2$ polymorphs were experimentally proven and/or found in natural lower-mantle conditions: tetragonal stishovite, orthorhombic CaCl$_2$-polymorph and α-PbO$_2$ polymorph (seifertite).

Stishovite, a post-coesite SiO_2 phase, stable at pressures above $\sim$7 GPa, was named after the Russian scientist Sergei Stishov who first discovered it in quenched samples from shocked silica in gas gun shockwave experiments (Stishov and Popova 1961). Later, it was discovered in nature in Meteor Crater, Arizona (Chao et al. 1962). Stishovite has a tetragonal rutile TiO_2 structure with a space group $P4_2/mnm$ (Stishov and Belov 1962). This structure consists of slightly distorted SiO_6 octahedra that share edges to form chains running parallel to the c axis (Fig. 4.28a). Each octahedron is corner linked to four neighbouring chains. The structure can also be described as a distorted hexagonal close-packed array of O^{2-} anions with half of the octahedral sites occupied (Wicks and Duffy 2016). Static high-pressure experiments established that stishovite is stable at pressures from 7–9 GPa to 43–70 GPa (Kingma et al. 1995, 1996; Zhang et al. 1996; Andrault et al. 1998b; Nomura et al. 2010).

Orthorhombic CaCl$_2$-structured silica. The possibility of a post-stishovite phase was extensively debated in the 1980–1990s (Park et al. 1988; Hemley et al.
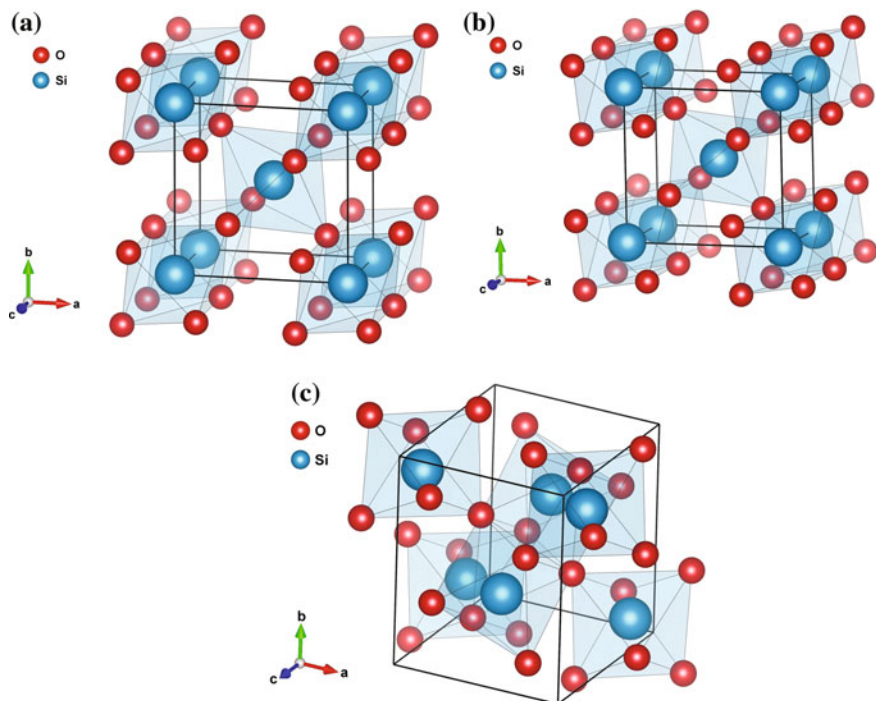
Fig. 4.28 Crystal structures of high-pressure SiO_2 polymorphs. **a** Stishovite with a tetragonal rutile TiO_2 structure (space group $P4_2/mnm$); **b** CaCl$_2$-type orthorhombic structure (space group $Pnnm$), oxygen escapes from the diagonal of the (a, b) plane, thus changing the symmetrical arrangement from tetragonal to orthorhombic; **c** Seifertite orthothombic structure (space group $Pbcn$). Lattice parameters from Yamanaka et al. (2002) for stishovite, from Andrault et al. (2003) for the CaCl$_2$-structured polymorph, and from Dera et al. (2002) for seifertite

1994 and references therein). Theoretical calculations predicted the transformation of the tetragonal structure into the orthorhombic CaCl$_2$ structure initially at a megabar pressure (Cohen 1987). Transition of stishovite into a CaCl$_2$ structure with the transformation of the tetragonal structure into orthorhombic (*Pnnm* space group; Fig. 4.28b) was first proven experimentally by Tsuchida and Yagi (1989). They observed it at a pressure of 108–124 GPa using a laser-heated DAC and powder XRD. The subsequent experiments using XRD and Raman spectroscopy (Kingma et al. 1995, 1996; Andrault et al. 1998b; Hemley et al. 2000) established the stishovite → CaCl$_2$-structured phase transformation at a much lower pressure of 43–54 GPa at room temperature; and theoretical calculations confirmed the same pressure range, at 47–55 GPa (Karki et al. 1997a; Teter et al. 1998). The orthorhombic CaCl$_2$ structure differs from the stishovitic one only by a small rotation of the octahedral chains (Fig. 4.28b).

The *P–T* phase boundary for the post-stishovite transition has been examined a number of times. Tsuchiya et al. (2004a) performed first-principles calculations and determined the stishovite-CaCl$_2$-structured phase transition boundary with a positive Clapeyron slope to be P (GPa) = 56.1 + 0.00585 × T (K), suggesting that the transition occurs at 1670 km depth along the normal mantle geotherm, where it may be responsible for the seismic heterogeneity. High *P–T* experiments in LHDAC equipment and in situ XRD observed that the phase transition occurred at 80 GPa at high temperature, corresponding to a depth of ∼1750 km along the typical mantle geotherm; the boundary was represented by a linear equation: P (GPa) = (51 ± 2) + (0.012 ± 0.005) × T (K) (Ono et al. 2002). Ono et al. concluded that the post-stishovite phase transition is not the cause of such heterogeneities in the mid-lower mantle. However, the boundary was not tightly constrained in their experiments. In other experiments, the transition occurs at 45–60 GPa under 500–1000 K and increases up to 75–90 GPa under 1500–3000 K with the boundary equation 11.1 MPa/K (Nomura et al. 2010). According to the Nomura et al. (2010) calculations, the transition and the accompanying seismic inhomogeneity should occur within the 1530–1830 km boundary, depending on the position of geotherm. The summary on the stishovite → CaCl$_2$-structured SiO$_2$ transition obtained from experimental data and theoretical calculations is presented in Table 4.13 and Fig. 4.29.

Concentration of aluminium in stishovite. According to experiments, stishovite may contain up to 5 wt% Al$_2$O$_3$ (Litasov et al. 2007). The concentration of aluminium in SiO$_2$ influences the position of the phase transition. The phase transition boundary of Al-bearing stishovite is lower than that of pure SiO$_2$ by ∼25 GPa: it is located at ∼62 GPa under 2000 K, which corresponds to ∼1500-km depth (Hirose et al. 2005) (Fig. 4.29).

Concentration of H$_2$O in stishovite is related to the Al admixture in silica. While Al-free stishovite contains only 16–30 wt ppm H$_2$O, synthetic stishovite with 4.4 wt% Al$_2$O$_3$ contains ∼3010 wt ppm H$_2$O (Litasov et al. 2007). Most hydrogen in stishovite is associated with Al^{3+} substitutional defects on the octahedral (Si^{4+}) site. Hydrogen can occupy 40% of vacancies created by incorporation of Al^{3+} at 20 GPa (Litasov et al. 2007). It is also possible that Al forms the AlOOH

Table 4.13 Summary on experimental and theoretical studies of stishovite-to-CaCl$_2$-structured SiO$_2$ transition

Authors	Experimental method[a]	Theoretical method[a]	Diffraction method[a]	Starting material; Al$_2$O$_3$, in SiO$_2$	P–T conditions of transfer
Tsuchida and Yagi (1989)	LHDAC		Powder in situ XRD	Quartz or amorphous SiO$_2$	108–124 GPa
Kingma et al. (1995)	DAC with neon medium		In situ Raman spectroscopy	Natural quartz	50 ± 3 GPa at room temperature
Kingma et al. (1996)	DAC without a medium		Synchrotron XRD	Quartz	43 GPa
Karki et al. (1997a)		Pseudopotential method within the LDA			47 GPa
Andrault et al. (1998b)			Angle-dispersive synchrotron XRD	Synthetic quartz	54 GPa at 300 K
Teter et al. (1998)		Fundamental crystal chemistry and first-principles total-energy calculations			55 GPa
Hemley et al. (2000)	DAC with hydrogen medium		Single-crystal synchrotron XRD		~50 GPa
Ono et al. (2002)	LHDAC		In situ XRD		80 GPa at 1900 km (mantle geotherm)
Tsuchiya et al. (2004a, b)		Density-functional linear response theory			58 GPa at 0 K and 72 Gpa at 2700 K
Hirose et al. (2005)	LHDAC		In situ angle-dispersive XRD	MORB glass or gel	62 Gpa and 2000 K
Lakshtanov et al. (2007)	DAC with neon medium		Synchrotron angle-dispersive XRD	5 wt% Al$_2$O$_3$	30 GPa
Nomura et al. (2010)	LHDAC		Angle-dispersive XRD	Powdered synthetic quartz	71 GPa at 2150 K (mantle geotherm)
Yamazaki et al. (2014)	Multi-anvil with SDA		Synchrotron XRD	Sintered at 12 GPa stishovite	62.3 GPa at 300 K
Umemoto et al. (2016)		DFT using the PBE-type GGA and molecular dynamics simulations		6.25 mol% AlOOH	30–50 GPa at 1000–1500 K

Notes: [a]*DAC* diamond-anvil cell; *DFT* density functional theory; *GGA* generalized gradient approximation; *LDA* local density approximation; *LHDAC* laser-heated diamond-anvil cell; *SDA* sintered diamond anvils; *XRD* X-ray diffraction

Fig. 4.29 Phase diagram for SiO$_2$ under high pressure and temperature conditions. Data from Ono et al. (2002), Murakami et al. (2003), Hirose et al. (2005), Shieh et al. (2005), Lakshtanov et al. (2007), Bolfan-Casanova et al. (2009), Driver et al. (2010), Nomura et al. (2010), Grocholski et al. (2013), Umemoto et al. (2016). Mantle adiabate after Katsura et al. (2010)
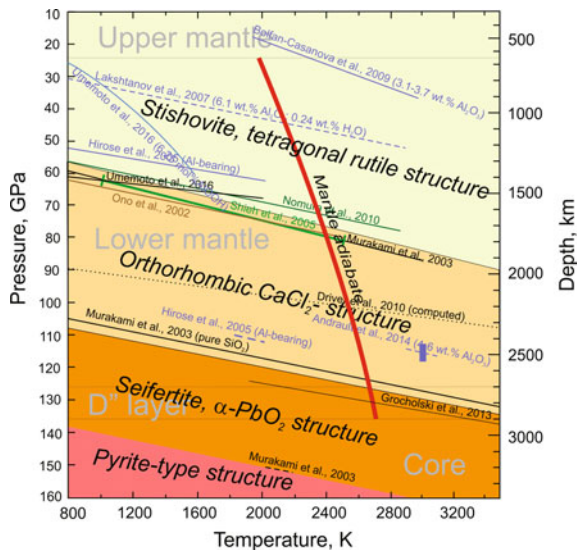
phase, which is highly soluble in stishovite (e.g., Chung and Kagi 2002; Panero and Stixrude 2004) (see Sect. 5.5.3). Lakshtanov et al. (2007) showed that the incorporation of water into Al-rich SiO$_2$ significantly reduces the post-stishovite transition pressure in SiO$_2$: in hydrous stishovite containing 5 wt% Al$_2$O$_3$ transformation occurs at 23–24 GPa (at 300 K) (Lakshtanov et al. 2007; Bolfan-Casanova et al. 2009), which is far lower than in pure silica. Umemoto et al. (2016), using first-principles static calculations and molecular dynamics simulations concluded that hydrogen bonds and hydrogen mobility play a crucial role in lowering the post-stishovite transition pressure. A cooperative redistribution of hydrogen atoms is the main mechanism responsible for the transition pressure reduction in hydrous Al-stishovite. Stishovite, containing 6.25 mol% AlOOH, transforms into CaCl$_2$-structured phase at pressures from 30–32 GPa (1000 K) to 50 GPa (1300 K) (Umemoto et al. 2016).

The CaCl$_2$-structured phase of SiO$_2$ is not observed in the natural environment to date.

Seifertite. In the lowermost mantle conditions, the pure CaCl$_2$-structured SiO$_2$ transforms into another orthorhombic α-PbO$_2$ ('skrutinyite')-structured polymorph named seifertite (El Goresy et al. 2008). In this phase, distorted SiO$_6$ octahedra are arranged into kinked chains extending along the c axis (Fig. 4.28c), resulting in a small density increase compared with stishovite and the CaCl$_2$-type phase (Wicks and Duffy 2016). This transition of CaCl$_2$-structured SiO$_2$ into an orthorhombic structure with space group $Pnc2$ was predicted to occur at ∼100–120 GPa using theoretical calculations (Belonoshko et al. 1996; Karki et al. 1997a). Later theoretical calculations by Teter et al. (1998), based on fundamental crystal chemistry and first-principles total-energy calculations, demonstrated that the space group of this phase should be $Pbcn$, which was confirmed in all further analyses (Sharp et al.

1999; Zhang et al. 2016a, b). The formation of α-PbO$_2$ phase was confirmed by experiments in laser-heated DAC by Dubrovinsky et al. (1997, 2001b, 2003), but at much lower pressures, 68–80 GPa and $\sim$1000–2000 K. These results were not confirmed by later experiments (possibly because of the wide range of metastability of seifertite). In all following experiments, the transformation of CaCl$_2$-structured SiO$_2$ into α-PbO$_2$ phase was observed within the range of 90–140 GPa along the mantle geotherm (Murakami et al. 2003; Shieh et al. 2005; Grocholski et al. 2013; Andrault et al. 2014; Zhang et al. 2016a, b). The boundary of the transformation has a positive Clapeyron slope and is represented by a linear equation P (GPa) = 98 + (0.0095 $\pm$ 0.0016) T (K) (Murakami et al. 2003) or P = 106.3 + 0.00579 T (K) (Tsuchiya et al. 2004a), which is almost parallel to the stishovite/CaCl$_2$ polymorph transformation. These data correspond to calculations with the use of DFT (Tsuchiya et al. 2004a, b; Oganov et al. 2005) and the QMC method (Driver et al. 2010), according to which the phase transition should occur at 90–120 GPa. The earlier experiments were performed without the pressure transmitting medium and thermal insulation in the diamond-anvil cell, which can result in severe deviatoric stresses and thermal gradients. In most recent experimental works, using insulating noble gas media in DAC and in situ XRD measurements, the formation of the *Pbcn*-structured α-PbO$_2$ phase was observed at the lowermost mantle conditions (113–140 GPa), most likely within the D$''$ layer (Grocholski et al. 2013; Andrault et al. 2014; Zhang et al. 2016a, b). The summary on theoretical calculations and experimental data on the formation of seifertite is presented in Table 4.14 and Fig. 4.29.

The space group of the seifertite orthorhombic structure has been under debate due to its similarity to several other space groups in the orthorhombic system. When the phase was first experimentally reported in DAC experiments at pressures of between 68 and 85 GPa and temperatures above $\sim$2000 K (Dubrovinsky et al. 1997, 2003), the few peaks observed in the powder XRD pattern did not allow for an unambiguous structure determination, such that the theoretically predicted space group *Pnc*2 using the molecular dynamics theory was used to explain the diffraction patterns (Belonoshko et al. 1996). To date, however, an unambiguous structure determination of seifertite with the space group *Pbcn* within its stability field is established with a single-crystal XRD (Zhang et al. 2016a, b), which is in agreement with predicted first-principle calculations (Karki et al. 1997a; Teter et al. 1998) and found in meteorites (Dera et al. 2002; El Goresy et al. 2008) (Fig. 4.29).

Seifertite is remarkable in that it can be metastably preserved to 1 bar from 140 GPa after high temperature quenching, instead of converting back to its lower-pressure forms, such as quartz, stishovite or densified glass. The greater molar volume of seifertite found in early experiments supports a metastable synthesis of the phase outside of its stability field (Grocholski et al. 2013). However, to date no seifertite grains were identified in lower-mantle diamonds, even though several grains of silica polymorphs have been studied using synchrotron XRD. This implies that the transformation of CaCl$_2$-structured SiO$_2$ into α-PbO$_2$-structured seifertite takes place deeper than the lower mantle boundary, or that seifertite inclusions are still yet to be found in diamond.

Table 4.14 Summary on theoretical and experimental studies of seifertite

Authors	Theoretical method[a]	Experimental method[a]	Diffraction method[a]	Natural sample	Starting material; Al_2O_3, in SiO_2	P–T conditions of transfer	Space group of seifertite
Belonoshko et al. (1996)	Molecular dynamics					Above ∼ 120 GPa in a wide range of T	$Pnc2$ (intermediate between $Pbcn$ and $P2_1/c$)
Karki et al. (1997a)	Pseudopotential method within the LDA					98 GPa	$Pnc2$
Dubrovinsky et al. (1997)		LHDAC	XRD		Silica gel and quartz	68 ± 5 GPa at 2000 ± 50 K	$Pnc2$ (based on theoretical considerations)
Dubrovinsky et al. (2001b)		Electrically and laser heated DAC	In situ XRD		α-crystobalite	45–53 GPa and >80 GPa at high T	$Pnc2$
Dubrovinsky et al. (2003)		Electrically heated DAC			Silica gel 99.99% purity	75–80 GPa at 950 K	
Teter et al. (1998)	Fundamental crystal chemistry and first-principles total-energy calculations						$Pbcn$
Sharp et al. (1999)			Single-crystal selected-area electron diffraction	Martian meteorite Shergotty	Al_2O_3 = 1.12 wt %; Na_2O = 0.4 wt %		$Pbcn$
El Goresy et al. (2000)			XRD	Martian meteorite Shergotty			Mixture of phases $Pbcn$ and $P2_1/c$
Dera et al. (2002)			Powder XRD	Martian meteorite Shergotty	Al_2O_3 = 0.8–1.6 wt%; Na_2O = 0.2–0.5 wt%		$Pbcn$

(continued)

Table 4.14 (continued)

Authors	Theoretical method[a]	Experimental method[a]	Diffraction method[a]	Natural sample	Starting material; Al_2O_3 in SiO_2	P–T conditions of transfer	Space group of seifertite
Murakami et al. (2003)		LHDAC without a medium	In situ synchrotron XRD		Synthetic amorphous pure SiO_2	121 GPa at 2400 K	
Tsuchiya et al. (2004a, b)	DFT					∼120 GPa	
Oganov et al. (2005)	Density-functional perturbation theory					∼90 GPa	
Shieh et al. (2005)		LHDAC	In situ angle-dispersive XRD		Pure silica glass and stishovite	113–117 GPa at 2160–2320 K and 124–128 GPa at 2250–2500 K	
El Goresy et al. (2008)			Selected-area electron diffraction	Martian meteorites Shergotty and Zagami	Al_2O_3 = 0.8–1.6 wt%; Na_2O = 0.2–0.5 wt%	Shock event with $P > 35$ GPa	Pbcn or Pb2n
Driver et al. (2010)	Quantum Monte Carlo method				Pure SiO_2	86–122 GPa at 2300–2600 K	
Miyahara et al. (2013)			XRD	Lunar meteorite NWA4734	Na_2O = 0.59–0.89 wt%; Na_2O = 0.21–0.26 wt%	Dynamic event	Pbcn
Grocholski et al. (2013)		LHDAC with insulating noble gas medium	In situ XRD		Pure (99.8%) or 10-mol% Al_2O_3 amorphous SiO_2	130–140 GPa at 2500 K	
Andrault et al. (2014)		LHDAC	Synchrotron in situ XRD		Na_2O = 4–6 wt%	113–119 GPa at 2500 K	
Zhang et al. (2016a, b)		LHDAC with neon medium	Single-crystal XRD		$(Mg_{0.6}Fe_{0.4})SiO_3$ + 5% SiO_2	129 GPa at 2500 K	Pbcn

Notes: [a]*DAC* diamond-anvil cell; *DFT* density functional theory; *LDA* local density approximation; *LHDAC* laser-heated diamond-anvil cell; *XRD* X-ray diffraction

On the surface of the Earth, seifertite was identified in Martian shergottites Sherotty, Zagami and NWA 4734 (Sharp et al. 1999) and the Lunar Asuka 881757 meteorite (Miyahara et al. 2013). Martian seifertite has the same (as in experiments) orthorhombic *Pbcn* structure (Dera et al. 2002; El Goresy et al. 2008) and minor admixtures of Na$_2$O (0.2–0.5 wt%) and Al$_2$O$_3$ (0.8–1.6 wt%). The formation of seifertite in meteorites is explained by shock events under dynamic pressures of 35–80 GPa (El Goresey et al. 2008; Miyahara et al. 2013). A disagreement between these estimates and much higher pressures of origin of seifertite under static conditions may be due to the extreme metastability of seifertite (Grocholski et al. 2013).

High alumina content in CaCl$_2$-structured SiO$_2$ has the same effect as in stishovite: according to experimental data, Al lowers the transition of CaCl$_2$-structured SiO$_2$ into seifertite by 5–10 GPa compared with pure silica: to 113–119 GPa at 2500 K (Hirose et al. 2005; Andrault et al. 2014).

However, the naturally occurring stishovite and seifertite contain only a small amount of Al admixture; for example, there is well below 1% in stishovite in lower-mantle diamond inclusions (Wirth et al. 2007), and 0.8–1.6 wt% Al$_2$O$_3$ in seifertite in Martian meteorite (El Goresy et al. 2000, 2008). Therefore, these silica polymorphs in nature are expected to have a chemical composition very close to pure SiO$_2$; and the Al$_2$O$_3$ dissolution is not expected to significantly affect the phase transition boundary.

Seifertite is stable up to 150–260 GPa; at such pressure, seifertite should obtain a **pyrite-type structure** (Karki et al. 1997a; Murakami et al. 2003; Kuwayama et al. 2005).

4.6.3 Physical Properties

The presence of free silica in the deep mantle was suggested to cause seismic velocity anomalies that are faster, by a few percent, relative to surrounding ultramafic peridotite assemblages (Bina 2010 and references therein).

The stishovite → CaCl$_2$ polymorph transition is a second-order ferroelastic transition, in the terminology of Wadhawan (1982), like in CaSi-perovskite (see Sect. 4.5.3). It consists of an orthorhombic distortion of tetragonal stishovite and displays large shear modulus softening (Cohen 1991; Karki et al. 1997a; Carpenter et al. 2000; Tsuchiya et al. 2004a, b; Jiang et al. 2009; Asahara et al. 2013). As a result, even a small fraction of free silica may produce a detectable seismic signal in the mid-lower mantle (Karki et al. 1997a).

Theoretical calculations of the volume change during the stishovite → CaCl$_2$ polymorph transition are controversial. A single Birch-Murnaghan equation of state suggested that the phase transition occurs without a substantial change in volume (Andrault et al. 1998b), while the pseudopotential method within the local-density approximation showed that the phase transition is associated with a volume decrease (Karki et al. 1997a), and the shear wave velocity V_s decreases rapidly (by

60%) between 40 and 47 GPa prior to the transition from stishovite to the $CaCl_2$ structure at 47 GPa (Karki et al. 1997b). Further experiments proved that the volume of the $CaCl_2$ phase is smaller than that in stishovite across the phase transition, and $CaCl_2$ polymorph is a significantly denser than stishovite in the high-pressure range (Andrault et al. 2003). Carpenter et al. (2000) established that seismic wave velocities, especially S-wave speed, are significantly reduced near this phase transition: S-wave velocity drops by $\sim 25\%$ at the phase transition and by 12–15% 100 km above and below the phase transition, i.e., the transition occupies the interval of ~ 200 km (Carpenter et al. 2000; Komabayashi et al. 2007). This seismic effect may be expected at the 1600–1800 km depth (see Fig. 4.29).

The $CaCl_2$ phase $\rightarrow$ seifertite (α-PbO_2) structural transition in SiO_2 (*Pnnm* $\leftrightarrow$ *Pbcn*), like the stishovite $\rightarrow$ $CaCl_2$ phase transition (*P4$_2$/ mnm* $\leftrightarrow$ *Pnnm*), is also of the ferroelastic type. Seifertite within its stability field is 1.5% denser than $CaCl_2$-structured SiO_2 (Grocholski et al. 2013) and approximately 10% lower density and 10% larger bulk sound velocity than the surrounding lowermost mantle (Tsuchiya et al. 2004a). The transformation of the $CaCl_2$ phase to seifertite is accompanied by a discontinuous change of 1–2% in elastic wave velocity and a decrease by a factor of two in anisotropy. Even a small amount of silica in the lower mantle may contribute significantly to observed seismic anisotropy (Karki et al. 1997b).

4.6.4 Origin of Silica Polymorphs in the Lower-Mantle Ultramafic Association

Stishovite SiO_2 and periclase–wüstite solid solutions $(MgO–FeO)_{ss}$, associate paradoxically in primary inclusions of lower-mantle diamonds. Under the conditions of the Earth's crust and upper mantle, such oxide assemblages are chemically impossible (forbidden) because the oxides MgO and FeO and SiO_2 react to produce intermediate silicate compounds, enstatite and ferrosilite. However, in the lower mantle silica is permanently present in association with bridgmanite and ferropericlase. Such occurrence in the lower-mantle associations was refered to as a 'stishovite paradox' (Litvin 2014; Litvin et al. 2016) and is not yet fully understood.

Initially, a model of the decomposition of bridgmanite with the resultant formation of ferropericlase and stishovite has been proposed:

$$(Mg, Fe)SiO_3 \rightarrow (Fe, Mg)O + SiO_2.$$

$$Fe-bridgmanite \rightarrow Ferropericlase + Stishovite$$
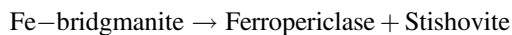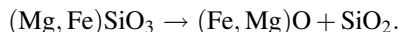
Such a transformation has been experimentally simulated, but only for Fe-rich systems, at 17–23 GPa (Ito and Takahashi 1989; Fei et al. 1996; Akaogi 2007). Ito and Takahashi (1989) estimated the limiting composition for bridgmanite in equilibrium with SiO_2 and ferropericlase as having $mg = 0.89$ and the composition

of the co-existing ferropericlase at $mg = 0.42$. However, the compositions of known ferropericlase associated with SiO$_2$ in a natural environment are more magnesium-rich: $mg = 0.70$ in Sao Luiz, Brazil (sample #BZ-103a; Harte et al. 1999) and $mg = 0.86$ in Kankan, Guinea (sample KK-31a; Stachel et al. 2000).

An explanation of formation of free silica as the result of decomposition of post-perovskite within the D″ layer was offered by Knittle and Jeanloz (1991). According to this model, post-perovskite (Mg,Fe)SiO$_3$ reacts with molten iron at the core–mantle boundary (within the D″ layer). As a result of this reaction, metallic alloys, FeO, FeSi and free silica may occur:

$$(Mg, Fe)SiO_3 + Fe \rightarrow MgSiO_3 + SiO_2 + FeO + FeSi.$$

Another model of the formation of SiO$_2$ in the ultramafic association (based on the fractional crystallization of the lower-mantle material) was proposed by Litvin (Litvin 2014; Litvin et al. 2016). According to this model, high iron content in the lower mantle may occur as a result of the crystallization of ferropericlase-magnesiowüstite accompanied by the increase of its fe index. During the course of fractional crystallization in ultramafic magma within the lower mantle, permanent fractionation with the removal of newly formed minerals results in the progressive evolution of the total composition of the system. The total composition is successively consistent with the changing compositions of residual melts. Fractional crystallization of ferropericlase-magnesiowüstite with decreasing temperature should be accompanied by an increase in the concentration of the relatively low-temperature component of the solid solution (in our case, FeO) in residual melts. The FeO concentration in residual melts is critical for initialization of the reaction   Bridg + Liq = Sti + MgWus   in   peritectic   Liq + MgWus + Bridg + CaSiPrv + Sti. This may explain the 'stishovite paradox', since stishovite appears in the peritectic composition. After the disappearance of bridgmanite, as an individual phase, the figurative point of the melt migrates along the monovariant curve Liq + MgWus + CaSiPrv + Sti, which is accompanied by an increase of fe in ferropericlase-magnesiowüstite associated with stishovite. This model is in fact another variety of the bridgmanite decomposition mechanism.

All these models are based on the assumptions from a pyrolitic composition of the lower mantle, analogous to the upper mantle composition. However, the enrichment of the lower mantle, particularly its lowermost part in Si may be caused by its chemical stratification, layering and very limited mass transport between the lower and the upper mantle. In geological samples from all areas free silica is always present, and this may be considered to be evidence of the enrichment of the juvenile lower mantle in SiO$_2$. The initial enrichment of the lower mantle with Si was suggested by Kaminsky (2012) during a study of natural parageneses in the lower mantle. This model was confirmed by the distribution of sound velocities in the lower mantle, which fit its enrichment in Si compared with the upper mantle (Murakami et al. 2012) and may be caused by the presence of free silica in the lower mantle (Bina 2010). Such interpretation is consistent with earlier proposals from

both geochemical and isotopic studies and seismic data (e.g., Anderson 2002; Cammarano and Romanowicz 2007; Matas et al. 2007; Ricolleau et al. 2008). It has been suggested that the source of silica in the lower mantle may be the Earth's core, which originally included $\sim$6 wt% SiO_2 but then became depleated in silicon by crystallizing SiO_2 and $MgSiO_3$ (Ozawa et al. 2016).

This model is also confirmed by planetary geochemical evidence. If the Earth was accreted from material such as the CI chondrites, which have the Mg/Si ratio of approximately 1.074, the lower mantle should be chemically distinct from the upper mantle (Javoy 1995; Williams and Knittle 2005), which has the Mg/Si ratio close to 1.27 (Ringwood 1975; Anderson 1983), i.e. lower mantle should be enriched in Si. In addition, the CI-chondrite model of the Earth's composition has been challenged, and the enstatite-chondrite model has been proposed (Javoy et al. 2010; Kaminski and Javoy 2013, 2015). Enstatite chondrite is significantly richer in silica than CI chondrites (Mg/Si = 0.69) and contains free silica in its composition (Javoy et al. 2010). The normative mineralogy of the lower mantle, calculated on the enstatite chondrite compositions, contains free silica ranging from 5% for low-iron (EL) enstatite chondrite to 12% for high-iron (EH) enstatite chondrite compositions (Frost and Myhill 2016).

Thermodynamic modeling with the use of HeFESTo code, based on experimental data and performed for the $MgSiO_3$–$FeSiO_3$ (enstatite–ferrosilite) compositions at lower-mantle pressures and $\sim$2000 K by Dorfman et al. 2013 demonstrated that within a wide compositional range ($fe = 0.1$–1), SiO_2 is stable in association with bridgmanite: initially in the form of stishovite (from 24 to $\sim$50 GPa), then as the $CaCl_2$-structured phase. This confirms that SiO_2 may occur in the ultramafic lower mantle without fractional crystallization and may be in equilibria with other lower-mantle phases.

In such a case, no special scenario of SiO_2 origin in the lower mantle is needed; *free silica should be considered as one of the major initial mineral components of the lower mantle*.

4.7   Mg–Cr–Fe, Ca–Cr and Other Orthorhombic Oxides

4.7.1   General

In one of the diamond grains from the Juina area, Brazil, a microxenolith of a supposed lower-mantle rock was found (Kaminsky et al. 2015a). It was composed of iron carbide, ferropericlase and two orthorhombic oxides $Mg(Cr,Fe)_2O_4$ and $CaCr_2O_4$, which are new mineral phases. This association was formed during several stages and it is considered as a rock microfragment of the lower mantle. In addition to the carbide-oxide fragment, some other phases were identified as inclusions in that diamond, such as orthorhombic MgO and an assemblage of periclase plus wüstite, among others.

Another series of lower-mantle orthorhombic oxides were recently identified as an inclusion in diamond, in association with nitride Fe_3N, and are suggested to originate within the lowermost mantle (Kaminsky and Wirth 2017).

4.7.2 Chemical Compositions

An elemental map of the carbide-orthorhombic oxides assemblage, using X-ray fluorescence intensities of the C–K_α, O–K_α, Mg–K_α, Ca–K_α, Cr–K_α and Fe–K_α, illustrates different element distributions in these mineral phases within the lower-mantle microxenolith (Fig. 4.30). The chemical compositions of the minerals, calculated from the EDX spectra, are presented in Table 4.15. In addition to major elements, EDX spectra demonstrate the presence of minor admixtures: Mg, Al, Ti, V, and Fe in Ca–Cr oxide; Al and V in Mg–Cr–Fe oxide; unusually high Mn (5.52 at.%) and Cr in ferropericlase.

Based on this analysis, an empirical formula for the new Mg-bearing oxide can be derived as $(Mg_{0.90}Mn_{0.18})_{1.08}(Cr_{1.37}Fe^{3+}{}_{0.39}V_{0.11}Al_{0.05})_{1.92}O_4$ or simplified as $Mg(Cr,Fe)_2O_4$. This formula is isomorphic to magnesium chrome spinel from kimberlites (e.g., Barnes and Roeder 2001) and is similar to xieite from the Suizhou meteorite (Chen et al. 2003b, 2008) with Mg instead of divalent Fe in its composition. The derived formula for Ca-bearing oxide is $(Ca_{1.07}Mg_{0.02}Mn_{0.02})_{1.11}(Cr_{1.71}Fe^{3+}{}_{0.06}V_{0.06}Ti_{0.03}Al_{0.03})_{1.89}O_4$ or simplified as $CaCr_2O_4$ calcium chrome spinel. In addition to the Cr, Al, Mg and Fe substitution in natural chromite, the orthorhombic phases are likely to incorporate Ca, Ti, Fe, Na, Si (as in $CaFe_2O_4$, $CaTi_2O_4$ and $NaAlSiO_4$), and possibly other divalent and trivalent transition elements and rare earth elements, thus having a major effect on element partitioning of the deep-Earth geochemistry (Chen et al. 2003a, b).
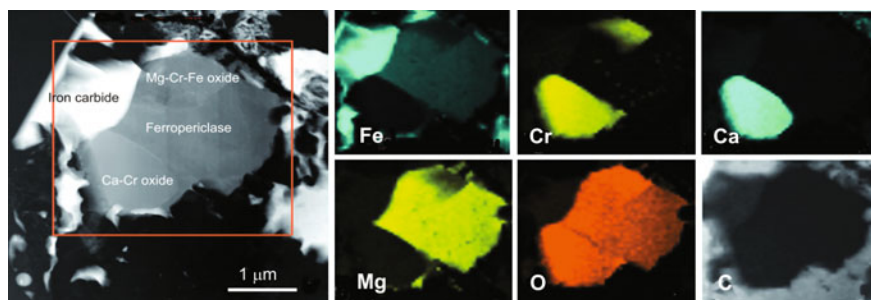
Fig. 4.30 Polyphase mineral inclusion in diamond from the Juina area, Brazil. General view (*left image*): an assemblage of major mineral phases forming an allotriomorphic texture and surrounded by graphite in the inclusion; *Right panels* elemental maps for Fe, Cr, Ca, Mg, O and C of the polyphase inclusion. From Kaminsky et al. (2015a). Used with a permission of the Canadian Mineralogist

Table 4.15 Chemical compositions of oxides (at.%)

Elements	From lower-mantle microxenolith			From association with iron nitride Fe_3N	
	Ferropericlase	Orthorhombic Mg–Cr–Fe oxide	Orthorhombic Ca–Cr oxide	Orthorhombic Mn–Fe–Cr oxides	
Mg	63.08	30.09	0.79	–	–
Ca	–	–	35.72	–	–
Cr	0.30	45.78	57.02	23.07	56.17
Fe	31.10	12.92	1.93	28.09	13.31
Mn	5.52	6.08	0.69	46.05	25.29
Al	–	1.58	0.80	–	–
Ti	–	–	1.09	–	–
V	–	3.55	1.96	1.31	3.38
Si	–	–	–	1.48	1.85
Total	100.00	100.00	100.00	100.00	100.00
mg = Mg/ $(Fe + Mg)_{at.}$	0.670	0.700	0.290	0	0

Fig. 4.31 A grain of iron nitride, Fe_3N, intergrown with orthorhombic oxides from an inclusion in a diamond from Rio Soriso, Juina area, Brazil. TEM dark field image. Photo made by R. Wirth. After Kaminsky and Wirth (2017)
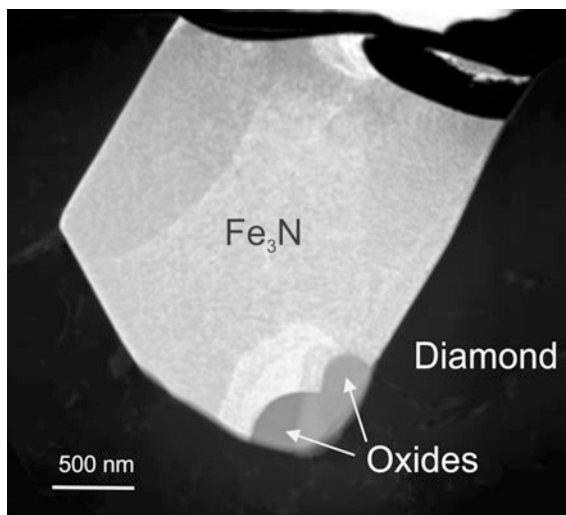
Two orthorhombic oxides identified in association with iron nitride Fe_3N (Fig. 4.31) are characterized by the absence of Mg and high concentrations of MnO = 25.29–46.05 at.% (Table 4.15). Their occurrences indicate great variability of post-spinel oxides in the lower mantle.

4.7.3   Crystal Structures of the Orthorhombic Oxides and Their Stability Range

Reid and Ringwood (1969, 1970) proposed two orthorhombic structures of $CaFe_2O_4$-type (CF) and $CaTi_2O_4$-type (CT) structures, which are denser than spinel, as being top candidates for post-spinel phases in the Earth's lower mantle. Both CF and CT structures contain dodecahedral and octahedral sites. The difference between these structures lies only in slight modifications of the linkage to the SiO_6 polyhedra (Fig. 4.32). The new $Mg(Cr,Fe)_2O_4$ oxide has an orthorhombic CT structure with lattice parameters (in Å): $a = 10.654$; $b = 9.401$; $c = 2.905$.

 CaCr_2O_4 oxide also has an orthorhombic structure, with lattice parameters (in Å): $a = 10.170$; $b = 9.017$; $c = 2.874$ (Kaminsky et al. 2015a). Its d-spacings and angles between lattice planes do not fit exactly to either a CT or a CF structure. It is most likely to be the high-temperature CF (β) variety (Lee and Nassaralla 1997) (Fig. 4.33a, b); however, the CT structure should not be excluded (Fig. 4.33c). Although $CaCr_2O_4$ is one of the important components of materials for many high-temperature applications in metallurgy, ceramics and solid oxide fuel cells (Róg et al. 2007; Zhai et al. 2016), there are no natural analogues for this oxide to date.

 Experimental investigations have demonstrated spinel-structured $CaAl_2O_4$ and $MgAl_2O_4$ transformations into a CF structure at pressures above 26.5 GPa at the top of the lower mantle conditions (Akaogi et al. 1999) and the $MgAl_2O_4$ structure transformations into a CT structure at pressures in excess of 40 GPa in the mid-lower mantle conditions (Funamori et al. 1998; Chen et al. 2003a and references therein). The only natural orthorhombic post-spinel polymorph of chromite with a CF structure, with an ideal formula of $FeCr_2O_4$, was discovered in shock veins of the
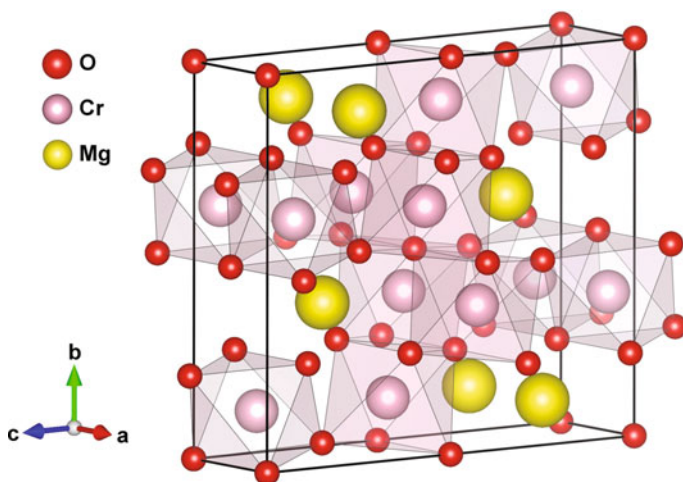
Fig. 4.32 Orthorhombic CT crystal structure (space group *Cmcm*) of the $Mg(Cr,Fe)_2O_4$ oxide. Lattice parameters from Yamanaka et al. (2008)
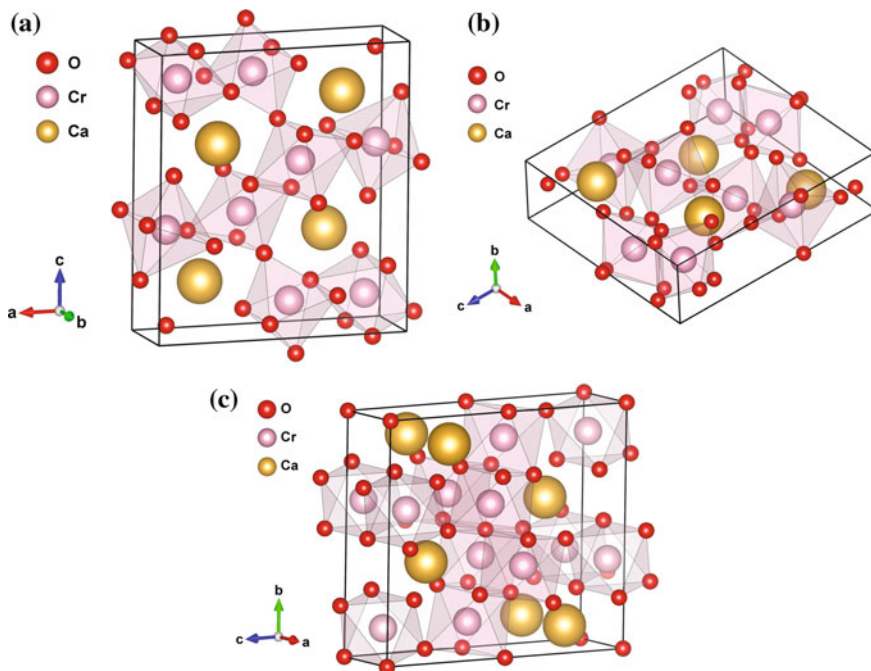
Fig. 4.33 Possible structures of the $CaCr_2O_4$ oxide. *Left* **a** and *center* **b** Orthorhombic CF structure (space group *Pnma*) in differently oriented axes; *Right* **c** Orthorhombic CT structure (space group *Cmcm*). Lattice parameters from Yamanaka et al. (2008)

Suizhou meteorite and termed xieite (Chen et al. 2003b, 2008). Ishii et al. (2014) suggested that xieite does not belong to the CF-type but exhibits a modified CF-type structure. On the other hand, the CT structure is considered to be the most probable post-spinel structure for the lower mantle. Minerals with such a structure have been shown to coexist under the *P–T* conditions of the lower mantle (Yamanaka et al. 2008). The existence of such post-spinel phases suggests that the pressure conditions for their formation are at ≥ 40 GPa or approximately at a depth of ≥ 1000 km.

4.7.4 Other Inclusions with the Spinel Composition

Mineral grains with the general composition of chromian spinel $(Mg,Fe)(Cr,Al, Fe)_2O_4$, in association with ferropericlase and MgSi-perovskite, were identified in diamonds from the Pandrea pipes and placer deposits in Juina, Brazil (Kaminsky et al. 2001, 2009a). Their compositions vary significantly and are quite different from the chrome spinel inclusions in lithospheric diamonds (Table 4.16 and Fig. 4.34). It is possible that these inclusions with various compositions may have an orthorhombic structure (CF or CT) stable within the mid-lower mantle.

MREE and HREE abundances in these grains are close to chondritic, and the REE patterns are characterized by LREE-depletion (Fig. 4.35).

Table 4.16 Representative analyses of inclusions in diamond with chemical compositions of spinels (wt%)

Mineral	'Chromite'			'Al-spinel'	'Magnetite'	
Country	Brazil			Canada	Brazil	
Area	Juina			NW Territories	Juina	
Location	Pandrea-2 pipe		Corrigo Chicoria placer	Panda (Ekati)	Rio Soriso placer	Juina-5 pipe
Sample No.	P2-2	P2-17	Juina 5-17b	PA-54a	1-4K	Ju5-102
Assemblage	2Chr + MgCaSi-prv	2Chr + fPer + nativeFe	2Chr + 2fPer	Spl + fPer + 'Ol'	Mag	Mag + Brd + Jeffbenite + Ilm + Ttn + FeMgSi
SiO_2	0.14	0.04	0.57	0.40	0.16	0.30
TiO_2	0.58	0.12	10.73	0.10	2.36	15.79
Al_2O_3	19.75	15.1	5.37	57.42	4.75	9.96
Cr_2O_3	46.73	55.08	36.34	8.47	n.a.	0.11
V_2O_3	0.22	0.18	n.a.	n.a.	58.21	n.a.
FeO	22.29	16.73	33.53	9.10	30.80	64.81
MnO	0.77	0.49	0.79	0.07	0.58	0.40
NiO	0.03	0.01	n.a.	0.23	n.a.	n.a.
MgO	9.2	12.46	10.72	23.77	1.46	2.63
CaO	0.01	0.00	n.a.	0.00	0.15	0.02
ZnO	0.46	0.07	n.a.	n.a.	n.a.	n.a.
Na_2O	0.04	0.01	n.a.	0.00	n.a.	0.03
K_2O	0.01	0.oo	n.a.	0.00	n.a.	0.00
Total	100.23	100.29	98.05	99.56	98.47	94.04
fe	0.576	0.429	0.637	0.177	0.922	0.932
mg	0.424	0.571	0.363	0.823	0.078	0.068
cr#	0.613	0.710	0.819	0.090	0.000	0.007
References	Kaminsky et al. (2009b)		Kaminsky et al. (2001)	Tappert et al. (2009a)	Hayman et al. (2005)	Thomson et al. (2014)
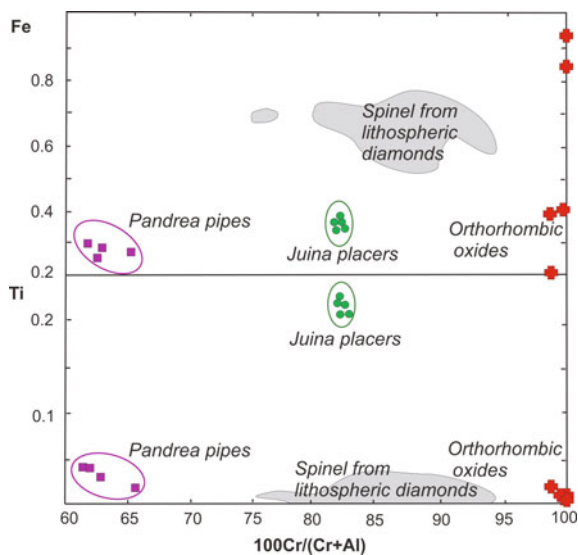
Fig. 4.34 Fe and Ti (cations) versus Cr/(Cr + Al)$_{at.}$ in inclusions with spinel compositions. Modified after Kaminsky (2012) with additions
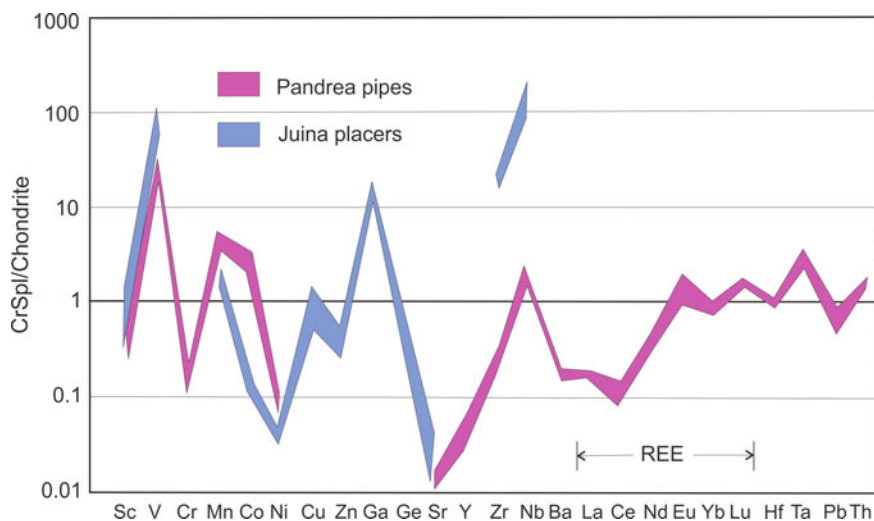
Fig. 4.35 Trace element patterns in inclusions with chromian spinel compositions. Data from Kaminsky et al. (2001, 2009a). Chondrite composition was derived from McDonough and Sun (1995). After Kaminsky (2012)

Other than the grains with the general chrome spinel composition, grains with alumospinel with $mg = 0.76–0.82$ have been identified in diamond from the Panda, Canada and Collier-4, Brazil kimberlite pipes (Tappert et al. 2005a; Bulanova et al. 2010). In addition, grains with the composition of magnetite were also identified in

diamonds from the Rio Soriso placer and the Juina-5 kimberlite pipe in Brazil, accompanied (in the latter place) by bridgmanite, jeffbenite, ilmenite and titanite (Thomson et al. 2014). Other than Fe cation substitution, major cations in these minerals are Si (0.16–0.28 wt% SiO_2), Ti (1.50–3.61 wt% TiO_2), Al (3.44–6.92 wt% Al_2O_3), Cr (2.10–3.03 wt% Cr_2O_3), Mg (1.46–3.58 wt% MgO), and Na (0–0.11 wt% Na_2O). Some of them with TiO_2 up to ∼16 wt% (Thomson et al. 2014) may be attributed as titanomagnetite.

4.8   Jeffbenite

4.8.1   General

Jeffbenite $(Mg,Fe^{2+},Ca)_3(Al,Fe^{3+},Cr)_2(Si,Ti)_3O_{12}$ (IMA No. 2014-097; Nestola et al. 2015, 2016b), a tetragonal almandine-pyrope phase formerly known as TAPP, was not expected to exist in the lower-mantle conditions with peridotite, pyrolite or MORB compositions (e.g., Irifune et al. 2010). It was discovered as small inclusions of 30–100 μm in diameter in diamonds from the São Luiz placer deposit in the Juina area, Brazil (Harte and Harris 1994; Harris et al. 1997; Harte et al. 1999; Zedgenizov et al. 2014a). Subsequently, it was identified in diamonds from other placers and kimberlite pipes of the same area and in Guinea placer, Kankan, and was suggested as a primary mineral phase in the upper-mantle and the lower parts of the transition zone (Kaminsky et al. 2001, 2009a, b; Hayman et al. 2005; Bulanova et al. 2010). Jeffbenite occurs as cubo-octahedral or elongate-tabular, apple-green grains with a stoichiometric composition similar to pyrope-almandine garnet. Some grains exhibit inclusions of ilmenite and ilmenite + spinel, which are possibly retrograde (Zedgenizov et al. 2014a).

As of yet, jeffbenite has not been synthesized experimentally in ultramafic systems at high *P*–*T* conditions since it appeared unstable in LHDAC experiments at pressures higher than 10–13 GPa and temperatures of 1300–1700 K (Armstrong and Walter 2012). Some researchers have suggested that the origin of jeffbenite is related to a retrograde process during the ascent of magmatic materials to the Earth's surface (Finger and Conrad 2000; Brenker et al. 2002; Armstrong and Walter 2012). An alternative hypothesis for its origin is that jeffbenite is a reaction product of majorite in the lower mantle (Harte 2010; Harte and Hudson 2013). Prior to the observation of the occurrence of an aluminous phase in the lower mantle, all Al was thought to reside in bridgmanite (Irifune 1994; Kesson et al. 1995), such that jeffbenite was thought to be the only aluminous phase to occur in a juvenile lower-mantle ultramafic association. Based on the association of jeffbenite with typical lower-mantle mineral phases, such as bridgmanite, ferropericlase and others (Harte and Harris 1994; Harris et al. 1997; Harte et al. 1999; Hutchison et al. 2001; Hayman et al. 2005; Kaminsky et al. 2001; Zedgenizov et al. 2014a), here we have grouped jeffbenite as a lower-mantle phase.

4.8.2 Chemical Composition

Chemical compositions of jeffbenite are presented in Table 4.17. Based on the compositional analysis, jeffbenite lacks evidence for majoritic solid solution and is very low in Ca (usually 0.03–0.54 wt% CaO; one sample from Guinea has 11.72 wt% CaO, partly replacing MgO (see Table 4.17), sample KK-108a), as compared with upper-mantle peridotitic or eclogitic garnets. The increasing admixture of Ti (up to 7.55 wt% TiO_2) is accompanied by decreasing the Si content, demonstrating the isomorphism between these elements. Ti-free jeffbenite is believed to form single-phase inclusions under relatively higher pressure conditions (Anzolini et al. 2016b), but it is not confirmed by geological data, according to which Ti-free jeffbenite occurs in association with bridgmanite and NaAl-silicate (Hutchison 1997; Table 4.17, sample BZ259A2).

Jeffbenite has very variable iron, magnesium and aluminium contents (FeO = 4.43–23.39 wt%; MgO = 12.86–37.01 wt%; Al_2O_3 = 7.79–24.17 wt%) and iron and magnesium indices (fe = 0.084–0.453; mg = 0.547–0.916). Ferric iron is the abundant form of iron ions: Fe^{3+}/Fe_{tot} = 66–74% (McCammon et al. 1997). The distribution of fe in jeffbenite is bimodal; two groups of samples can be distinguished by this parameter: low-Fe (fe = 0.084–0.217) and high-Fe (fe = 0.365–0.453) (Fig. 4.36a). These two groups of jeffbenite have different geochemical characteristics. The low-Fe group of jeffbenite (fe = 0.084–0.217) has high Al (15.60–24.17 wt% Al_2O_3) and elevated concentrations of Cr (1.33–3.00 wt% Cr_2O_3), while the second high-Fe group (fe = 0.365–0.453) usually has low Al (7.79 vs. 19.92 wt% Al_2O_3) and low Cr content (0.02–0.06 wt% Cr_2O_3) (Fig. 4.36b). The first group with the low Fe content is associated with typical lower-mantle minerals such as bridgmanite and ferropericlase, suggestive of jeffbenite being a primary lower-mantle mineral phase. The second group with the high Fe content is associated with garnet, spinel, magnesite and perhaps orthopyroxene, most likely originating in the transition zone or of the retrograde process.

Jeffbenite also contains minor amounts of Ni (0.01–0.07 wt% NiO), Mn (0.14–0.96 wt% MnO), Ca (0.01–0.13 wt%; in one sample 11.72 wt% CaO); Na (0.02–1.13 wt% Na_2O) and K (0–0.02 wt% K_2O). Concentrations of REE trace elements in jeffbenite, apart from Nb, Zr, and Hf, are less than those in chondrites; the trends of the REE patterns are, however, similar to chondritic (Fig. 4.37).

4.8.3 Crystal Structure

Jeffbenite was first examined to display a tetragonal crystal structure with a space group I-42d (a = 6.526 Å and c = 18.182 Å) and a chemical formula $^{VIII-IV}$(Mg, Fe^{3+})^{II}(Al,Cr,Mn)$_2$^{II}(Mg,Fe^{2+})$_2$Si$_3$O$_{12}$, where the first cation group occupies a tetrahedral coordination with a four-fold symmetry and the second and the third groups have an octahedral coordination with a two-fold symmetry (Harris et al. 1997). Strictly speaking, the tetrahedral site is a distorted eight-fold 'capped'

Table 4.17 Representative compositions of jeffbenite (wt%)

	Brazil					Machado	Guinea
Country							
Area	Juina						Kankan
Location	Collier-4 pipe	Sao Luiz placer		Rio Vermelho placer	Rio Soriso placer	Placer	Placer
Sample No.	J4-1	BZ207A	BZ259A2	Juina 4-104	1-5A2	P33-1b	KK-108a
Assemblage	Jeffbenite + Magnesite	Jeffbenite + Brd + fPer	2Jeffbenite + Brd + NaAl-silicate	Jeffbenite + Brd	Jeffbenite + Brd + fPer + 'Ol'	Jeffbenite + Brd + 'Ol'	Jeffbenite + 2Brd + 2fPer + Ga
SiO_2	36.05	39.93	41.83	37.75	39.99	30.49	47.00
TiO_2	3.56	4.23	0.02	7.55	4.71	2.76	1.01
Al_2O_3	17.82	20.01	23.15	16.96	19.03	13.08	7.79
Cr_2O_3	0.01	1.34	2.40	1.74	2.74	0.07	0.02
FeO	20.12	9.51	4.43	10.06	6.87	14.80	14.53
NiO	n.a.	0.02	0.01	n.a.	n.a.	0.04	0.03
MnO	0.37	0.27	0.65	0.16	0.14	<0.02	0.41
MgO	17.99	25.16	26.91	24.39	25.75	37.01	12.86
CaO	0.04	0.03	0.11	0	0.04	<0.01	11.72
Na_2O	0.10	0.02	0.15	n.a.	n.a.	0.08	1.13
K_2O	0.04	0.01	0.01	n.a.	n.a.	0.03	0.80
Total	96.10	100.53	99.67	98.61	99.27	98.36	97.28
fe	0.385	0.175	0.084	0.188	0.130	0.183	0.388
mg	0.615	0.825	0.916	0.812	0.870	0.817	0.612
References	Nestola et al. (2016b)	Hutchison (1997)		Kaminsky et al. (2001)	Hayman et al. (2005)	Burnham et al. (2016)	Stachel et al. (2000)

Note: *n.a.* not analysed
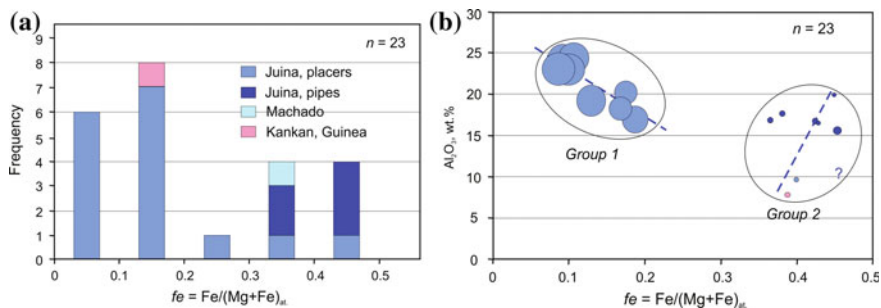
Fig. 4.36 Chemical characteristics of jeffbenite. **a** Distribution of iron index *fe* in jeffbenite. **b** Al_2O_3 versus *fe* in jeffbenite. Cr concentrations in jeffbenite are shown as *circles*, the radii of which are proportional to the Cr contents. Data from Hutchison (1997), Stachel et al. (2000), Kaminsky et al. (2001), Hayman et al. (2005), Bulanova et al. (2010), Thomson et al. (2014), Zedgenizov et al. (2014a), Burnham et al. (2016), Nestola et al. (2016b)
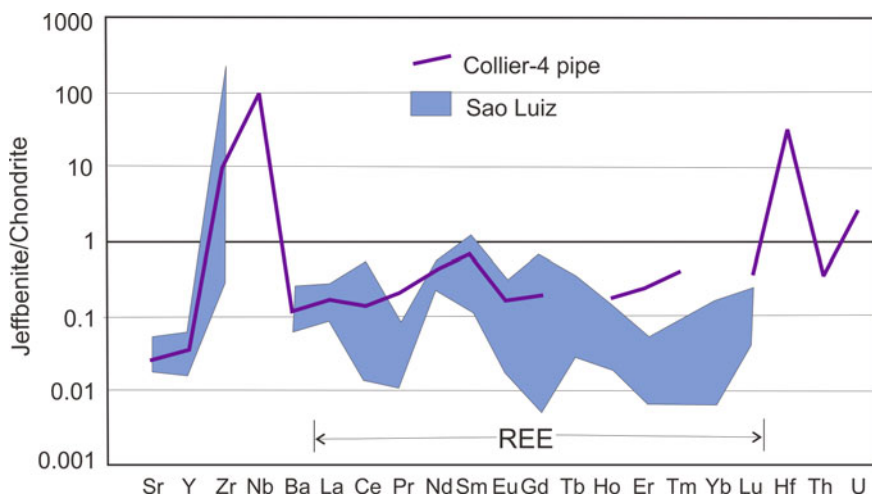
Fig. 4.37 Chondrite-normalised trace element patterns in jeffbenite from Brazil. Data from Hutchison et al. (2001), Bulanova et al. (2010), Harte et al. (1999). Chondrite composition was derived from McDonough and Sun (1995). After Kaminsky (2012). © Elsevier

coordination. These cation occupations in the lattice lead to small charge deficiencies at all cation sites, making a small amount of cation transfer in the lattice possible.

Finger and Conrad (2000) further studied one of the earlier examined jeffbenite samples and, in general, confirmed the initial assignment of the tetrahedral crystal structure. However, they proposed a revised model for the cation occupancies and simplified the formula as $^{VIII\text{-}IV}(Mg,Fe)^{VIII}(Al,Mg,Fe)_4[^{IV}(SiAl)O_4]_3$. The latest structural study of jeffbenite provided a more general formula of $Mg_3Al_2Si_3O_{12}$ with unit cell parameters of $a = 6.5231$ Å and $c = 18.1756$ Å (Nestola et al. 2015, 2016b). Considering the fact that jeffbenite always contains some other cation substitutions in nature, the proposed general formula can be presented as $(Mg,Fe^{2+},$
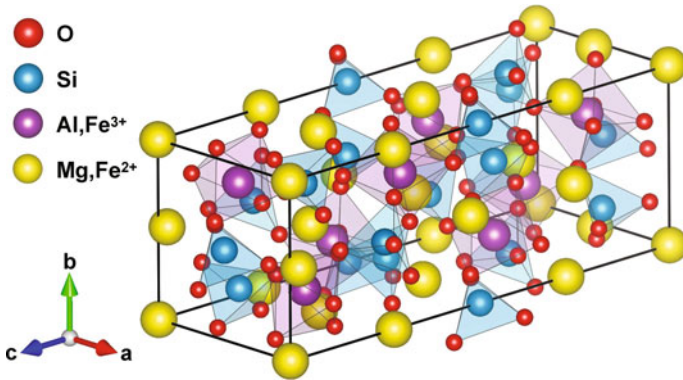
Fig. 4.38 Tetragonal crystal structure of jeffbenite (space group $I\bar{4}2d$). Lattice parameters from Nestola et al. (2016b)

Ca)$_3$(Al,Fe^{3+},Cr)$_2$(Si,Ti)$_3$O$_{12}$ (Fig. 4.38). It should be noted that all structural studies were performed for the low-Fe high-Cr 'juvenile' group of jeffbenite.

Jeffbenite was suggested to have a limited P–T stability field in moderately aluminous bulk compositions of the uppermost lower mantle (Harris et al. 1997). Recent experiments demonstrated that the stability field of jeffbenite extends to higher pressures than previously determined (Anzolini et al. 2016b).

4.9   Majorite Garnet

4.9.1   General

Majorite garnet, or majorite Mg$_3$(Mg,Fe,Al,Si)$_2$Si$_3$O$_{12}$ (in which there is an excess of Si in octahedral coordination) is the major mineral of the transition zone (e.g., Harte 2010). In majorite grains from the Monastery and Jagersfontein pipes, South Africa, the silica excess is as high as X_{Si} = 3.2–3.6 (Moore and Gurney 1985; Chinn et al. 1998; Tappert et al. 2005b). Some experimental studies have demonstrated that majorite is stable at pressures of up to 28 GPa (Irifune and Ringwood 1993). The association of majorite, in diamond from the Juina placers in Brazil, with perovskite and ilmenite (Wilding et al. 1991; Kaminsky et al. 2001) allows for its possible presence in the uppermost parts of the lower mantle. However, it is difficult to distinguish lower-mantle majorite; most of them are from the transition-zone.

4.9.2   Chemical Composition

The chemical compositions of the observed majorite varies within a wide range of mg = 0.402–0.895; mostly within the range of mg = 0.55–0.70 (Table 4.18;

Table 4.18 Representative compositions of majorite (wt%)

	Brazil						Machado	Canada
Country	Brazil							Canada
Area	Juina						Machado	Slave
Location	Sao Luiz				Corrigo Chicoria	Collier 4	Placer	Pipe DO27
Sample No.	BZ237C	28	34	C11	Juina 5-108b	J9-1	P23	97 28(1)
Assemblage	Maj + Brd	Maj + CaSiPrv + CaSiTiPrv + SiO$_2$	Maj + CaSiPv	Maj	Maj + CaSiprv + Ilm	3Maj	Maj	5Maj + Ni-sulph
SiO$_2$	43.37	44.36	41.94	39.41	41.46	42.31	49.13	42.73
TiO$_2$	0.01	0.34	1.66	1.39	1.95	1.06	0.42	0.79
Al$_2$O$_3$	21.47	20.36	18.76	20.40	18.82	21.45	12.41	19.31
Cr$_2$O$_3$	2.96	0.08	0.07	0.04	0.12	0.07	0.21	0.07
FeO	6.02	13.74	13.32	18.91	13.37	14.90	5.14	14.16
NiO	0.02	n.a.	n.a.	n.a.	n.a.	0.02	<0.07	n/a
MnO	0.89	0.28	0.29	0.32	0.3	0.3	0.31	0.29
MgO	22.20	12.69	10.77	7.13	12.46	10.05	24.62	9.87
CaO	1.72	7.29	12.26	9.94	10.7	9.48	8.14	13.05
Na$_2$O	0.27	1.50	0.71	0.93	0.67	0.85	0.30	0.11
K$_2$O	0.01	0.01	0	0.02	n.a.	0	<.04	n.a.
Total	98.94	100.64	99.78	98.48	99.85	100.49	100.68	100.38
fe	0.132	0.378	0.409	0.598	0.376	0.454	0.105	0.446
mg	0.868	0.622	0.591	0.402	0.624	0.546	0.895	0.554
References	Hutchison (1997)	Zedgenizov et al. (2014a)			Kaminsky et al. (2001)	Bulanova et al. (2010)	Burnham et al. (2016)	Davies et al. (2004)

Note: *n.a.* not analysed

Fig. 4.39 Distribution of magnesium index *mg* in majorite inclusions in diamond. Data from Wilding (1990), Hutchison (1997), Davies et al. (2004), Kaminsky et al. (2001), Bulanova et al. (2010), Burnham et al. (2016)

Fig. 4.39). The major admixture is sodium (0.27–1.12 wt% Na_2O), which corresponds to the experimental data regarding the synthesis of majorite with up to 12 mol% of Na in a garnet solid solution (Bobrov et al. 2008a; Dymshits et al. 2010). Na-majorite may be an important concentrator of sodium in the upper part of the lower mantle and transition zone. Sodium majorite $Na_2MgSi_5O_{12}$ has tetragonal structure where excess Si occupies the octahedral site that is compensated for by the entry of Na in the X site of the garnet structure (Bobrov et al. 2008b; Bindi et al. 2011).

Concentrations of trace elements in majorite are usually one to two magnitudes higher than in chondrite, except Ni and Ba, which form negative anomalies (Fig. 4.40).

The patterns of REE in majorite from different regions are also distinct (Fig. 4.40). Majorite from Brazil and Guinea have almost linear, chondritic-like patterns (with a small predominance of LREE in majorite from Guinea), while majorite from South Africa (pipes Monastery and Jagersfontein) are significantly depleted with respect to LREE; the most contrasting distribution for the samples is present in those from the Jagersfontein pipe. Many majorite grains have a positive or a negative Eu anomaly, most likely indicating their 'eclogitic' genesis, with formation of these grains likely to have occurred within subducted lithosphere. This is confirmed by very light isotopic compositions of the hosting diamonds (from −17‰ to −24‰ $\delta^{13}C$ PDB). The other majorite grains, which lack Eu-anomalies, may belong to the ultramafic association.
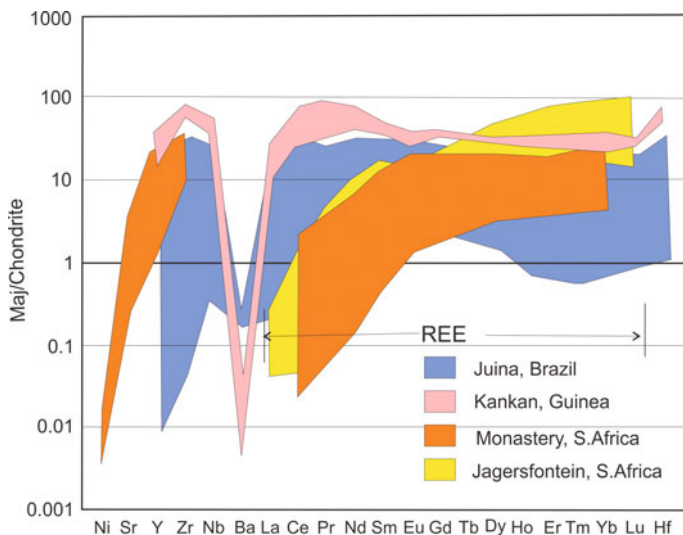
Fig. 4.40 Chondrite-normalised trace element patterns in majorite. Data from Moore et al. (1986), Hutchison et al. (2001), Kaminsky et al. (2001), Stachel et al. (2000), Tappert et al. (2005b), Burnham et al. (2016). Chondrite composition from McDonough and Sun (1995). Modified after Kaminsky (2012), with additions

4.10   Ilmenite

4.10.1   General

Ilmenite (Fe,Mg,Mn)TiO$_3$ is identified in inclusions from Brazilian diamonds together with bridgmanite, ferropericlase, CaSi-perovskite, jeffbenite and titanite, and is attributed to the lower mantle and transition zone origin (Kaminsky et al. 2001, 2009a; Thomson et al. 2014). Three compositional varieties, common ilmenite, Mg-ilmenite (picroilmenite) (Fe,Mg)TiO$_3$ and Mn-ilmenite (manganil-menite) (Fe,Mn)TiO$_3$, occur as inclusions in diamond. Picroilmenite is a common inclusion in upper-mantle diamonds, as well as in all kimberlite pipes worldwide. By contrast, common ilmenite and manganilmenite were not found in diamonds or kimberlites until recently. Of particular interest is manganilmenite, which was previously encountered only as a late- or post-magmatic, metasomatic phase in kimberlites, carbonatites, agpaitic and ultramafic pegmatites, and some other rocks.

Low-magnesium ilmenite (with only 0.11–0.14 wt% MgO) was first reported as an inclusion in three Brazilian diamonds by Meyer and Svisero (1975) who noted that its composition is close to stoichiometry and it does not have high Mg con-centrations, characteristic for kimberlitic picroilmenite. The mineral has only one major impurity, MnO (0.64–0.75 wt%), which is markedly different from kim-berlitic ilmenite. The exact locality of those samples was not mentioned in the literature, however, but it might be related to the Juina area in which extensive
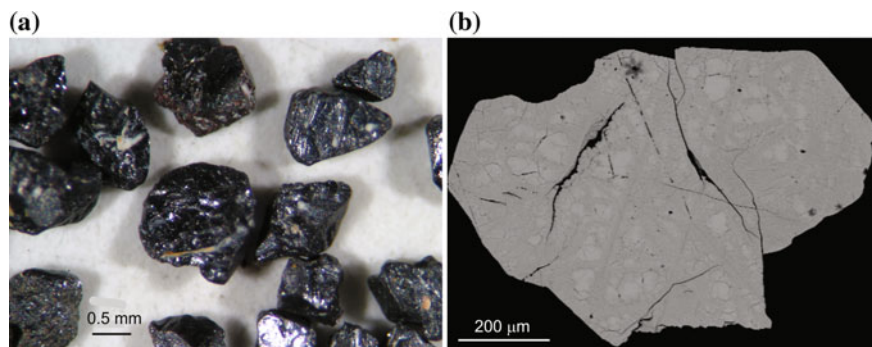
Fig. 4.41 Manganoilmenite from the Juina area, Brazil. **a** General view of grains from the Pandrea-3 kimberlite. **b** Internal structure with minor inhomogeneities. Black-scattered electron image. From Kaminsky and Belousova (2009). © Elsevier

mining for diamonds started in the 1970s. This finding was confirmed in the 1990s, when a series of low-Mg manganoan ilmenite inclusions in Juina placer diamonds was found (Kaminsky et al. 2001). At the same time, inclusions of low-Mg, Mn-ilmenite were found in placer diamonds from Guaniamo, Venezuela (Kaminsky et al. 1997, 2000; Sobolev et al. 1998), and later manganoan ilmenite was found as an inclusion in a diamond from a primary deposit kimberlitic pipe Pandrea-7 in the Juina area (Kaminsky et al. 2009a). In Juina diamonds, manganilmenite was identified, for the first time, as a primary-magmatic phase with a homogeneous, internal structure. In one of the diamond crystals from the Pandrea-7 pipe, manganilmenite occurs with picroilmenite. A great number of Mn-ilmenite grains were identified in this and other kimberlitic rocks from the same area (Fig. 4.41a). They appeared to be low-Mg, manganoan ilmenite, analogous to the composition of the grains included in diamonds, and were considered to be a new kimberlite/diamond indicator mineral (Kaminsky and Belousova 2009). However, the internal structure of the Mn-ilmenite grains shows some inhomogeneous features (Fig. 4.41b).

4.10.2 Chemical Composition and Ilmenite Varieties

The chemical compositions of the ilmenite grains are presented in Table 4.19. All three compositional varieties show significant non-stoichiometry by as much as 10–13% in some samples, which is most likely caused by a high proportion of Fe^{3+} cation substitution in the lattice. Manganilmenite has a MnO content from 0.42 to 6.01 wt% and an elevated vanadium admixture ($V_2O_3 = 0.21–0.43$ wt%); in one grain the MnO content reaches 11.46 wt%. MgO content in all manganilmenite grains varies from less than 0.04 wt% (the analytical detection limit) to 0.81 wt%, while in picroilmenite it is approximately 9.33–11.94 wt%. Analysis of the MnO and MgO contents shows no correlation between each other and with Fe.

Table 4.19 Representative compositions of ilmenites from the Juina area, Brazil (wt%)

Location	Pandrea-7 pipe		Rio Sao Luis placer			Corrigo Chicoria placer	
Sample No.	P7-29		Juina 1-4	Juina 1-32	Juina 1-34	Juina 5-108	Juina 5-56
Mineral association	Pilm + Mn-Ilm		Ilm + fPer	Mn-ilm	Ilm	Mn-Ilm + CaSiPrv + Maj	Pilm
SiO_2	0.03	0.02	0.01	0.01	0.00	0.02	0.04
TiO_2	49.08	55.78	50.22	52.51	50.41	50.13	51.93
Al_2O_3	0.86	0.16	0.00	0.05	0.00	0.00	0.47
Cr_2O_3	0.29	0.00	0.00	0.00	0.00	0.06	0.66
V_2O_3	0.43	0.13	n.a.	n.a.	n.a.	n.a.	n.a.
FeO	38.92	38.08	46.21	39.62	48.24	42.43	32.72
MnO	0.27	2.81	0.73	5.37	0.44	6.01	0.25
NiO	0.05	0.00	0.00	0.00	0.00	0.00	0.11
MgO	9.33	0.12	0.12	0.81	0.40	0.00	11.94
CaO	0.02	0.01	0.03	0.00	0.00	0.03	0.00
ZnO	0.02	0.04	n.a.	n.a.	n.a.	n.a.	n.a.
Na_2O	0.02	0.01	n.a.	n.a.	n.a.	n.a.	n.a.
K_2O	0.01	0	n.a.	n.a.	n.a.	n.a.	n.a.
Total	99.33	97.16	97.32	98.37	99.49	98.68	98.12
fe	0.697	0.926	0.980	0.852	0.977	0.874	0.603
mg	0.298	0.005	0.005	0.031	0.014	0.000	0.392
mn	0.005	0.069	0.016	0.117	0.009	0.126	0.005
References	Kaminsky et al. (2009b)		Kaminsky et al. (2001)				

Note: *n.a.* not analysed

All manganilmenite grains found earlier in carbonatites, gabbro, pegmatites, and other rocks were proposed to be formed at the latest magmatic or postmagmatic, metasomatic stages (Simpson 1929; Vincent and Phillips 1954; Omori and Hasegawa 1955; Snetsinger 1969; Elsdon 1975; Mitchell 1978; Gaspar and Wyllie 1984). They either form reaction rims on grains of picroilmenite and other ore minerals, or compose laths in the groundmass. The manganilmenite from Juina diamonds as well as from the sources of kimberlites is a primary mineral phase, and can be distinguished from the secondary manganilmenite based on their compositional differences (Table 4.20).

Trace element patterns in manganilmenite and picroilmenite are plotted in Fig. 4.42. They show resemblance to each other mineral with very little variation. Both manganilmenite and picroilmenite have high concentrations of V, Zr, Nb, Ta, Th, and U, while Ni, Cr, Co, Ta, and Nb in manganilmenite are less abundant than that in picroilmenite.

Table 4.20 Chemical characteristics of manganilmenite from different localities (Kaminsky and Belousova 2009)

Characteristic	Inclusions in diamond	Kimberlite, Juina, Brazil	Jacupiranga carbonatite, Brazil	Other igneous rocks	Metamorphosed mafic/ultramafic rocks, Western Australia
MnO, wt%	0.42–11.46	0.63–2.49	2.29–7.87	1.44–15.15	1.15–7.38
MgO	0.0.81	0–0.24	15.69–23.46	0.0.46	0.01–0.49
TiO_2	50.13–56.15	55.49–57.79	55.83–59.24	46.23–52.02	42.80–52.66
V_2O_3	0.13	0.21–0.39	–	0.06	0.01–0.43
NiO	0–0.12	0–0.02	4.56–6.80	–	–
$MnTiO_3$, mol %	0.9–23.5	1.3–5.0	4.2–14.6	3.2–40.4	3.0–16.4
$MgTiO_3$, mol %	0–2.0	0–0.6	52.6–75.6	0–6.0	0.1–2.3
References	Kaminsky et al. (2001, 2009a)	Kaminsky and Belousova (2009)	Mitchell (1978)	Simpson (1929), Vincent and Phillips (1954), Omori and Hasegawa (1955), Snetsinger (1969), Elsdon (1975)	Cassidy et al. (1988)
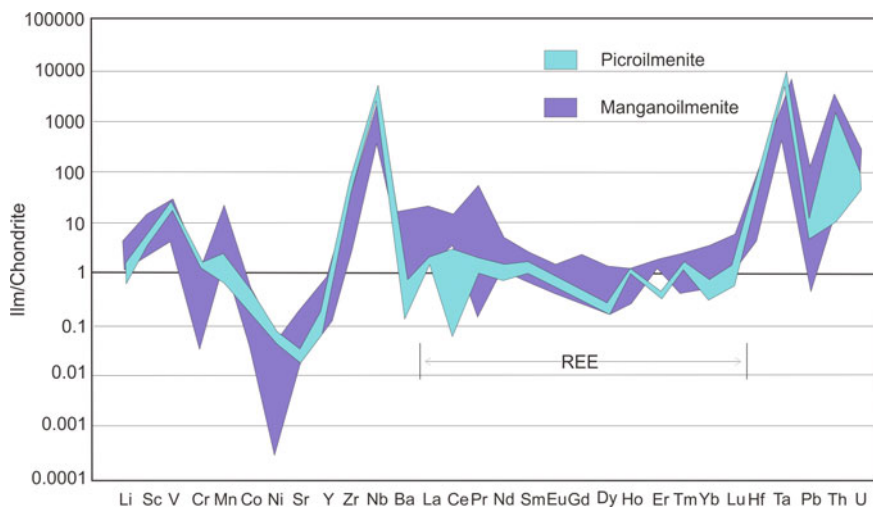
Fig. 4.42 Chondrite-normalised trace element patterns in manganilmenite and picroilmenite. Data from Kaminsky et al. (2001, 2009a). Chondrite composition from McDonough and Sun (1995). Modified after Kaminsky (2012)

4.10.3   Crystal Structure and Phase Stability of Ilmenite

The ilmenite phase with trigonal structure (space group $R\bar{3}$) in the $MgSiO_3$–$FeSiO_3$ system was found in meteorites and named 'akimotoite' after Prof. Syun-iti Akimoto of the University of Tokyo (Tomioka and Fujino 1997, 1999). Akimotoite is believed to be a significant mineral in the Earth's mantle at depths of approximately 600–800 km (at pressures between approximately 21 and 28 GPa). The ilmenite crystal structure can be described as a corundu structure with Mg^{2+} and Si^{4+} located in an ordered alternative fashion in the six-co-ordinated Al^{3+} sites (Liu 1977). At lower-mantle pressures, ilmenite transitions into the bridgmanite structure, which is a 3D framework of the corner-shared SiO_6 octahedra with Mg^{2+} in the pseudo-dodecahedral sites.

When in association with the majoritic garnet (Akaogi et al. 2002; Fei and Bertka 1999), the addition of Al_2O_3 widens the stability field of majorite and suppresses the stability field of ilmenite at high pressures and relatively high temperatures (Akaogi et al. 2002). Across the ilmenite–bridgmanite transition, the addition of Al_2O_3 extends the transition boundary to greater pressures (deeper parts of the lower-mantle conditions). In the ilmenite solid solution, the addition of Al_2O_3 slightly increases the a-axis but decreases the c-axis and molar volume substantially (Akaogi et al. 2002). According to calculations using generalised gradient approximations, ilmenite may be stable only in the uppermost levels of the lower mantle and in the transition zone under a pressure of 20–26 GPa (Yu et al. 2011).

4.11   Other Minerals

A series of other minerals were found in association with major lower-mantle minerals and may be considered to be accessory mineral phases in the deep-Earth mantle. Some of them may occur locally.

4.11.1   Olivine Polymorphs

A mineral phase with a composition identical to olivine $(Mg,Fe)_2SiO_4$ was identified in diamonds from Brazilian kimberlite pipes and placer deposits, Canadian kimberlite pipes, Guinea, and Australia, where it forms colorless grains in association with bridgmanite, ferropericlase, CaSi-perovskites, jeffbenite and some other mineral phases (Wilding et al. 1991; Stachel et al. 2000; Kaminsky et al. 2001; Hayman et al. 2005; Tappert 2005a, 2009a, b; Bulanova et al. 2010; Thomson et al. 2014). These grains have wide variations in Mg (mg = 0.848–0.965) (Table 4.21). The distribution of mg in 'olivine' grains is similar to the one in bridgmanite (Fig. 4.43a) with an almost identical value range and average mg = 0.908 (0.917 in bridgmanite) and bimodality. The latter is most likely caused by different compositions of this mineral in different areas: in Brazil, this phase has less magnesium

Table 4.21 Representative analyses of mineral phase with a composition identical to olivine (wt%)

	Brazil					Canada	Guinea	Australia
Country	Brazil					Canada	Guinea	Australia
Area	Juina					Northwest Territories	Kankan	Orroroo
Location	Pipe Juina-5	Corrigo Chicoria	Sao Luiz placer	Rio Soriso placer	Rio Soriso	Pipe DO27	Placer	Dyke Eurelia K7
Sample No.	Ju5-73	Juina 5-5	80	3-2S	4-3C	DO270300	KK-44e	FBS5-12
Assemblage	'Ol' + fPer	'Ol' + fPer	'Ol' + Brd + CaSiPrv	'Ol' + Brd + fPer + CaSiPrv	'Ol' + Brd + fPer	'Ol' + 3Brd + fPer	'Ol' + 3Brd + fPer + CaSiPrv	'Ol'
SiO_2	41.55	40.31	40.5	39.42	42.74	41.70	41.02	40.78
TiO_2	0.00	n.a.	n.a.	n.a.	0.07	0.00	0.01	0.02
Al_2O_3	0.02	0.03	n.a.	n.a.	0.8	0.03	0.04	0.00
Cr_2O_3	0.14	0.15	n.a.	n.a.	n.a.	0.00	0.07	0.07
FeO	9.25	10.79	14.1	11.15	4.61	3.52	6.15	8.45
NiO	0.45	0.37	0.24	n.a.	n.a.	0.08	0.09	0.47
MnO	0.09	n.a.	n.a.	0.12	0.15	0.09	0.11	0.11
MgO	48.22	47.42	44.1	48.85	51.96	53.80	52.26	48.81
CaO	0.00	n.a.	n.a.	0.07	n.a.	0.05	0.01	0.06
Na_2O	0.05	0.04	n.a.	n.a.	n.a.	0.00	0.02	0.00
K_2O	0.01	n.a.	n.a.	n.a.	n.a.	n.a.	0.00	0.00
Total	99.79	99.11	99.02	99.61	100.33	99.27	99.83	98.77
fe	0.097	0.113	0.152	0.113	0.047	0.035	0.062	0.088
mg	0.903	0.887	0.848	0.887	0.953	0.965	0.938	0.912
References	Thomson et al. 2014	Kaminsky et al. (2001)	Zedgenizov et al. (2014a)	Hayman et al. (2005)		Davies et al. (2004a)	Stachel et al. (2000)	Tappert et al. (2005a)

Note: *n.a.* not analysed
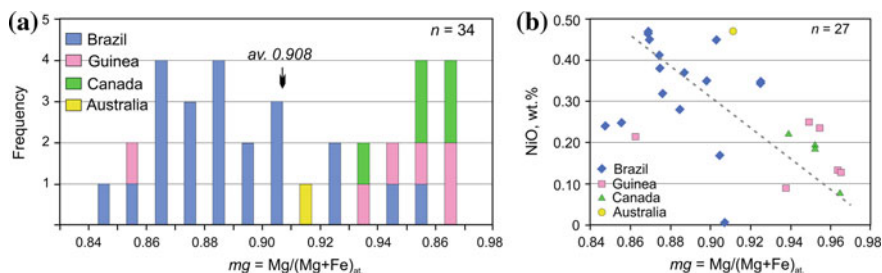
Fig. 4.43 Chemical characteristics of mineral phase with a composition of olivine. **a** Distribution of magnesium index *mg* in the mineral. **b** NiO versus *mg*. Data from Wilding (1990), Hutchison (1997), Stachel et al. (2000), Kaminsky et al. (2001), Davies et al. (2004), Hayman et al. (2005), Tappert et al. (2009a, b), Bulanova et al. (2010), Thomson et al. (2014), Zedgenizov et al. (2014a)

than in other areas. The Mg concentration shows a non-strong negative correlation with Ni (Fig. 4.43b).

This phase is most likely a product of a retrograde transformation from a lower-mantle mineral, or a retrograde reaction fPer + Brd → Ol. The latter is less possible because it associates (in diamond) not only with ferropericlase but also with bridgmanite, sometimes in a 'touching' association. None of the 'olivine' grains were studied structurally. It is not excluded that these grains are, in fact, ringwoodite from the uppermost layers from the lower mantle.

4.11.2   Titanite

Titanite ($CaTiSiO_5$) was identified in placers of Rio Chicoria (Kaminsky et al. 2001) and Rio Soriso (Hayman et al. 2005) in the Juina area, Brazil, where it associates with CaSi-perovskite. Its chemical composition (in wt%) is: 33.04 SiO_2; 29.70 TiO_2; 3.16 Al_2O_3; 0.06 FeO; 27.75 CaO. Low total for bulk composition (93.70%) suggests the existence of other, non-analyzed elements in the mineral. Structural analysis of this mineral in diamond inclusions has not been performed, although it is possible that it is a polymorph modification of $CaTiSiO_5$.

4.11.3   Merwinite

The inclusion of merwinite ($Ca_{2.85}Mg_{0.96}Fe_{0.11}Si_{2.04}O_8$) was first detected by Raman spectroscopy in the core zone of one Sao-Luiz diamond, Brazil in association with the inclusions of walsromite-structured $CaSiO_3$ and olivine of $(Mg_{0.86}Fe_{0.14})_2SiO_4$ composition (Zedgenizov et al. 2014b). Merwinite was found to contain microinclusions of calcite.

The existing experimental data (Sharygin et al. 2012) indicate that under mantle conditions merwinite can be only formed in specific, Ca-rich and Mg- and Si-depleted environments, which differ from any known mantle lithology. Such chemical conditions can occur during interaction of Ca-rich carbonatite melts with ultramafic mantle, which would eventually lead to crystallization of $CaSiO_3$ and merwinite together with late olivine after re-equilibration of Ca and Mg (Zedgenizov et al. 2014b, 2016).

4.11.4 Native Nickel

Native nickel (Ni^0) associated with CaSi-perovskite was identified in diamond from Rio São Luiz (Wilding et al. 1991) and Rio Chicoria (Kaminsky et al. 2001) in the Juina area, Brazil. Native nickel is also found in pipe DO27, Canada, occurring with ferropericlase and MgSi-perovskite (Davies et al. 2004). Its peculiar chemical feature is a noticeable admixture of potassium (in the sample from the Chicoria, 0.21 wt% K_2O). Other admixtures include (in wt%): Fe (1.01–1.29 FeO), Ti (0.02–0.07 TiO_2), Cr (0.01 Cr_2O_3), Mn (0.07 MnO), and Na (0.02 Na_2O).

4.11.5 Native Iron

Native iron (Fe^0) was identified in diamonds from the Rio Soriso placer in association with low-Ni pyrrhotite (Hayman et al. 2005) and from the Pandrea-1 pipe in association with ferropericlase and chrome spinel (Kaminsky et al. 2009a), both from the Juina area, Brazil; and from the placer Kankan in Guinea (Stachel et al. 2000). The mineral is notably rich in Cr (0.77–1.62 wt%), as well as in Ni (0.22–0.31 wt%), Mg (0.10–0.57 wt%), Mn (0.13–0.36 wt%), Ti (0.01–0.07 wt%) and Al (0.05–0.14 wt%).

4.11.6 Unidentified Si–Mg Phase

An unidentified mineral of Si–Mg with a Si/Mg atomic ratio of ∼4/3 (1.37) was observed in a diamond from the Chicoria placer in Brazil, occurring in association with perovskite, manganilmenite, and majorite (i.e., a lower-mantle origin is not obvious) (Kaminsky et al. 2001). The composition of the mineral consists only of Si (61.95 wt% SiO_2) and Mg (30.33 wt% MgO), with admixtures of Al (0.10 wt% Al_2O_3) and Fe (0.45 wt% FeO). Considering the low analytical totals (92.71 wt%) for this material, the presence of volatiles in this phase may be suggested.

4.11.7   Moissanite

Moissanite SiC, another potential lower mantle phase, was identified in diamonds from the São Luiz placer deposit (Wilding et al. 1991), but it is found to be unassociated with other minerals.

4.12   Conclusions

The juvenile ultramafic association predominates in the lower mantle. It is composed of bridgmanite + ferropericlase + CaSi-perovskite + free silica. This association, in contrast to the upper mantle, consists not of silicates but predominantly of oxides, and the traditional term 'silicate mantle' is not applicable to the lower mantle. It should be referred to as the 'oxide mantle'. Of particular importance, the presence of iron-rich ferropericlase-magnesiowüstite and free silica in the ultramafic association disagrees with the proposed pyrolitic composition of the lower mantle.

Bridgmanite has a high-Mg composition (mg = 0.84–0.96) and variable admixture of Al (0.25–12.58 wt% Al_2O_3). Two groups of bridgmanite are distinguished: low-Al (0.25–3.10 wt% Al_2O_3) and high-Al (8.34–12.58 wt% Al_2O_3). Natural high-Mg bridgmanite does not experience any phase transitions in the lower mantle down to the D″ border. The addition of Fe in bridgmanite causes an increase in its density, bulk modulus and bulk sound velocity, independently of the Al concentration, at lower-mantle pressures. The incorporation of Al either has no effect on the thermodynamic properties of bridgmanite or slightly decreases its bulk modulus; in any case, it does not appear to be significant for seismologic interpretations. The orthorhombic structure of bridgmanite is stable within the entire lower mantle down to the D″ layer, where it transforms into the post-perovskite phase.

Ferropericlase occurs in geological samples more frequently than was expected from experimental and theoretic data. Its chemical composition is different to that predicted, with magnesium index mg varying widely from 0.90 to 0.36, most likely caused by magma fractional crystallization in the lower mantle. Ferropericlase remains stable within the entire lower mantle with the cubic rocksalt structure; however, high Fe-rich varieties at subsolidus temperatures may obtain rhombohedral and hexagonal structures.

Iron contents in both ferropericlase and bridgmanite increase with depth, reflecting the increasing Fe content in the bulk composition of the lowermost mantle.

The occurrence of ∼8.4% free silica (stishovite and $CaCl_2$–structured polymorph) is most likely cause by more silica-rich composition of the lower mantle compared with the upper mantle. The presence of free silica may create faster seismic velocities by a few percent. At a depth of 1600–1800 km (70–80 GPa pressure range), stishovite transforms into the $CaCl_2$-structured polymorph, which should cause the reduction of seismic velocities (particularly V_s).

In addition to major minerals, a variety of other mineral phases occurs in the lower mantle: Mg–Cr–Fe, Ca–Cr and other orthorhombic oxides, jeffbenite, ilmenite (including picroilmenite and manganilmenite), titanite, native Ni and Fe, moissanite, and some others.

References

Adams, D. J., & Oganov, A. R. (2006). Ab initio molecular dynamics study of CaSiO$_3$ perovskite at P–T conditions of Earth's lower mantle. *Physical Review B, 73,* 184106.

Akaogi, M. (2007). Phase transitions of minerals in the transition zone and upper part of the lower mantle. In E. Ohtani (Ed.), *Advances in High Pressure Mineralogy* (Vol. 421, pp. 1–13). Geological Society of America Memoirs.

Akaogi, M., Hamada, Y., Suzuki, T., Kobayashi, M., & Okada, M. (1999). High pressure transitions in the system MgAl$_2$O$_4$–CaAl$_2$O$_4$: A new hexagonal aluminous phase with implication for the lower mantle. *Physics of the Earth and Planetary Interiors, 115,* 67–77.

Akaogi, M., Tanaka, A., & Ito, E. (2002). Garnet–ilmenite–perovskite transitions in the system Mg$_4$Si$_4$O$_{12}$–Mg$_3$Al$_2$Si$_3$O$_{12}$ at high pressures and high temperatures: Phase equilibria, calorimetry and implications for mantle structure. *Physics of the Earth and Planetary Interiors, 132,* 303–324.

Akber-Knutson, S., & Bukowinski, M. S. T. (2004). The energetics of aluminum solubility into MgSiO$_3$ perovskite at lower mantle conditions. *Earth and Planetary Science Letters, 220,* 317–330. doi:10.1016/S0012-821X(04)00065-2

Akber-Knutson, S., Bukowinski, M. S. T., & Matas, J. (2002). On the structure and compressibility of CaSiO$_3$ perovskte. *Geophysical Research Letters, 29*(3), 1034–1037.

Anderson, D. L. (1983). Chemical composition of the mantle. *Journal of Geophysical Research, 88,* B41–B52. doi:10.1029/Jb088is01p00b41

Anderson, D. L. (2002). The case for irreversible chemical stratification of the mantle. *International Geology Review, 44*(2), 97–116.

Andrault, D. (2001). Evaluation of (Mg, Fe) partitioning between silicate perovskite and magnesiowüstite up to 120 GPa and 2300 K. *Journal of Geophysical Research, 106*(B2), 2079–2087.

Andrault, D., Angel, R. J., Mosenfelder, J. I., & Le Bihan, T. (2003). Equation of state of stishovite to lower mantle pressures. *American Mineralogist, 88,* 301–307.

Andrault, D., Bolfan-Casanova, N., Bouhifd, M. A., Guignot, N., & Kawamoto, T. (2007). The role of Al-defects on the equation of state of Al–(Mg, Fe)SiO$_3$ perovskite. *Earth and Planetary Science Letters, 263,* 167–179. doi:10.1016/j.epsl.2007.08.012

Andrault, D., Bolfan-Casanova, N., & Guignot, N. (2001). Equation of state of lower mantle (Al, Fe)-MgSiO$_3$ perovskite. *Earth and Planetary Science Letters, 193*(3–4), 501–508.

Andrault, D., Fiquet, G., Guyot, F., & Hanfland, M. (1998a). Pressure-induced Landau-type transition in stishovite. *Science, 282*(5389), 720–724.

Andrault, D., Neuville, D. R., Flank, A. M., & Wang, Y. (1998b). Cation sites in Al-rich MgSiO$_3$ perovskites. *American Mineralogist, 83,* 1045–1053.

Andrault, D., Pesce, G., Bouhifd, M. A., Bolfan-Casanova, N., Hénot, J.-M., & Mezouar, M. (2014). Melting of subducted basalt at the core-mantle boundary. *Science, 344*(6186), 892–895.

Andrault, D., Petitgirard, S., Lo Nigro, G., Devidal, J.-L., Veronesi, G., Garbarino, G., et al. (2012). Solid-liquid iron partitioning in Earth's deep mantle. *Nature, 487,* 354–357.

Antonangeli, D., Siebert, J., Aracne, C. M., Farber, D. L., Bosak, A., Hoesch, M., et al. (2011). Spin crossover in ferropericlase at high pressure: A seismologically transparent transition? *Science, 331,* 64–67.

Anzolini, C., Angel, R. J., Merlini, M., Derzsi, M., Tokár, K., Milani, S., et al. (2016a). Depth of formation of $CaSiO_3$-walstromite included in super-deep diamonds. *Lithos, 265,* 138–147. doi:10.1016/j.lithos.2016.09.025

Anzolini, C., Drewitt, J., Lord, O. T., Walter, M. J., & Nestola, F. (2016b). New stability field of jeffbenite (ex-"TAPP"): Possibility of super-deep origin. AGU Fall Meeting Abstract MR33A-2675, 1 p.

Armstrong, L. S., & Walter, M. J. (2012). Tetragonal almandine pyrope phase (TAPP): Retrograde Mg-perovskite from subducted oceanic crust? *European Journal of Mineralogy, 24*(4), 587–597.

Armstrong, L. S., Walter, M. J., Tuff, J. R., Lord, O. T., Lennie, A. R., Kleppe, F. R., et al. (2012). Perovskite phase relations in the system $CaO–MgO–TiO_2–SiO_2$ and implications for deep mantle lithologies. *Journal of Petrology, 53*(3), 611–635. doi:10.1093/petrology/egr073

Asahara, Y., Hirose, K., Ohishi, Y., Hirao, N., Ozawa, H., & Murakami, M. (2013). Acoustic velocity measurements for stishovite across the post-stishovite phase transition under deviatoric stress: Implications for the seismic features of subducting slabs in the mid-mantle. *American Mineralogist, 98*(11–12), 2053–2062. doi:10.2138/am.2013.4145

Auzende, A.-L., Badro, J., Ryerson, F. J., Weber, P. K., Fallon, S. J., Addad, A., et al. (2008). Element partitioning between magnesium silicate perovskite and ferropericlase: New insights into bulk lower-mantle geochemistry. *Earth and Planetary Science Letters, 269,* 164–174. doi:10.1016/j.epsl.2008.02.001

Badro, J., Fiquet, G., Guyot, F., Rueff, J.-P., Struzhkin, V. V., Vankó, G., et al. (2003). Iron partitioning in Earth's mantle: Toward a deep lower mantle discontinuity. *Science, 300*(5620), 789–791. doi:10.1126/science.1081311

Barnes, S. J., & Roeder, P. L. (2001). The range of spinel compositions in terrestrial mafic and ultramafic rocks. *Journal of Petrology, 42,* 2279–2302.

Bass, J. D. (2008). Recent progress in studies of the elastic properties of earth materials. *Physics of the Earth and Planetary Interiors, 170,* 207–209.

Bassett, W. A. (2001). The birth and development of laser heating in DACs. *Review of Scientific Instruments, 72,* 1270–1272.

Becerro, A. I., McCammon, C. A., Langenhorst, F., Angel, R. J., & Seifert, F. (1999). Oxygen vacancy ordering in $CaTiO_3–CaFeO_{2.5}$. *Phase Transitions, 69,* 133–146.

Belonoshko, A. B., Dubrovinsky, L. S., & Dubrovinsky, N. A. (1996). A new high-pressure silica phase obtained by molecular dynamics. *American Mineralogist, 81,* 785–788.

Bina, C. R. (2010). Scale limits of free-silica seismic scatterers in the lower mantle. *Physics of the Earth and Planetary Interiors, 183,* 110–114.

Bindi, L., Dymshits, A. M., Bobrov, A. V., Litasov, K. D., Shatsky, A. F., Ohtani, E., et al. (2011). Crystal chemistry of sodium in the Earth's interior: The structure of $Na_2MgSi_5O_{12}$ synthesized at 17.5 GPa and 1700 °C. *American Mineralogist, 96*(2–3), 447–450.

Bindi, L., Tamarova, A., Bobrov, A. V., Sirotkina, E. A., Tschauner, O., Walter, M. J., et al. (2016). Incorporation of high amounts of Na in ringwoodite: Possible implications for transport of alkali into lower mantle. *American Mineralogist, 101,* 483–486.

Bläß, U. W., Langenhorst, F., Frost, D. J., & Seifert, F. (2007). Oxygen deficient perovskites in the system $CaSiO_3–CaAlO_{2.5}$ and implications for the Earth's interior. *Physics and Chemistry of Minerals, 34,* 363–376.

Bobrov, A. V., Kojitani, H., Akaogi, M., & Litvin, Yu A. (2008a). Phase relations on the diopside-hedenbergite-jadeite join up to 24 GPa and stability of Na-bearing majorite garnet. *Geochimica et Cosmochimica Acta, 72*(9), 2392–2408.

Bobrov, A. V., Litvin, Yu A, Bindi, L., & Dymshits, A. M. (2008b). Phase relations and formation of sodium-rich majorite garnet in the system $Mg_3Al_2Si_3O_{12}–Na_2MgSi_5O_{12}$ at 7.0 and 8.5 GPa. *Contributions to Mineralogy and Petrology, 156*(2), 243–257.

Bolfan-Casanova, N., Andrault, D., Amiguet, E., & Guignot, N. (2009). Equation of state and post-stishovite transformation of Al-bearing silica up to 100 GPa and 3000 K. *Physics of the Earth and Planetary Interiors, 174,* 70–77. doi:10.1016/j.pepi.2008.06.024

Boujibar, A., Bolfan-Casanova, N., Andrault, D., Bouhifd, M. A., & Trcera, N. (2016). Incorporation of Fe^{2+} and Fe^{3+} in bridgmanite during magma ocean crystallization. *American Mineralogist, 101,* 1560–1570. doi:10.2138/am-2016-5561

Brenker, F. E., Stachel, T., & Harris, J. W. (2002). Exhumation of lower mantle inclusions in diamond: ATEM investigation of retrograde phase transitions, reactions and exsolution. *Earth and Planetary Science Letters, 198,* 1–9.

Brodholt, J. P. (2000). Pressure-induced changes in the compression mechanism of aluminous perovskite in the Earth's mantle. *Nature, 407,* 620–622.

Bulanova, G. P., Smith, C. B., Kohn, S. C., Walter, M. J., Gobbo, L., & Kearns, S. (2008). Machado River, Brazil—A newly recognised ultradeep diamond occurrence. In *9th International Kimberlite Conference*. Extended Abstract No. 9IKC-A-00233.

Bulanova, G. P., Walter, M. J., Smith, C. B., Kohn, S. C., Armstrong, L. S., Blundy, J., et al. (2010). Mineral inclusions in sublithospheric diamonds from Collier 4 kimberlite pipe, Juina, Brazil: Subducted protoliths, carbonated melts and primary kimberlite magmatism. *Contributions to Mineralogy and Petrology, 159*(4), 489–510. doi:10.1007/s00410-010-0490-6

Burnham, A. D., Bulanova, G. P., Smith, C. B., Whitehead, S. C., Kohn, S. C., Gobbo, L., et al. (2016). Diamonds from the Machado River alluvial deposit, Rondônia, Brazil, derived from both lithospheric and sublithospheric mantle. *Lithos, 265,* 199–213. doi:10.1016/j.lithos.2016.05.022

Cammarano, F., & Romanowicz, B. (2007). Insights into the nature of the transition zone from physically constrained inversion of long-period seismic data. *Proceedings of the National Academy of the U.S.A., 104*(22), 9139–9144.

Caracas, R., Wentzcovitch, R., Price, G. D., & Brodholt, J. (2005). $CaSiO_3$ perovskite at lower mantle pressures. *Geophysical Research Letters, 32,* L06306. doi:10.1029/2004GL022144

Carpenter, M. A. (2006). Elastic properties of minerals and the influence of phase transitions. *American Mineralogist, 91,* 229–246.

Carpenter, M. A., Hemley, R. J., & Mao, H.-K. (2000). High-pressure elasticity of stishovite and the $P4_2/mnm \leftrightarrow Pnnm$ phase transition. *Journal of Geophysical Research, 105,* 10807–10816.

Carpenter, M. A., & Salje, E. K. H. (1998). Elastic anomalies in minerals due to structural phase transitions. *European Journal of Mineralogy, 10,* 693–812.

Cassidy, K. F., Groves, D. I., & Binns, R. A. (1988). Manganoan ilmenite formed during regional metamorphism of Archean mafic and ultramafic rocks from Western Australia. *Canadian Mineralogist, 26*(4), 999–1012.

Chao, E. C. T., Fahey, J. J., Littler, J., & Milton, D. J. (1962). Stishovite, SiO_2, a very high pressure new mineral from Meteor Crater, Arizona. *Geophysical Research, 67,* 419–421.

Chen, M., Shu, J., & Mao, H.-K. (2008). Xieite, a new mineral of high-pressure $FeCr_2O_4$ polymorph. *Chinese Science Bulletin, 53,* 3341–3345.

Chen, M., Shu, J., Mao, H.-K., Xie, X., & Hemley, R. J. (2003a). Natural occurrence and synthesis of two new postspinel polymorphs of chromite. *Proceedings of the National Academy of the U.S.A., 100,* 14651–14654.

Chen, M., Shu, J., Xie, X., & Mao, H.-K. (2003b). Natural $CaTi_2O_4$-structured $FeCr_2O_4$ polymorph in the Suizhou meteorite and its significance in mantle mineralogy. *Geochimica et Cosmochimica Acta, 67,* 3937–3942.

Chinn, J. L., Milledge, H. J., & Gurney, J. J. (1998). Diamonds and inclusions from the Jagersfontein kimberlite. In *Seventh International Kimberlite Conference Extended Abstracts* (pp. 156–157), Cape Town.

Chizmeshya, A. V. G., Wolf, G. H., & McMillan, P. F. (1996). First-principles calculation of the equation-of-state, stability, and polar optic modes of $CaSiO_3$ perovskite. *Geophysical Research Letters, 23*(20), 2725–2728.

Chizmeshya, A. V. G., Wolf, G. H., & McMillan, P. F. (1998). Correction to "First-principles calculation of the equation-of-state, stability, and polar optic modes of $CaSiO_3$ perovskite". *Geophysical Research Letters, 25*(5), 711.

Chung, J. I., & Kagi, H. (2002). High concentration of water in stishovite in the MORB system. *Geophysical Research Letters, 29*(21), 2020. doi:10.1029/2002GL015579

Civet, F., Thëbault, E., Verhoeven, O., Langlais, B., & Saturnino, D. (2015). Electrical conductivity of the Earth's mantle from the first Swarm magnetic field measurements. *Geophysical Research Letters, 42,* 3338–3346.

Cohen, R. E. (1987). Calculation of elasticity and high pressure instabilities in corundum and stishovite with the potential induced breathing model. *Geophysical Research Letters, 14*(1), 37–40.

Cohen, R. E. (1991). Bonding and elasticity of stishovite SiO_2 at high pressure: Linearized augmented plane wave calculations. *American Mineralogist, 76,* 733–742.

Coppari, F., Smith, R. F., Eggert, J. H., Wang, J., Rygg, J. R., Lazicki, A., et al. (2013). Experimental evidence for a phase transition in magnesium oxide at exoplanet pressures. *Nature Geoscience, 6,* 926–929.

Corgne, A., Liebske, C., Wood, B. J., Rubie, D. C., & Frost, D. J. (2005). Silicate perovskite-melt partitioning of trace elements and geochemical signature of a deep perovskitic reservoir. *Geochimica et Cosmochimica Acta, 146,* 249–260.

Corgne, A., & Wood, B. J. (2002). $CaSiO_3$ and $CaTiO_3$ perovskite-melt partitioning of trace elements: Implications for gross mantle differentiation. *Geophysical Research Letters*, *29*. doi:10.1029/2001GL014398

Crowhurst, J., Brown, J., Goncharov, A., & Jacobsen, S. (2008). Elasticity of (Mg, Fe)O through the spin transition of iron in the lower mantle. *Science, 319,* 451–453. doi:10.1126/science.1149606

Daniel, I., Bass, J. D., Fiquet, G., Cardon, H., Zhang, J. Z., & Hanfland, M. (2004). Effect of aluminium on the compressibility of silicate perovskite. *Geophysical Research Letters, 31,* L15608.

Daniel, I., Cardon, H., Fiquet, G., Guyot, F., & Mezouar, M. (2001). Equation of state of Al-bearing perovskite to lower mantle pressure conditions. *Geophysical Research Letters, 28* (19), 3789–3792.

Davies, R. M., Griffin, W. L., O'Reilly, S. Y., & Doyle, B. J. (2004). Mineral inclusions and geochemical characteristics of microdiamonds from the DO27, A154, A21, A418, DO18, DD17 and Ranch Lake kimberlites at Lac de Gras, Slave Craton, Canada. *Lithos, 77*(1–4), 39–55. doi:10.1016/j.lithos.2004.04.016

Dera, P., Prewitt, C. T., Boctor, N. Z., & Hemley, R. J. (2002). Characterization of a high-pressure phase of silica from the Martian meteorite Shergotty. *American Mineralogist, 87,* 1018–1023.

Deschamps, F., & Khan, A. (2016). Electrical conductivity as a constraint on lower mantle thermo-chemical structure. *Earth and Planetary Science Letters, 450*(2016), 108–119. doi:10.1016/j.epsl.2016.06.027

Dorfman, S. M., Meng, Y., Prakapenka, V. B., & Duffy, T. S. (2013). Effects of Fe-enrichment on the equation of state and stability of (Mg, Fe)SiO_3 perovskite. *Earth and Planetary Science Letters, 361,* 249–257. doi:10.2138/am-2015-5190

Dorfman, S. M., Prakapenka, V. B., Meng, Y., & Duffy, T. S. (2012). Intercomparison of pressure standards (Au, Pt, Mo, MgO, NaCl and Ne) to 2.5 Mbar. *Journal of Geophysical Research, 117,* B08210.

Driver, K. P., Cohen, R. E., Wu, Z., Militzer, B., Ríos, P. L., Towler, M. D., et al. (2010). Quantum Monte Carlo for minerals at high pressures: Phase stability, equations of state, and elasticity of silica. *Proceedings of the National Academy of the U.S.A., 107,* 9519–9524. doi:10.1073/pnas.0912130107

Dubrovinsky, L. S., Dubrovinskaia, N. A., Annersten, H., Halenius, E., & Harryson, H. (2001a). Stability of (Mg$_{0.5}$Fe$_{0.5}$)O and (Mg$_{0.8}$Fe$_{0.2}$)O magnesiowüstites in the lower mantle. *European Journal of Mineralogy, 13*(5), 857–861.

Dubrovinsky, L. S., Dubrovinskaia, N. A., Prakapenka, V., Seifert, F., Langenhorst, F., Dmitriev, V., et al. (2003). High-pressure and high-temperature polymorphism in silica. *High Pressure Research, 23*(1–2), 35–39.

Dubrovinsky, L. S., Dubrovinskaia, N. A., Saxena, S. K., Annersten, H., Halenius, E., Harryson, H., et al. (2000). Stability of ferropericlase in the lower mantle. *Science, 289*(5478), 430–432.

Dubrovinsky, L. S., Dubrovinskaia, N. A., Saxena, S. K., Tutti, F., Rekhi, S., Le Bihan, T., et al. (2001b). Pressure-induced transformation of cristobalite. *Chemical Physics Letters, 333*(3–4), 264–270.

Dubrovinsky, L. S., Saxena, S. K., Lazor, P., Ahuja, R., Eriksson, O., Wills, J. M., et al. (1997). Experimental and theoretical identification of a new high-pressure phase of silica. *Nature, 388,* 362–365.

Duffy, T. S., Hemley, R. J., & Mao, H.-K. (1995). Equation of state and shear strength at multimegabar pressures: Magnesium oxide to 227 GPa. *Physical Review Letters, 74,* 1371–1375.

Dymshits, A. M., Bobrov, A. V., Litasov, K. D., Shatsky, A. F., Ohtani, E., & Litvin, Yu A. (2010). Experimental study of the pyroxene-garnet phase transition in the $Na_2MgSi_5O_{12}$ system at pressures of 13–20 GPa: First syntheses of sodium majorite. *Doklady Earth Sciences, 434*(1), 1263–1266.

Dziewonski, A. M., & Anderson, D. L. (1981). Preliminary reference Earthmodel. *Physics of the Earth and Planetary Interiors, 25,* 297–356.

El Goresy, A., Dera, P., Sharp, T. G., Prewitt, C. T., Chen, M., Dubrovinsky, L., et al. (2008). Seifertite, a dense or-thorhombic polymorph of silica from the Martian meteorites Shergotty and Zagami. *European Journal of Mineralogy, 20,* 523–528.

El Goresy, A., Dubrovinsky, L., Sharp, T. G., Saxena, S. K., & Chen, M. (2000). A monoclinic post-stishovite polymorph of silica in the Shergotty meteorite. *Science, 288*(5471), 1632–1634.

Elsdon, R. (1975). Manganoan ilmenite from the Leinster granite, Ireland. *Mineralogical Magazine, 40*(312), 419–421.

Fei, Y. (1996). *Crystal chemistry of FeO at high pressure and temperature* (pp. 243–254). Geochemical Society Special Publication 5.

Fei, Y., & Bertka, C. M. (1999). Phase transitions in the Earth's mantle and mantle mineralogy. In Y. Fei, C. M. Bertka, & B. O. Mysen (Eds.), *Mantle petrology: Field observations and high pressure experimentation: A tribute to Francis R. (Joe) Boyd* (pp. 189–207). Geochemical Society Special Publication No. 6.

Fei, Y., & Mao, H. K. (1994). In situ determination of the NiAs phase of FeO at high pressure and temperature. *Science, 266*(5191), 1678–1680.

Fei, Y. W., Wang, Y. B., & Finger, L. W. (1996). Maximum solubility of FeO in (Mg, Fe)SiO$_3$ perovskite as a function of temperature at 26 GPa: Implication for FeO content in the lower mantle. *Journal of Geophysical Research, 101,* 11525–11530.

Finger, L. W., & Conrad, P. G. (2000). The crystal structure of "Tetragonal Almandine-Pyrope Phase" (TAPP): A reexamination. *American Mineralogist, 85,* 1804–1807.

Fiquet, G., Dewaele, A., Andrault, D., Kunz, M., & Le Bihan, T. (2000). Thermoelastic properties and crystal structure of MgSiO$_3$ perovskite at lower mantle pressure and temperature conditions. *Geophysical Research Letters, 27,* 21–24.

Fischer, R. A., & Campbell, A. J. (2010). High pressure melting of wüstite. *American Mineralogist, 95,* 1473–1477.

Fischer, R. A., Campbell, A. J., Lord, O. T., Shofner, G. A., Dera, P., & Prakapenka, V. B. (2011a). Phase transition and metallization of FeO at high pressures and temperatures. *Geophysical Research Letters, 38,* L24301. doi:10.1029/2011GL049800

Fischer, R. A., Campbell, A. J., Shofner, G. A., Lord, O. T., Dera, P., & Prakapenka, V. P. (2011b). Equation of state and phase diagram of FeO. *Earth and Planetary Science Letters, 304,* 496–502.

Flynn, G. J., Nittler, L. R., & Engrand, C. (2016). Composition of cosmic dust: Sources and implications for the early Solar system. *Elements, 12*(6), 177–183.

Frost, D. J., Liebske, C., Langenhorst, F., McCammon, C. A., Trønnes, R. G., & Rubie, D. C. (2004). Experimental evidence for the existence of iron-rich metal in the Earth's lower mantle. *Nature, 428,* 409–412.

Frost, D. J., & McCammon, C. A. (2008). The redox state of Earth's mantle. *Annual Review of Earth and Planetary Sciences, 36,* 389–420. doi:10.1146/annurev.earth.36.031207.124322

Frost, D. J., & Myhill, R. (2016). Chemistry of the lower mantle. In H. Terasaki & R. A. Fischer (Eds.), *Deep Earth; Physics and Chemistry of the Lower Mantle and Core: Vol. 217. Geophysical monograph* (pp. 225–240).

Fukui, H., Yoneda, A., Nakatsuka, A., Tsujino, N., Kamada, S., Ohtani, E., et al. (2016). Effect of cation substitution on bridgmanite elasticity: A key to interpret seismic anomalies in the lower mantle. *Scientific Reports, 6,* 33337. doi:10.1038/srep33337

Funamori, N., Jeanloz, R., Miyajima, N., & Fujino, K. (2000). Mineral assemblages of basalt in the lower mantle. *Journal of Geophysical Research, 105*(B11), 26037–26043.

Funamori, N., Jeanloz, R., Nguyen, J. H., Kavner, A., Caldwell, W. A., Fiujino, K., et al. (1998). High-pressure transformations in $MgAl_2O_4$. *Journal of Geophysical Research, 103*(B9), 20813–20818.

Gaspar, J. C., & Wyllie, P. J. (1984). The alleged kimberlite-carbonatite relationship: Evidence from ilmenite and spinel from Premier and Wesselton mines and the Bentfontein sill, South Africa. *Contributions Mineralogy and Petrology, 85*(2), 133–140.

Gasparik, T., Wolf, K., & Smith, C. M. (1994). Experimental determination of phase relations in the $CaSiO_3$ system from 8 to 15 GPa. *American Mineralogist, 79*(11–12), 1219–1222.

Grocholski, B., Shim, S. H., & Prakapenka, V. B. (2013). Stability, metastability, and elastic properties of a dense silica polymorph, seifertite. *Journal of Geophysical Research: Solid Earth, 118*(9), 4745–4757. doi:10.1002/jgrb.50360

Gu, T., Li, M., McCammon, C., & Lee, K. K. M. (2016). Redox-induced lower mantle density contrast and effect on mantle structure and primitive oxygen. *Nature Geoscience, 9,* 723–729. doi:10.1038/NGEO2772

Guyot, F., Madon, M., & Poirier, J.-P. (1988). X-ray microanalysis of high pressure/high temperature phases synthesized from natural olivine in the diamond–anvil cell. *Earth and Planetary Science Letters, 90,* 52–64.

Harris, J. W., Hutchison, M. T., Hursthouse, M., Light, M., & Harte, B. (1997). A new tetragonal silicate mineral occurring as inclusions in lower mantle diamonds. *Nature, 387*(6632), 486–488.

Harte, B. (2010). Diamond formation in the deep mantle: The record of mineral inclusions and their distribution in relation to mantle dehydration zones. *Mineralogical Magazine, 74*(2), 189–215.

Harte, B., & Cayzer, N. (2007). Decompression and unmixing of crystals included in diamonds from the mantle transition zone. *Physics and Chemistry of Minerals, 34,* 647–656.

Harte, B., & Harris, J. W. (1994). Lower mantle mineral association preserved in diamonds. *Mineralogical Magazine, 58A,* 384–385.

Harte, B., Harris, J. W., Hutchison, M. T., Watt, G. R., & Wilding, M. C. (1999). Lower mantle mineral associations in diamonds from Sao Luiz, Brazil. In Y. Fei, C. M. Bertka, & B. O. Mysen (Eds.), *Mantle petrology: Field observations and high pressure experimentation: A tribute to Francis R. (Joe) Boyd* (pp. 125–153). Geochemical Society Special Publication No. 6.

Harte, B., & Hudson, N. F. C. (2013). Mineral associations in diamonds from the lowermost upper mantle and uppermost lower mantle. In *Proceedings of the 10th International Kimberlite Conference* (Vol. 1, pp. 235–254). Special Issue of the Journal of the Geological Society of India.

Hayman, P. C., Kopylova, M. G., & Kaminsky, F. V. (2005). Lower mantle diamonds from Rio Soriso (Juina, Brazil). *Contributions to Mineralogy and Petrology, 149*(4), 430–445. doi:10.1007/s00410-005-0657-8

Hemley, R. J., Prewitt, C. T., & Kingma, K. J. (1994) High-pressure behavior of silica. In P. J. Heaney & C. T. Prewitt (Eds.), *Silica: Physical behavior, geochemistry and materials applications. Reviews in mineralogy* (Vol. 29, pp. 41–82).

Hemley, R. J., Shu, J., Carpenter, M. A., Hu, J., Mao, H. K., & Kingma, K. J. (2000). Strain/order parameter coupling in the ferroelastic transition in dense SiO_2. *Solid State Communications, 114*(10), 527–532.

Hernández, E. R., Alfe, D., & Brodholt, J. (2013). The incorporation of water into lowermantle perovskites: A first-principles study. *Earth and Planetary Science Letters, 364,* 37–43. doi:10.1016/j.epsl.2013.01.005

Hirose, K., Fei, Y. W., Ma, Y. Z., & Mao, H. K. (1999). The fate of subducted basaltic crust in the Earth's lower mantle. *Nature, 397*(6714), 53–56.

Hirose, K., Takafuji, N., Sata, N., & Ohishi, Y. (2005). Phase transition and density of subducted MORB crust in the lower mantle. *Earth and Planetary Science Letters, 237,* 239–251.

Horiuchi, H., Ito, E., & Weidner, D. J. (1987). Perovskite-type $MgSiO_3$: Single-crystal X-ray diffraction. *American Mineralogist, 72,* 357–360.

Hsu, H., Yu, Y. G., & Wentzcovitch, R. M. (2012). Spin crossover of iron in aluminous $MgSiO_3$ perovskite and post-perovskite. *Earth and Planetary Science Letters, 359–360,* 34–39.

Hummer, D. R., & Fei, Y. (2012). Synthesis and crystal chemistry of Fe^{3+}-bearing (Mg, Fe^{3+})(Si, Fe^{3+})O_3 perovskite. *American Mineralogist, 97,* 1915–2012.

Hutchison, M. T. (1997). *Constitution of the deep transition zone and lower mantle shown by diamonds and their inclusions* (Unpublished Ph.D. thesis). University of Edinburgh, UK. Vol. 1, 340 pp., Vol. 2 (Tables and Appendices), 306 pp.

Hutchison, M. T., Hurtshouse, M. B., & Light, M. E. (2001). Mineral inclusions in diamonds: Associations and chemical distinctions around the 670-km discontinuity. *Contributions to Mineralogy and Petrology, 142*(2), 119–126.

Irifune, T. (1994). Absence of an aluminous phase in the upper part of the Earth's lower mantle. *Nature, 370,* 131–133.

Irifune, T., Koizumi, T., & Ando, J. I. (1996). An experimental study of the garnet-perovskite transformation in the system $MgSiO_3$-$Mg_3Al_2Si_3O_{12}$. *Physics of the Earth and Planet Interior, 96*(3–4), 147–157.

Irifune, T., & Ringwood, A. E. (1993). Phase transformations in subducted oceanic crust and buoyancy relationships at depths of 600–800 km in the mantle. *Earth and Planetary Science Letters, 117*(1–2), 101–110.

Irifune, T., Shinmei, T., McCammon, C. A., Miyajima, N., Rubie, D. C., & Frost, D. J. (2010). Iron partitioning and density changes of pyrolite in Earth's lower mantle. *Science, 327*(5962), 193–195. doi:10.1126/science.1181443

Irifune, T., & Tsuchiya, T. (2007). Mineralogy of the Earth—Phase transitions and mineralogy of the lower mantle. In G. D. Price & G. Schubert (Eds.), *Treatise on geophysics. Mineral physicas* (pp. 33–62). Elsevier.

Ishii, T., Hiroshi Kojitani, H., Tsukamoto, S., Fujino, K., Mori, D., Inaguma, Y., et al. (2014). High-pressure phase transitions in $FeCr_2O_4$ and structure analysis of new postspinel $FeCr_2O_4$ and $Fe_2Cr_2O_5$ phases with meteoritical and petrological implications. *American Mineralogist, 99,* 1788–1797.

Ito, E., Akaogi, M., Topor, L., & Navrotsky, A. (1990). Negative pressure-temperature slopes for reactions forming $MgSiO_3$ from calorimetry. *Science, 249,* 1275–1278.

Ito, E., & Matsui, Y. (1978). Synthesis and crystal-chemical characterization of $MgSiO_3$ perovskite. *Earth and Planetary Science Letters, 38,* 443–450.

Ito, E., & Takahashi, E. (1989). Postspinel transformations in the system Mg_2SiO_4-Fe_2SiO_4 and some geophysical implications. *Journal of Geophysical Research, 94*(B8), 10637–10646.

Jackson, I., Khanna, S. K., Revcolevschi, A., & Berthon, J. (1990). Elasticity, shear-mode softening and high-pressure polymorphism of wüstite ($Fe_{1-x}O$). *Journal of Geophysical Research, 95,* 21671–21685.

Jackson, J. M., Sinogeikin, S. V., Jacobsen, S. D., Reichmann, H. J., Mackwell, S. J., & Bass, J. D. (2006). Single-crystal elasticity and sound velocities of ($Mg_{0.94}Fe_{0.06}$)O ferropericlase to 20 GPa. *Journal of Geophysical Research, 111,* B09203.

Jackson, J. M., Zhang, J., & Bass, J. D. (2004). Sound velocities and elasticity of aluminous MgSiO$_3$ perovskite: Implications for aluminum heterogeneity in Earth's lower mantle. *Geophysical Research Letters, 31*(10), L10614.

Jacobsen, S. D., Reichmann, H. J., Spetzler, H., Mackwell, S. J., Smyth, J. R., Angel, R. J., et al. (2002). Structure and elasticity of single-crystal (Mg, Fe)O and a new method of generating shear waves for gigahertz ultrasonic interferometry. *Journal of Geophysical Research, 107,* 5867–5871.

Javoy, M. (1995). The integral enstatite chondrite model of the Earth. *Geophysical Research Letters, 22,* 2219–2222.

Javoy, M., Kaminski, E., Guyot, F., Andrault, D., Sanloup, C., Moreira, M., et al. (2010). The chemical composition of the Earth: Enstatite chondrite models. *Earth and Planetary Science Letters, 293*(3–4), 259–268.

Jeanloz, R., & Ahrens, T. J. (1980). Equations of state of FeO and CaO. *Geophysical Journal of the Royal Astronomical Society, 62,* 505–528.

Jiang, F., Gwanmesia, G. D., Dyuzheva, T. I., & Duffy, T. S. (2009). Elasticity of stishovite and acoustic mode softening under high pressure by Brillouin scattering. *Physics of the Earth and Planetary Interiors, 172*(3–4), 235–240. doi:10.1016/j.pepi.2008.09.017

Joswig, W., Stachel, T., Harris, J. W., Baur, W. H., & Brey, G. P. (1999). New Ca-silicate inclusions in diamonds—Tracers from the lower mantle. *Earth and Planetary Science Letters, 173*(1–2), 1–6.

Jung, D. Y., & Oganov, A. R. (2005). Ab initio study of the high-pressure behavior of CaSiO$_3$ perovskite. *Physics and Chemistry of Minerals, 32,* 146–153. doi:10.1007/s00269-005-0453-z

Kaercher, P., Speziale, S., Miyagi, L., Kanitpanyacharoen, W., & Wenk, H.-R. (2012). Crystallographic preferred orientation in wüstite (FeO) through the cubic-to-rhombohedral phase transition. *Physical Chemistry Minerals, 39,* 613–626. doi:10.1007/s00269-012-0516-x

Kaminski, E., & Javoy, M. (2013). A two-stage scenario for the formation of the Earth's mantle and core. *Earth and Planetary Science Letters, 365,* 97–107.

Kaminski, E., & Javoy, M. (2015). The composition of the Deep Earth. In A. Khan & F. Deschamps (Eds.), *The Earth's heterogeneous mantle* (pp. 303–328). Berlin: Springer.

Kaminsky, F. V. (2012). Mineralogy of the lower mantle: A review of 'super-deep' mineral inclusions in diamond. *Earth-Science Reviews, 110*(1–4), 127–147.

Kaminsky, F. V., & Belousova, E. A. (2009). Manganoan ilmenite as kimberlite/diamond indicator mineral. *Russian Geology and Geophysics, 50*(10), 1212–1220.

Kaminsky, F. V., Khachatryan, G. K., Andreazza, P., Araujo, D., & Griffin, W. L. (2009a). Super-deep diamonds from kimberlites in the Juina area, Mato Grosso State, Brazil. *Lithos, 112S*(2), 833–842.

Kaminsky, F. V., & Lin, J.-F. (2017). Iron partitioning in natural lower-mantle minerals: Toward a chemically heterogeneous lower mantle. *American Mineralogist, 102*(4), 824–832. doi:10.2138/am-2017-5949.

Kaminsky, F. V., Ryabchikov, I. D., McCammon, C., Longo, M., Abakumov, A. M., Turner, S., et al. (2015a). Oxidation potential in the Earth's lower mantle as recorded from ferropericlase inclusions in diamond. *Earth and Planetary Science Letters, 417,* 49–56.

Kaminsky, F. V., Ryabchikov, I. D., & Wirth, R. (2016). A primary natrocarbonatitic association in the Deep Earth. *Mineralogy and Petrology, 110*(2–3), 387–398. doi:10.1007/s00710-015-0368-4

Kaminsky, F., & Wirth, R. (2017). Nitride, carbonitride and nitrocarbide inclusions in lower-mantle diamonds: A key to the balance of nitrogen in the Earth. *European Geosciences Union General Assembly Abstract No. EGU2017-1751*, Vienna, Austria.

Kaminsky, F., Wirth, R., Matsyuk, S., Schreiber, A., & Thomas, R. (2009b). Nyerereite and nahcolite inclusions in diamond: Evidence for lower-mantle carbonatitic magmas. *Mineralogical Magazine, 73*(5), 797–816.

Kaminsky, F. V., Wirth, R., & Schreiber, A. (2015b). A microinclusion of lower-mantle rock and some other lower-mantle inclusions in diamond. *Canadian Mineralogist, 53*(1), 83–104. doi:10.3749/canmin.1400070

Kaminsky, F. V., Zakharchenko, O. D., Channer, D. M. D., Blinova, G. K., & Bulanova, G. P. (1997). Diamonds from the Guaniamo area, Bolivar state, Venezuela. In *Memorias del VIII Congreso Geologico Venezolana, Soc Venezolana de Geologia* (pp. 427–430).

Kaminsky, F. V., Zakharchenko, O. D., Davies, R., Griffin, W. L., Khachatryan-Blinova, G. K., & Shiryaev, A. A. (2001). Superdeep diamonds from the Juina area, Mato Grosso State, Brazil. *Contributions to Mineralogy and Petrology, 140*(6), 734–753.

Kaminsky, F. V., Zakharchenko, O. D., Griffin, W. L., Channer, D. M. D., & Khachatryan-Blinova, G. K. (2000). Diamond from the Guaniamo area, Venezuela. *Canadian Mineralogist, 38*(6), 1347–1370.

Kantor, A. P., Jacobsen, S. D., Kantor, I Yu., Dubrovinsky, L. S., McCammon, C. A., Reichmann, H. J., et al. (2004). Pressure-induced magnetization in FeO: Evidence from elasticity and Mössbauer spectroscopy. *Physical Review Letters, 93,* 215502.

Karki, B., Stixrude, L., & Crain, J. (1997a). Ab initio elasticity of three high-pressure polymorphs of silica. *Geophysical Research Letters, 24*(24), 3269–3272.

Karki, B. B., Warren, M. C., Stixrude, L., Ackland, C. J., & Crain, J. (1997b). *Ab initio* studies of high-pressure structural transformations in silica. *Physical Review B, 55,* 3465–3471.

Karki, B. B., Wentzcovitch, R. M., de Gironcoli, S., & Baroni, S. (2001). First principles thermoelasticity of $MgSiO_3$-perovskite; consequences for the inferred properties of the lower mantle. *Geophysical Research Letters, 28*(14), 2699–2702.

Katsura, T., & Ito, E. (1996). Determination of Fe–Mg partitioning between perovskite and magnesiowüstite. *Geophysical Research Letters, 23*(16), 2005–2008.

Katsura, T., Yoneda, A., Yamazaki, D., Yoshino, T., & Ito, E. (2010). Adiabatic temperature profile in the mantle. *Physics of the Earth and Planetary Interiors, 183,* 212–218. doi:10.1016/j.pepi.2010.07.001

Kesson, S. E., & Fitz Gerald, J. D. (1991). Partitioning of MgO, FeO, NiO, MnO and Cr_2O_3 between magnesian silicate perovskite and magnesiowustite: Implications for the origin of inclusions in diamond and the composition of the lower mantle. *Earth and Planetary Science Letters, 111,* 229–240.

Kesson, S. E., Fitz Gerald, J. D., O'Neill, H., St, C., & Shelley, J. M. G. (2002). Partitioning of iron between magnesian silicate perovskite and magnesiowüstite at about 1 Mbar. *Physics of the Earth and Planetary Interiors, 131,* 295–310.

Kesson, S. E., Fitz Gerald, J. D., & Shelley, J. M. (1998). Mineralogy and dynamics of a pyrolite lower mantle. *Nature, 393*(6682), 252–255.

Kesson, S. E., Fitz Gerald, J. D., Shelley, J. M. G., & Withers, R. L. (1995). Phase relations, structure and crystal chemistry of some aluminous silicate perovskite. *Earth and Planetary Science Letters, 134,* 187–201.

Kind, R., & Li, X. (2007). Deep Earth structure—Transition zone and mantle discontinuities. In G. Schubert, B. Romanowicz, & A. Dziewonski (Eds.), *Treatise on Geophysics: Vol. 1. Seismology and the structure of the Earth* (pp. 591–612). Amsterdam: Elsevier.

Kingma, K. J., Cohen, R. E., Hemley, R. J., & Mao, H.-K. (1995). Transformation of stishovite to a denser phase at lower mantle pressures. *Nature, 374,* 243–245.

Kingma, J. K., Mao, H. K., & Hemley, R. J. (1996). Synchrotron XRD of SiO_2 to multimegabar pressures. *High Pressure Research, 14,* 363.

Klug, D. D., Rousseau, R., Uehara, K., Bernasconi, M., Le Page, Y., & Tse, J. S. (2001). Ab initio molecular dynamics study of the pressure-induced phase transformations in cristobalite. *Physical Review B, 63,* 104106.

Knittle, E., & Jeanloz, R. (1987). Synthesis and equation of state of (Mg, Fe)SiO_3 perovskite to over 100 gigapascals. *Science, 235,* 668–670.

Knittle, E., & Jeanloz, R. (1991). Earth's core-mantle boundary: Results of experiments at high pressures and temperatures. *Science, 251,* 1438–1443.

Kobayashi, Y., Kondo, T., Ohtani, E., Hirao, N., Miyajima, N., Yagi, T., et al. (2005). Fe–Mg partitioning between (Mg, Fe)SiO_3 post-perovskite, perovskite, and magnesiowüstite in the Earth's lower mantle. *Geophysical Research Letters, 32,* L19301. doi:10.1029/2005GL023257

Kojitani, H., Katsura, T., & Akaogi, M. (2007). Aluminum substitution mechanisms in perovskite-type MgSiO$_3$: An investigation by Rietveld analysis. *Physics and Chemistry of Minerals, 34*(4), 257–267. doi:10.1007/s00269-007-0144-z

Komabayashi, T., Hirose, K., Sata, N., Ohishi, Y., & Dubrovinsky, L. S. (2007). Phase transition in CaSiO$_3$ perovskite. *Earth and Planetary Science Letters, 260,* 564–569.

Kondo, T., Ohtani, E., Hirao, N., Yagi, T., & Kikegawa, T. (2004). Phase transitions of (Mg, Fe)O at megabar pressures. *Physics of the Earth and Planetary Interiors, 143–144,* 201–213.

Kubo, T., Suzuki, T., & Akaogi, M. (1997). High pressure phase equilibria in the system CaTiO$_3$–CaSiO$_3$: Stability of perovskite solid solutions. *Physics and Chemistry of Minerals, 24,* 488–494.

Kubo, A., Yagi, T., Ono, S., & Akaogi, M. (2000). Compressibility of Mg$_{0.9}$Al$_{0.2}$Si$_{0.9}$O$_3$ perovskite. *Proceedings of the Japan Academy Series B, 76*(8), 103–107.

Kudoh, Y., Prewitt, C. T., Finger, L. W., Darovskikh, A., & Ito, E. (1990). Effect of iron on the crystal structure of (Mg, Fe)SiO$_3$ perovskite. *Geophysical Research Letters, 17*(10), 1481–1484. doi:10.1029/GL017i010p01481

Kurashina, T., Hirose, K., Ono, S., Sata, N., & Ohishi, Y. (2004). Phase transition in Albearing CaSiO$_3$ perovskite: Implications for seismic discontinuities in the lower mantle. *Physics of the Earth and Planetary Interiors, 145,* 67–74.

Kuwayama, Y., Hirose, K., Satam, N., & Ohishi, Y. (2005). The pyrite-type high-pressure form of silica. *Science, 309,* 923–925.

Lakshtanov, D. L., Sinogeikin, S. V., Konstantin, D., Litasov, K. D., Vitali, B., Prakapenka, V. B., et al. (2007). The post-stishovite phase transition in hydrous alumina-bearing SiO$_2$ in the lower mantle of the Earth. *Proceedings of the National Academy of Sciences of the U.S.A., 104,* 13588–13590.

Lauterbach, S., McCammon, C. A., Aken, P. V., Langenhorst, F., & Seifert, F. (2000). Mossbauer and ELNES spectroscopy of (Mg, Fe)(Si, Al)O$_3$ perovskite: A highly oxidized component of the lower mantle. *Contributions to Mineralogy and Petrology, 138,* 17–26.

Lee, Y. M., & Nassaralla, C. L. (1997). Minimization of hexavalent chromium in magnesite-chrome refractory. *Metallurgical and Materials Transactions B, 28,* 855–859.

Lee, K. K. M., O'Neill, B., Panero, W. R., Shim, S. H., Benedetti, L. R., & Jeanloz, R. (2004). Equations of state of the high-pressure phases of a natural peridotite and implications for the Earth's lower mantle. *Earth and Planetary Science Letters, 223*(3–4), 381–393. doi:10.1016/j.epsl.2004.04.033

Li, L., Nagai, T., Seto, Y., Fujino, K., Kawano, J., & Itoh, S. (2015). Superior solid solubility of MnSiO$_3$ in CaSiO$_3$ perovskite. *Physics and Chemistry of Minerals 42*(2), 123–129.

Li, L., Weidner, D. J., Brodholt, J., Alfe, D., Price, G. D., Caracas, R., et al. (2006). Phase stability of CaSiO$_3$ perovskite at high pressure and temperature: Insights from ab initio molecular dynamics. *Physics of the Earth and Planetary Interiors, 155,* 260–268.

Lin, J.-F., Alp, E. E., Mao, Z., Inoue, T., McCammon, C., Xiao, Y., et al. (2012). Electronic spin states of ferric and ferrous iron in the lower-mantle silicate perovskite. *American Mineralogist, 97,* 592–597.

Lin, J.-F., Heinz, D. L., Mao, H.-K., Hemley, R. J., Devine, J. M., Li, J., et al. (2003). Stability of magnesiowüstite in Earth's lower mantle. *Proceedings of the National Academy of Sciences of the U.S.A., 100*(8), 4405–4408.

Lin, J.-F., Speziale, S., Mao, Z., & Marquardt, H. (2013). Effects of the electronic spin transitions of iron in lower-mantle minerals: Implications to deep-mantle geophysics and geochemistry. *Reviews of Geophysics, 51,* 244–275. doi:10.1002/rog.20010

Lin, J.-F., Struzhkin, V. V., Jacobsen, S. D., Hu, M. Y., Chow, P., King, J., et al. (2005). Spin transition of iron in magnesiowüstite in Earth's lower mantle. *Nature, 436,* 377–380.

Litasov, K. D., Kagi, H., Shatskiy, A., Ohtani, E., Lakshtanov, D. L., Bass, J. D., et al. (2007). High hydrogen solubility in Al-rich stishovite and water transport in the lower mantle. *Earth and Planetary Science Letters, 262,* 620–634. doi:10.1016/j.epsl.2007.08.015

Litasov, K., Ohtani, E., Langenhorst, F., Yurimoto, H., Kubo, H., & Kondo, T. (2003). Water solubility in Mg-perovskites and water storage capacity in the lower mantle. *Earth and Planetary Science Letters, 211,* 189–203.

Litvin, Y. A. (2014). The stishovite paradox in the genesis of superdeep diamonds. *Doklady Earth Sciences, 455*(1), 274–278.

Litvin, Y. A., Spivak, A. V., & Dubrovinsky, L. S. (2016). Magmatic evolution of the material of the Earth's lower mantle: Stishovite paradox and origin of superdeep diamonds (experiments at 24–26 GPa). *Geochemistry International, 54*(11), 936–947. doi:10.1134/S0016702916090032

Liu, L.-G. (1974). Silicate perovskite from phase transformations of pyrope-garnet at high pressure and temperature. *Geophysical Research Letters, 1,* 277–280.

Liu, L.-G. (1975). Post oxide phases of forsterite and enstatite. *Geophysical Research Letters, 2,* 417–419.

Liu, L. (1977). Ilmenite-type solid solutions between $MgSiO_3$ and Al_2O_3 and some structural systematics among ilmenite compounds. *Geochimica et Cosmochimica Acta, 41,* 1355–1361.

Liu, L.-G. (2002). An alternative interpretation of lower mantle mineral associations in diamonds. *Contributions to Mineralogy and Petrology, 144*(1), 16–21.

Liu, Z., Irifune, T., Nishi, M., Tange, Y., Arimoto, T., & Shinmei, T. (2016). Phase relations in the system $MgSiO_3$–Al_2O_3 up to 52 GPa and 2000 K. *Physics of the Earth and Planetary Interiors, 257,* 18–27. doi:10.1016/j.pepi.2016.05.006

Liu, L.-G., & Ringwood, A. E. (1975). Synthesis of a perovskite-type polymorph of $CaSiO_3$. *Earth and Planetary Science Letters, 28,* 209–211.

Lobanov, S. S., Zhu, Q., Holtgrewe, N., Prescher, C., Prakapenka, V. B., Oganov, A. R., et al. (2015). Stable magnesium peroxide at high pressure. *Scientific Review, 5,* 13582. doi:10.1038/srep13582

Longo, M., McCammon, C. A., & Jacobsen, S. D. (2011). Microanalysis of the iron oxidation state in (Mg, Fe)O and application to the study of microscale processes. *Contributions to Mineralogy and Petrology, 162,* 1249–1257.

Magyari-Köpe, B., Vitos, L., Grimvall, G., Johansson, B., & Kollar, J. (2002a). Low-temperature crystal structure of $CaSiO_3$ perovskite: An *ab initio* total energy study. *Physical Review B, 65,* 193107. doi:10.1103/PhysRevB.65.193107

Magyari-Köpe, B., Vitos, L., Johansson, B., & Kollar, J. (2002b). Model structure of perovskites: Cubic-orthorhombic phase transition. *Computational Material Science, 25*(4), 615–621.

Mao, H. K., Chen, L. C., Hemley, R. J., Jephcoat, A. P., Wu, Y., & Bassett, W. A. (1989). Stability and equation of state of $CaSiO_3$-perovskite to 134 GPa. *Journal of Geophysical Research, 94,* 17889–17894.

Mao, Z., Lin, J. F., Scott, H. P., Watson, H. C., Prakapenka, V. B., Xiao, Y., et al. (2011). Iron-rich perovskite in the Earth's lower mantle. *Earth and Planetary Science Letters, 309,* 179–184. doi:10.1016/j.epsl.2011.06.030

Mao, Z., Lin, J.-F., Yang, J., Inoue, T., & Prakapenka, V. B. (2015). Effects of the Fe^{3+} spin transition on the equation of state of bridgmanite. *Geophysical Research Letters, 42,* 4335–4342. doi:10.1002/2015GL064400

Mao, H.-K., Shu, J., Fei, Y., Hu, J., & Hemley, R. J. (1996). The wüstite enigma. *Physics of the Earth and Planetary Interiors, 96,* 135–145.

Mao, W., Shu, J., Hu, J., Hemley, R., & Mao, H.-K. (2002). Displacive transition in magnesiowüstite. *Journal of Physics: Condensed Matter, 14,* 11349–11354.

Mao, Z., Wang, F., Lin, J.-F., Fu, S., Yang, J., Wu, X., et al. (2017). Equation of state of high-spin bridgmanite in the Earth's lower mantle by synchrotron X-ray diffraction and Mössbauer spectroscopy. *American Mineralogist, 102*(2), 357–368. doi:10.2138/am-2017-5770

Marquardt, H., Speziale, S., Reichmann, H. J., Frost, D. J., & Schilling, F. R. (2009a). Single-crystal elasticity of $(Mg_{0.9}Fe_{0.1})O$ to 81 GPa. *Earth and Planetary Science Letters, 287,* 345–352.

Marquardt, H., Speziale, S., Reichmann, H. J., Frost, D. J., Schilling, F. R., & Garnero, E. J. (2009b). Elastic shear anisotropy of ferropericlase in Earth's lower mantle. *Science, 324* (6289), 224–226.

Martirosyan, N.S., Yoshino, T., Shatskiy, A., Chanyshev, A.D., & Litasov, K.D. (2016). The $CaCO_3$–Fe interaction: Kinetic approach for carbonate subduction to the deep Earth's mantle. *Physics of the Earth and Planetary Interiors, 259*, 1–9.

Matas, J., Bass, J. D., Ricard, Y., Mattern, E., & Bukowinsky, M. S. (2007). On the bulk composition of the lower mantle: predictions and limitations from generalized inversion of radial seismic profiles. *Geophysical Journal International, 170,* 764–780.

McCammon, C. A. (1993). Effect of pressure on the composition of the Lower Mantle End Member Fe_xO. *Science, 259,* 66–68.

McCammon, C. A. (1997). Perovskite as a possible sink for ferric iron in the lower mantle. *Nature, 387,* 694–696.

McCammon, C. A. (2005). Mantle oxidation state and oxygen fugacity: Constraints on mantle chemistry, structure, and dynamics. In *Earth's Deep Mantle: Structure, Composition, and Evolution: Vol. 160. Geophysical monograph* (pp. 219–240).

McCammon, C., Hutchison, M. T., & Harris, J. W. (1997). Ferric iron content of mineral inclusions in diamonds from São Luiz: A view into the lower mantle. *Science, 278*(5337), 434–436.

McCammon, C. A., Ringwood, A. E., & Jackson, I. (1983). Thermodynamics of the system Fe-FeO-MgO at high pressure and temperature and a model for formation of the Earth's core. *Geophysical Journal of the Royal Astronomical Society, 72,* 577–595.

McDonough, W. F., & Sun, S.-S. (1995). The composition of the Earth. *Chemical Geology, 120* (3–4), 223–253.

McWilliams, R. S., Spaulding, D. K., Eggert, J. H., Celliers, P. M., Hicks, D. G., Smith, R. F., et al. (2012). Phase transformations and metallization of magnesium oxide at high pressure and temperature. *Science, 338,* 1330–1333.

Meade, C., Mao, H. K., & Hu, J. (1995). High-temperature phase transition and dissociation of (Mg, Fe)SiO_3 perovskite at lower mantle pressures. *Science, 268*(5218), 1743–1745.

Merli, M., Bonadiman, C., Diella, V., & Pavese, A. (2016). Lower mantle hydrogen partitioning between periclase and perovskite: A quantum chemical modelling. *Geochimica et Cosmochimica Acta, 173,* 304–318.

Metsue, A., & Tsuchiya, T. (2011). Lattice dynamics and thermodynamic properties of (Mg, Fe^{2+}) SiO_3 postperovskite. *Journal of Geophysical Research, 116,* JB008018. doi:10.1029/2010JB008018

Meyer, H. O. A., & Svisero, D. P. (1975). Mineral inclusions in Brazilian diamonds. *Physics and Chemistry of the Earth, 9,* 785–795.

Mitchell, R. H. (1978). Manganoan magnesian ilmenite and titanian clinohumite from the Jacupiranga carbonatite, Sao Paulo, Brazil. *American Mineralogist, 63*(5–6), 544–547.

Miyahara, M., Kaneko, S., Ohtani, E., Sakai, T., Nagase, T., Kayama, M., et al. (2013). Discovery of seifertite in a shocked lunar meteorite. *Nature Communications, 4,* 1737. doi:10.1038/ncomms2733

Moore, R. O., & Gurney, J. J. (1985). Pyroxene solid solution in garnets included in diamonds. *Nature, 318*(6046), 553–555.

Moore, R. O., Otter, M. L., Rickard, R. S., Harris, J. W., & Gurney, J. J. (1986). The occurrence of moissanite and ferro-periclase as inclusions in diamond. In *4th International Kimberlite Conference Extended Abstracts, Perth* (Vol. 16, pp. 409–411). Geological Society of Australia Abstracts.

Moran, E., Blesa, M. C., Medina, M.-E., Tornero, J.-D., Menendez, N., & Amador, U. (2002). Nonstoichiometric spinel ferrites obtained from α-$NaFeO_2$ via molten media reactions. *Inorganic Chemistry, 41*(23), 5961–5967.

Muir, J. M. R., & Brodholt, J. P. (2015). Elastic properties of ferrous bearing $MgSiO_3$ and their relevance to ULVZs. *Geophysical Journal International, 201*(1), 496–504. doi:10.1093/gji/ggv045

Muir, J. M. R., & Brodholt, J. P. (2016). Ferrous iron partitioning in the lower mantle. *Physics of the Earth and Planetary Interiors, 257,* 12–17. doi:10.1016/j.pepi.2016.05.008

Murakami, M., Hirose, K., Kawamura, K., Sata, N., & Ohishi, Y. (2004a). Post-perovskite phase transition in MgSiO$_3$. *Science, 304,* 855–858.

Murakami, M., Hirose, K., Ono, S., & Ohishi, Y. (2003). Stability of CaCl$_2$-type and α-PbO$_2$-type SiO$_2$ at high pressure and temperature determined by in situ X-ray measurements. *Geophysical Research Letters, 30,* 1207. doi:10.1029/2002GL016722

Murakami, M., Hirose, K., Ono, S., Tsuchiya, T., Isshiki, M., & Watanuki, T. (2004b). High pressure and high temperature phase transitions of FeO. *Physics of the Earth and Planetary Interiors, 146,* 273–282.

Murakami, M., Hirose, K., Sata, N., & Ohishi, Y. (2005). Post-perovskite phase transition and mineral chemistry in the pyrolitic lowermost mantle. *Geophysical Research Letters, 32,* L03304. doi:10.1029/2004GL021956

Murakami, M., Hirose, K., Yurimoto, H., Nakashima, S., & Takafuji, N. (2002). Water in Earth's Lower Mantle. *Science, 295,* 1885–1887.

Murakami, M., Ohishi, Y., Hirao, N., & Hirose, K. (2012). A perovskitic lower mantle inferred from high-pressure, high-temperature sound velocity data. *Nature, 485*(7396), 90–94. doi:10.1038/nature11004

Nakajima, Y., Frost, D. J., & Rubie, D. C. (2012). Ferrous iron partitioning between magnesium silicate perovskite and ferropericlase and the composition of perovskite in the Earth's lower mantle. *Journal of Geophysical Research, 117,* B08201. doi:10.1029/2012JB009151

Navrotsky, A., Schoenitz, M., Kojitani, H., Xu, H., Zhang, J., Weidner, D. J., et al. (2003). Aluminum in magnesium silicate perovskite: Formation, structure, and energetics of magnesium-rich defect solid solutions. *Journal of Geophysical Research*, *108*(B7). doi:10.1029/2002JB002055

Nestola, F., Burnham, A. D., Peruzza, L., Tauro, L., Alvaro, M., Walter, M. J., et al. (2016a). Tetragonal almandine-pyrope phase, TAPP: Finally a name for it, the new mineral jeffbenite. *Mineralogical Magazine, 80*(7), 1219–1232. doi:10.1180/minmag.2016.080.059

Nestola, F., Burnham, A., Peruzzo, L., Tauro, L., Alvaro, M., Walter, M. J., et al. (2015) Jeffbenite, IMA 2014-097. CNMNC Newsletter No. 24, April 2015, page 250. *Mineralogical Magazine, 79*, 247–251.

Nestola, F., Cerantola, V., Milani, S., Anzolini, C., McCammon, C., Novella, D., et al. (2016b). Synchrotron Mössbauer Source technique for *in situ* measurement of iron-bearing inclusions in natural diamonds. *Lithos, 265,* 328–333. doi:10.1016/j.lithos.2016.06.016

Nomura, R., Hirose, K., Sata, N., & Ohishi, Y. (2010). Precise determination of post-stishovite phase transition boundary and implications for seismic heterogeneities in the mid-lower mantle. *Physics of the Earth and Planetary Interiors, 183,* 104–109. doi:10.1016/j.pepi.2010.08.004

Nomura, R., Ozawa, H., Tateno, S., Hirose, K., Hernlund, H., Muto, S., et al. (2011). Spin crossover and iron-rich silicate melt in the Earth's deep mantle. *Nature, 473,* 199–203.

Oganov, A. R., Brodholt, J. P., & Price, G. D. (2001). Ab initio elasticity and thermal equation of state of MgSiO$_3$ perovskite. *Earth and Planetary Science Letters, 184*(3–4), 555–560.

Oganov, A. R., Gillan, M. J., & Price, G. D. (2005). Structural stability of silica at high pressures and temperatures. *Physical Review B, 71,* 64104.

Oganov, A. R., & Ono, S. (2004). Theoretical and experimental evidence for a post-perovskite phase of MgSiO$_3$ in Earth's D″ layer. *Nature, 430,* 445–448.

Ohta, K., Cohen, R. E., Hirose, K., Haule, K., Shimizu, K., & Ohishi, Y. (2012). Experimental and theoretical evidence for pressure-induced metallization in FeO with rocksalt-type structure. *Physical Review Letters, 108,* 026403. doi:10.1103/PhysRevLett.108.026403

Ohta, K., Fujino, K., Kuwayama, Y., Kondo, T., Shimizu, K., & Ohishi, Y. (2014). Highly conductive iron rich (Mg, Fe)O magnesiowustite and its stability in the Earth's lower mantle. *Journal of Geophysical Research: Solid Earth, 119*(6), 4656–4665.

Ohta, K., Hirose, K., Shimizu, K., & Ohishi, Y. (2010). High-pressure experimental evidence for metal FeO with normal NiAs-type structure. *Physical Review B, 82*(174), 120. doi:10.1103/PhysRevB.82.174120

Ohta. K., Yagi, T., Hirose, K., & OhishI, Y. (2017). Thermal conductivity of ferropericlase in the Earth's lower mantle. *Earth and Planetary Science Letters, 465*, 29–37. doi: 10.1016/j.epsi. 2017.02.030

Omori, K., & Hasegawa, S. (1955). Chemical composition of perthite, ilmenite, allanite and pyroxmangite occurred in pegmatites of vicinity of Iwaizami Town, Iwate Prefecture. *Journal of Japanese Association of Mineralogy, Petrography, and Economic Geology, 39,* 89–98.

Ono, S., Hirose, K., Murakami, M., & Isshiki, M. (2002). Post-stishovite phase boundary in SiO_2 determined by in situ X-ray observations. *Earth and Planetary Science Letters, 197,* 187–192.

Ono, S., Ohishi, Y., Isshiki, M., & Watanuki, T. (2005). In situ X-ray observations of phase assemblages in peridotite and basalt compositions at lower mantle conditions: Implications for density of subducted oceanic plate. *Journal of Geophysical Research, 110,* B02208.

Ono, S., Ohishi, Y., & Mibe, K. (2004). Phase transition in CaSi-perovskite and stability of Al-bearing Mg-perovskite in the lower mantle. *American Mineralogist, 89,* 1480–1485.

Ozawa, H., Hirose, K., Ohta, K., Ishii, H., Hiraoka, N., Ohishi, Y., et al. (2011). Spin crossover, structural change, and metallization in NiAs-type FeO at high pressure. *Physical Review B, 84,* 134417.

Ozawa, H., Hirose, K., Tateno, S., Sata, N., & Ohishi, Y. (2010). Phase transition boundary between B1 and B8 structures of FeO up to 210 GPa. *Physics of the Earth and Planetary Interiors, 179,* 157–163.

Ozawa, H., Hirose, K., Yonemitsu, K., & Ohishi, Y. (2016). High-pressure melting experiments on Fe–Si alloys and implications for silicon as a light element in the core. *Earth and Planetary Science Letters, 456,* 47–54. doi:10.1016/j.epsl.2016.08.042

Palot, M., Jacobsen, S. D., Townsend, J. P., Nestola, F., Marquardt, K., Harris, J. W., et al. (2016). Evidence for H_2O-bearing fluids in the lower mantle from diamond inclusion. *Lithos, 265,* 237–243. doi:10.1016/j.lithos.2016.06.023

Panero, W. R., & Stixrude, L. P. (2004). Hydrogen incorporation in stishovite at high pressure and symmetric bonding in δ-AlOOH. *Earth and Planetary Science Letters, 221,* 421–431.

Park, K. T., Terakura, K., & Matsui, Y. (1988). Theoretical evidence for a new ultra-high-pressure phase of SiO_2. *Nature, 336,* 670–672. doi:10.1038/336670a0

Perrillat, J. P., Ricolleau, A., Daniel, I., Fiquet, G., Mezouar, M., Guignot, N., et al. (2006). Phase transformations of subducted basaltic crust in the upmost lower mantle. *Physics of the Earth and Planetary Interiors, 157*(1–2), 139–149.

Perry, S.N., Pigott, J.S., & Panero, W.R. (2017). Ab initio calculations of uranium and thorium storage in $CaSiO_3$-perovskite in the Earth's lower mantle. *American Mineralogist*, *102*, 321–326. doi: 10.2138/am-2017-5816

Reid, A. F., & Ringwood, A. E. (1969). Newly observed high pressure transformations in Mn_3O_4, $CaAl_2O_4$, and $ZrSiO_4$. *Earth and Planetary Science Letters, 6,* 205–208.

Reid, A.F., & Ringwood, A.E. (1970). The crystal chemistry of dense M_3O_4 polymorphs: High pressure Ca_2GeO_4 of K_2NiF_4 structure type. *Journal of Solid State Chemistry, 1*, 557–565.

Reid, A. F., & Ringwood, A. E. (1975). High pressure modification of $ScAlO_3$ and some geophysical implications. *Journal of Geophysical Research, 80,* 3363–3369.

Richet, P., Mao, H.-K., & Bell, P. M. (1989). Bulk moduli of magnesiowiistites from static compression measurements. *Journal of Geophysical Research, 94*(B3), 3037–3045.

Richmond, N. C., & Brodholt, J. P. (1998). Calculated role of aluminum in the incorporation of ferric iron into magnesium silicate perovskite. *American Mineralogist, 83,* 947–951.

Ricolleau, A., Fiquet, G., Addad, A., Menguy, N., Vanni, C., Perrillat, J.-P., et al. (2008). Analytical transmission electron microscopy study of a natural MORB sample assemblage transformed at high pressure and high temperature. *American Mineralogist, 93,* 144–153. doi:10.2138/am.2008.2532

Righter, K., Danielson, L., Drake, M. J., & Domanik, K. (2014). Partition coefficients at high pressure and temperature. In R. W. Carlson (Ed.), *Treatise on geochemistry* (2nd ed., Vol. 3, pp. 449–477). Elsevier.

Ringwood, A. E. (1962). Mineralogical constitution of the deep mantle. *Journal of Geophysical Research, 67*(10), 4005–4010.

Ringwood, A. E. (1975). *Composition and petrology of the Earth's mantle* (p. 618). New York: McGraw-Hill.

Ringwood, A. E. (1977). Composition of core and implications for origin of Earth. *Geochemical Journal, 11*(3), 111–135.

Róg, G., Kozlowska-Róg, A., & Dudek, M. (2007). The standard Gibbs free energy of formation of calcium chromium (III) oxide in the temperature range (1073 to 1273 K). *The Journal of Chemical Thermodynamics, 39,* 275–278.

Ross, N. L., Angel, R. J., & Seifert, F. (2002). Compressibility of brownmillerite ($Ca_2Fe_2O_5$): Effect of vacancies on the elastic properties of perovskite. *Physics of the Earth and Planetary Interiors, 129,* 145–151.

Ryabchikov, I. D. (2011). Conditions of diamond formation in the Earth's lower mantle. *Doklady Earth Sciences, 438*(2), 788–791.

Ryabchikov, I. D., & Kaminsky, F. V. (2013a). The composition of the lower mantle: Evidence from mineral inclusions in diamonds. *Doklady Earth Sciences, 453*(2), 1246–1249.

Ryabchikov, I. D., & Kaminsky, F. V. (2013b). Oxygen potential of diamond formation in the lower mantle. *Geology of Ore Deposits, 55*(1), 1–12. doi:10.1134/S1075701513010066

Ryabchikov, I. D., & Kaminsky, F. V. (2014). Physico-chemical parameters of material in mantle plumes: Evidence from the thermodynamic analysis of mineral inclusions in sublithospheric diamonds. *Geochemistry International, 52*(11), 903–911. doi:10.1134/S001670291411007X

Sakai, T., Ohtani, E., Terasaki, H., Sawada, N., Kobayashi, Y., Miyahara, M., et al. (2009). Fe–Mg partitioning between perovskite and ferropericlase in the lower mantle. *American Mineralogist, 94,* 921–925. doi:10.2138/am.2009.3123

Saxena, S. K., Dubrovinsky, L. S., Lazor, P., Cerenius, Y., Haggkvist, P., Hanfland, M., et al. (1996). Stability of perovskite ($MgSiO_3$) in the Earth's mantle. *Science, 274*(5291), 1357–1359.

Saxena, S. K., Dubrovinsky, L. S., Lazor, P., & Hu, J. Z. (1998). In situ X-ray study of perovskite ($MgSiO_3$): Phase transition and dissociation at mantle conditions. *European Journal of Mineralogy, 10,* 1275–1281.

Scott Smith, B. H., Danchin, R. V., Harris, J. W., & Stracke, K. J. (1984). Kimberlites near Orroroo, South Australia. In J. Kornprobst (Ed.), *Kimberlites I: Kimberlites and related rocks* (pp. 121–142). Amsterdam: Elsevier.

Seagle, C. T., Heinz, D. L., Campbell, A. J., Prakapenka, V. B., & Wanless, S. T. (2008). Melting and thermal expansion in the Fe–FeO system at high pressure. *Earth and Planetary Science Letters, 265,* 655–665.

Serghiou, G., Zerr, A., & Boehler, R. (1998). (Mg, Fe)SiO_3-perovskite stability under lower mantle conditions. *Science, 280*(5372), 2093–2095.

Shannon, R. D., & Prewitt, C. T. (1969). Effective ionic radii in oxides and fluorides. *Acta Crystallographica, B25,* 925–946.

Sharp, T. G., El Goresy, A., Wopenka, B., & Chen, M. (1999). A post-stishovite SiO_2 polymorph in the meteorite Shergotty: Implications for impact events. *Science, 284,* 1511–1513.

Sharygin, I. S., Litasov, K. D., Shatskiy, A., Safonov, O. G., Ohtani, E., & Pokhilenko, N. P. (2012) Interaction of orthopyroxene with carbonatite melts at 3 and 6.5 GPa: Implication for evolution of kimberlite magma. In *G–COE Symposium 2012. Achievement of G–COE Program for Earth and Planetary Science, Sendai, Japan, 2012* (pp. 146–149).

Sherman, D. M. (1989). The nature of pressure-induced metallization of FeO and its implications to the core-mantle boundary. *Geophysical Research Letters, 16,* 515–518.

Sherman, D. M., & Jansen, H. J. F. (1995). First-principles predictions of the high pressure phase transition and electronic structure of FeO: Implications for the chemistry of the lower mantle and core. *Geophysical Research Letters, 22,* 1001–1004.

Shieh, S. R., Duffy, T. S., & Shen, G. (2005). XRD study of phase stability in SiO_2 at deep mantle conditions. *Earth and Planetary Science Letters, 235,* 273–282.

Shim, S.-H., Duffy, T. S., & Shen, G. (2000a). The stability and P–V–T equation of state of $CaSiO_3$ perovskite in the Earth's lower mantle. *Journal of Geophysical Research, 106*(B11), 25955–25968.

Shim, S. H., Duffy, T., & Shen, G. (2000b). The equation of state of $CaSiO_3$ perovskite to 108 GPa at 300 K. *Physics of the Earth and Planetary Interiors, 120,* 327–338.

Shim, S. H., Duffy, T. S., & Shen, G. (2001). Stability and structure of $MgSiO_3$ perovskite to 2300-kilometer depth in Earth's mantle. *Science, 293*(5539), 2437–2440.

Shim, S.-H., Jeanloz, R., & Duffy, T. S. (2002). Tetragonal structure of $CaSiO_3$ perovskite above 20 GPa. *Geophysical Research Letters, 29*(24), 2466. doi:10.1029/2002GL016148

Shu, J., Mao, H. K., Hu, J., Fei, Y., & Hemley, R. J. (1998). Single-crystal XRD of wüstite to 30 GPa hydrostatic pressure. *Neues Jahrbuch für Mineralogie Abhandlungen, 172,* 309–323.

Shukla, G., Wu, Z., Hsu, H., Floris, A., Cococcioni, M., & Wentzcovitch, R. M. (2015). Thermoelasticity of Fe^{2+}-bearing bridgmanite. *Geophysical Research Letters, 42,* 1741–1749.

Sidorin, I., Michael, G., & Helmberger, D. V. (1999). Evidence for a ubiquitous seismic discontinuity at the base of the mantle. *Science, 286,* 1326–1331.

Simpson, E. S. (1929). Contributions to the mineralogy of Western Australia. *Journal of the Royal Society of Western Australia, 15,* 99–113.

Sinmyo, R., Bykova, E., McCammon, C., Kupenko, I., Potapkin, V., & Dubrovinsky, L. (2014). Crystal chemistry of Fe^{3+}-bearing (Mg, Fe)SiO_3 perovskite: a single-crystal X-ray diffraction study. *Physics and Chemistry of Minerals, 41,* 409–417.

Sinmyo, R., & Hirose, K. (2013). Iron partitioning in pyrolitic lower mantle. *Physics and Chemistry of Minerals, 40,* 107–113. doi:10.1007/s00269-012-0551-7

Sinogeikin, S. V., Zhang, J., & Bass, J. D. (2004). Elasticity of single crystal and polycrystalline $MgSiO_3$ perovskite by Brillouin spectroscopy. *Geophysical Research Letters, 31,* L06620. doi:10.1029/2004GL019559

Snetsinger, K. G. (1969). Manganoan ilmenite from a Sierran adamellite. *American Mineralogist, 54*(4), 431–435.

Sobolev, N. V., Yefimova, E. S., Channer, D. M. D., Anderson, P. F. N., & Barron, K. M. (1998). Unusual upper mantle beneath Guaniamo, Guyana shield, Venezuela: Evidence from diamond inclusions. *Geology, 26*(11), 971–974.

Speziale, S., Milner, A., Lee, V. E., Clark, S. M., Pasternak, M. P., & Jeanloz, R. (2005). Iron spin transition in Earth's mantle. *Proceedings of the National Academy of the U.S.A., 102,* 17918–17922. doi:10.1073/pnas.0508919102

Stachel, T., Harris, J. W., Brey, G. P., & Joswig, W. (2000). Kankan diamonds (Guinea) II: Lower mantle inclusion parageneses. *Contributions to Mineralogy and Petrology, 140*(1), 16–27.

Stebbins, J. F., Kroeker, S., & Andrault, D. (2001). The mechanism of solution of aluminum oxide in $MgSiO_3$ perovskite. *Geophysical Research Letters, 28,* 615–618.

Stishov, S. M., & Belov, N. V. (1962). Crystal structure of a new dense modification of silica SiO_2. *Doklady Akademii Nauk SSSR, 143*(4), 951.

Stishov, S. M., & Popova, S. V. (1961). A new dense modification of silica. *Geochemistry (USSR), 10,* 923–926.

Stixrude, L., & Cohen, R. E. (1993). Stability of orthorhombic $MgSiO_3$ perovskite in the Earth's lower mantle. *Nature, 364*(6438), 613–616.

Stixrude, L., Cohen, R. E., Yu, R., & Krakauer, H. (1996). Prediction of phase transition in $CaSiO_3$ perovskite and implications for lower mantle structure. *American Mineralogist, 81,* 1293–1296.

Stixrude, L., Lithgow-Bertelloni, C., Kiefer, B., & Fumagalli, P. (2007). Phase stability and shear softening in $CaSiO_3$ perovskite at high pressure. *Physical Review B, 75,* 024108.

Sugahara, M., Yoshiasa, A., Komatsu, Y., Yamanaka, T., Bolfan-Kasanova, N., Nakatsuka, A., et al. (2006). Reinvestigation of the $MgSiO_3$ perovskite structure at high pressure. *American Mineralogist, 91,* 533–536.

Sun, N., Mao, Z., Yan, S., Lin, J. F., Wu, X., & Prakapenka, V. B. (2016). Confirming a pyrolitic lower mantle using self-consistent pressure scales and new constraints on $CaSiO_3$-perovskite. *Journal of Geophysical Research, 121*(7), 4876–4892. doi:10.1002/2016JB013062

Takafuji, N., Yagi, T., Miyajima, N., & Sumita, T. (2002). Study on Al_2O_3 content and phase stability of aluminous-$CaSiO_3$ perovskite at high pressure and temperature. *Physics and Chemistry of Minerals, 29,* 532–537. doi:10.1007/s00269-002-0271-5

Tange, Y., Takahashi, E., Nishihara, Y., Funakoshi, K., & Sata, N. (2009). Phase relations in the system MgO-FeO-SiO$_2$ to 50 GPa and 2000°C: An application of experimental techniques using multianvil apparatus with sintered diamond anvils. *Journal of Geophysical Research, 114*(B02), 214.

Tappert, R., Foden, J., Stachel, T., Muehlenbachs, K., Tappert, M., & Wills, K. (2009a). The diamonds of South Australia. *Lithos, 112S,* 806–821.

Tappert, R., Foden, J., Stachel, T., Muehlenbachs, K., Tappert, M., & Wills, K. (2009b). Deep mantle diamonds from South Australia: A record of Pacific subduction at the Gondwanan margin. *Geology, 37*(1), 43–46. doi:10.1130/G25055A.1

Tappert, R., Stachel, T., Harris, J. W., Muehlenbachs, K., Ludwig, T., & Brey, G. (2005a). Diamonds from Jagersfontein (South Africa): Messengers from the sublithospheric mantle. *Contributions to Mineralogy and Petrology, 150*(5), 505–522.

Tappert, R., Stachel, T., Harris, J. W., Shimizu, N., & Brey, G. P. (2005b). Mineral inclusions in diamonds from the Slave Province, Canada. *European Journal of Mineralogy, 17*(3), 423–440.

Tarrida, M., & Richet, P. (1989). Equation of state of CaSiO$_3$ perovskite to 96 GPa. *Geophysical Research Letters, 16,* 1351–1354.

Tateno, S., Hirose, K., & Ohishi, Y. (2014). Melting experiments on peridotite to lowermost mantle conditions. *Journal of Geophysical Research: Solid Earth, 119,* 4684–4694. doi:10.1002/2013JB010616

Teter, D. M., Hemley, R. J., Kresse, G., & Hafner, J. (1998). High-pressure polymorphism in silica. *Physical Review Letters, 80,* 2145–2148.

Thomson, A. R., Kohn, S. C., Bulanova, G. P., Smith, C. B., Araujo, D., & Walter, M. J. (2014). Origin of sub-lithospheric diamonds from the Juina-5 kimberlite (Brazil): Constraints from carbon isotopes and inclusion compositions. *Contributions to Mineralogy and Petrology, 168,* 1081.

Thomson, A. R., Kohn, S. C., Bulanova, G. P., Smith, C. B., Araujo, D., & Walter, M. J. (2016). Trace element composition of silicate inclusions in sub-lithospheric diamonds from the Juina-5 kimberlite: Evidence for diamond growth from slab melts. *Lithos, 265,* 108–124. doi:10.1016/j.lithos.2016.08.035

Tomioka, N., & Fujino, K. (1997). Natural (Mg, Fe)SiO$_3$-ilmenite and perovskite in the Tenham meteorite. *Science, 277,* 1084–1086.

Tomioka, N., & Fujino, K. (1999). Akimotoite, (Mg, Fe)SiO$_3$, a new silicate mineral of the ilmenite group in the Tenham chondrite. *American Mineralogist, 84,* 267–271.

Townsend, J. P., Tsuchiya, J., Bina, C. R., & Jacobsen, S. D. (2016). Water partitioning between bridgmanite and postperovskite in the lowermost mantle. *Earth and Planetary Science Letters, 454,* 20–27. doi:10.1016/j.epsl.2016.08.009

Tschauner, O., Ma, Ch., Beckett, J. R., Prescher, C., Prakapenka, V. B., & Rossman, G. R. (2014). Discovery of bridgmanite, the most abundant mineral in Earth, in a shocked meteorite. *Science, 346*(6213), 1100–1102.

Tsuchida, Y., & Yagi, T. (1989). A new, post-stishovite high-pressure polymorph of silica. *Nature, 340,* 217–220.

Tsuchiya, T., & Kawai, K. (2013). Ab initio mineralogical model of the Earth's lower mantle. In: S.-i. Karato (Ed.), *Physics and Chemistry of the Deep Earth*. John Wiley, Sons, pp. 213–243.

Tsuchiya, T., Caracas, R., & Tsuchiya, J. (2004a). First principles determination of the phase boundaries of high-pressure polymorphs of silica. *Geophysical Research Letters, 31,* L11610. doi:10.1029/2004GL019649

Tsuchiya, T., Tsuchiya, J., Umemoto, K., & Wentzcovitch, R. M. (2004b). Phase transition in MgSiO$_3$ perovskite in the earth's lower mantle. *Earth and Planetary Science Letters, 224,* 241–248.

Tsuchiya, T., & Wang, X. (2013). Ab initio investigation on the high-temperature thermodynamic properties of Fe^{3+}-bearing MgSiO$_3$ perovskite. *Journal of Geophysical Research, 118,* 83–91. doi:10.1029/2012JB009696

Umemoto, K., Kawamura, K., Hirose, K., & Wentzcovitch, R. M. (2016). Post-stishovite transition in hydrous aluminous SiO_2. *Physics of the Earth and Planetary Interiors, 255,* 18–26. doi:10.1016/j.pepi.2016.03.008

Van Aken, P. A., & Liebscher, B. (2002). Quantification of ferrous/ferric ratios in minerals: New evaluation schemes of Fe L_{23} electron energy-loss near-edge spectra. *Physics and Chemistry of Minerals, 29*(3), 188–200.

Van Rythoven, A. D., & Schulze, D. J. (2009). In-situ analysis of diamonds and their inclusions from the Diavik Mine, Northwest Territories, Canada: Mapping diamond growth. *Lithos, 112S,* 870–879.

Vanpeteghem, C., Angel, R., Ross, N., Jacobsen, S., Dobson, D., Litasov, K., et al. (2006). Al, Fe substitution in the $MgSiO_3$ perovskite structure: A single-crystal X-ray diffraction study. *Physics of the Earth and Planetary Interiors, 155*(1–2), 96–103.

Vilella, K., Shim, S.-H., Farnetani, C. G., & Badro, J. (2015). Spin state transition and partitioning of iron: Effects on mantle dynamics. *Earth and Planetary Science Letters, 417,* 57–66. doi:10.1016/j.epsl.2015.02.009

Vincent, E. A., & Phillips, R. (1954). Iron-titanium oxide minerals in layered gabbros of the Skaergaard intrusion, East Greenland. *Geochimica et Cosmochimica Acta, 6*(1), 1–34.

Wadhawan, V. K. (1982). Ferroelasticitay and related properties of crystals. *Phase Transitions, 3,* 3–103.

Walter, M. J., Kubo, A., Yoshino, T., Brodholt, J., Koga, K. T., & Ohishi, Y. (2004a). Phase relations and equation-of-state of aluminous Mg-silicate perovskite and implications for Earth's lower mantle. *Earth and Planetary Science Letters, 222*(2), 501–516.

Walter, M. J., Nakamura, E., Tronnes, R. G., & Frost, D. J. (2004b). Experimental constraints on crystallization differentiation in a deep magma ocean. *Geochimica et Cosmochimica Acta, 68,* 4267–4284.

Wang, W., Gasparik, T., & Rapp, R. (2000). Partitioning of rare earth elements between $CaSiO_3$ perovskite and coexisting phases: Constraints on the formation of $CaSiO_3$ inclusions in diamond. *Earth and Planetary Science Letters, 181*(3), 291–300.

Wang, Y. B., & Weidner, D. J. (1994). Thermoelasticity of $CaSiO_3$ perovskite and implications for the lower mantle. *Geophysical Research Letters, 21,* 895–898.

Warren, M. C., Ackland, G. J., Karki, B. B., & Clark, S. J. (1998). Phase transitions in silicate perovskites from first principles. *Mineralogical Magazine, 62*(5), 585–598.

Wentzcovitch, R. M., Ross, N. L., & Price, G. D. (1995). Ab initio study of $MgSiO_3$ and $CaSiO_3$ perovskites at lower-mantle pressures. *Physics of the Earth and Planetary Interiors, 90,* 101–112.

Wicks, J. K., & Duffy, T. S. (2016). Crystal structures of minerals in the lower mantle. In H. Terasaki & R. A. Fischer (Eds.), *Deep Earth: Physics and Chemistry of the Lower Mantle and Core: Vol. 217. Geophysical monograph* (pp. 69–87).

Wicks, J. K., Jackson, J. M., Sturhahn, W., Zhuravlev, K. K., Tkachev, S. N., & Prakapenka, V. B. (2015). Thermal equation of state and stability of $(Mg_{0.06}Fe_{0.94})O$. *Physics of the Earth and Planetary Interiors, 249,* 28–42.

Wilding, M. C. (1990). *A study of diamonds with syngenetic inclusions* (Unpublished Ph.D. thesis). University of Edinburgh, UK, 281 pp.

Wilding, M. C., Harte, B., & Harris, J. W. (1991). Evidence for a deep origin for the Sao Luiz diamonds. In *Fifth International Kimberlite Conference Extended Abstracts, Araxa, June 1991,* pp. 456–458.

Williams, Q., & Knittle, E. (2005). The highly uncertain bulk composition of Earth's mantle. In R. van der Hilst, J. Trampert, J. Bass, & J. Matas (Eds.), *Structure, dynamics and properties of Earth's Mantle* (pp. 187–200). Washington, D.C.: AGU Press.

Wirth, R., Dobrzhinetskaya, L., Harte, B., Schreiber, A., & Green, H. W. (2014). High-Fe (Mg, Fe)O inclusion in diamond apparently from the lowermost mantle. *Earth and Planetary Science Letters, 404,* 365–376.

Wirth, R., Vollmer, C., Brenker, F., Matsyuk, S., & Kaminsky, F. (2007). Nanocrystalline hydrous aluminium silicate in superdeep diamonds from Juina (Mato Grosso State, Brazil). *Earth and Planetary Science Letters, 259*(3–4), 384–399.

Wolf, G. H., & Jeanloz, R. (1985). Lattice dynamics and structural distortions of $CaSiO_3$ and $MgSiO_3$ perovskites. *Geophysical Research Letters, 12*(7), 413–416.

Wood, B. J. (2000). Phase transformations and partitioning relations in peridotite under lower mantle conditions. *Earth and Planetary Science Letters, 174*(3–4), 341–354.

Wood, B. J., & Corgne, A. (2009). Mineralogy of the Earth—Trace elements and hydrogen in the Earth's transition zone and lower mantle. In G. D. Price (Ed.), *Treatise on geophysics. Mineral physics* (pp. 63–89.). Elesevier.

Wu, Z., João, F., Justo, F., & Wentzcovitch, R. M. (2013). Elastic anomalies in a spin-crossover system: Ferropericlase at lower mantle conditions. *Physical Review Letters, 110,* 228501.

Wu, Z., & Wentzcovitch, R. M. (2014). Spin crossover in ferropericlase and velocity heterogeneities in the lower mantle. *Proceedings of the National Academy of the U.S.A., 111,* 10468–10472.

Xu, S., Lin, J.-F., Morgan, D. (2017). Iron speciation induced chemical and seismic heterogeneities in the lower mantle. *Journal of Geophysical Research. Solid Earth*, *122*. doi: 10.1002/2016JB013543.

Xu, Y., McCammon, C., & Poe, B. T. (1998). The effect of alumina on the electrical conductivity of silicate perovskite. *Science, 282,* 922–924.

Xu, S., Shim, S.-H., & Morgan, D. (2015). Origin of Fe^{3+} in Fe-containing, Al-free mantle silicate perovskite. *Earth and Planetary Science Letters, 409,* 319–328.

Yagi, T., Okabe, K., Nishiyama, N., Kubo, A., & Kikegawa, T. (2004). Complicated effects of aluminum on the compressibility of silicate perovskite. *Physics of the Earth and Planetary Interiors, 143–144,* 81–91.

Yagi, T., Suzuki, T., & Akimoto, S. (1985). Static compression of wüstite ($Fe_{0.98}$)O to 120 GPa. *Journal of Geophysical Research, 90,* 8784–8788.

Yamamoto, T., Yuen, D. A., & Ebisuzaki, T. (2003). Substitution mechanism of Al ions in $MgSiO_3$ perovskite under high pressure conditions from first-principles calculations. *Earth and Planetary Science Letters, 206,* 617–625.

Yamanaka, T., Fukuda, T., & Tsuchiya, J. (2002). Bonding character of SiO_2 stishovite under high pressures up to 30 GPa. *Physics and Chemistry of Minerals, 29,* 633–641. doi:10.1007/s00269-002-0257-3

Yamanaka, T., Uchida, A., & Nakamoto, Y. (2008). Structural transition of post-spinel phases $CaMn_2O_4$, $CaFe_2O_4$, and $CaTi_2O_4$ under high pressures up to 80 GPa. *American Mineralogist, 93,* 1874–1881. doi:10.2138/am.2008.2934

Yamazaki, D., Ito, E., Yoshino, T., Tsujino, N., Yoneda, A., Guo, X., et al. (2014). Over 1 Mbar generation in the Kawai-type multianvil apparatus and its application to compression of ($Mg_{0.92}Fe_{0.08}$)SiO_3 perovskite and stishovite. *Physics of the Earth and Planetary Interiors, 228,* 262–267. doi:10.1016/j.pepi.2014.01.013

Yang, J., Tong, X., Lin, J.-F., Okuchi, T., & Tomioka, N. (2015). Elasticity of ferropericlase across the spin crossover in the Earth's lower mantle. *Scientific Reports, 5,* 17188. doi:10.1038/srep17188

Yeganeh-Haeri, A., Weidner, D. J., & Ito, E. (1989). Elasticity of $MgSiO_3$ in the perovskite structure. *Science, 243,* 787–789.

Yoshino, T., Kamada, S., Zhao, C., Ohtani, E., & Naohisa, H. (2016). Electrical conductivity model of Al-bearing bridgmanite with implications for the electrical structure of the Earth's lower mantle. *Earth and Planetary Science Letters, 434,* 208–219.

Yu, Y. G., Wentzcovitch, R. M., Vinograd, V. L., & Angel, R. J. (2011). Thermodynamic properties of $MgSiO_3$ majorite and phase transitions near 660 km depth in $MgSiO_3$ and Mg_2SiO_4: A first principles study. *Journal of Geophysical Research, 116,* B02208. doi:10.1029/2010JB007912

Zedgenizov, D. A., Kagi, H., Shatsky, V. S., & Ragozin, A. L. (2014a). Local variations of carbon isotope composition in diamonds from Sao-Luis (Brazil): Evidence for heterogenous carbon reservoir in sublithospheric mantle. *Chemical Geology, 240*(1–2), 114–124. doi:10.1016/j. chemgeo.2013.10.033

Zedgenizov, D. A., Ragozin, A. L., Kalininaa, V. V., & Kagi, H. (2016). The mineralogy of Ca-rich inclusions in sublithospheric diamonds. *Geochemistry International, 54*(10), 890–900. doi:10.1134/S0016702916100116

Zedgenizov, D. A., Shatskiy, A., Ragozin, A. L., Kagi, H., & Shatsky, V. S. (2014b). Merwinite in diamond from São Luiz, Brazil: A new mineral of the Ca-rich mantle environment. *American Mineralogist, 99,* 547–550.

Zedgenizov, D. A., Shatsky, V. S., Panin, A. V., Evtushenko, O. V., Ragozin, A. L., & Kagi, H. (2015). Evidence for phase transitions in mineral inclusions in superdeep diamonds of the Sao Luiz deposit, Brazil. *Russian Geology and Geophysics, 56*(1), 296–305.

Zerr, A., Serghiou, G., & Boehler, R. (1997). Melting of $CaSiO_3$ perovskite to 430 kbar and first in situ measurements of lower mantle eutectic temperatures. *Geophysical Research Letters, 12* (24), 909–912.

Zhai, S., Yin, Y., Shieh, S. R., Shan, S., Xue, W., Wang, C.-P., et al. (2016). High-pressure X-ray diffraction and Raman spectroscopy of $CaFe_2O_4$-type β-$CaCr_2O_4$. *Physics and Chemistry of Minerals, 43,* 307–314. doi:10.1007/s00269-015-0795-0

Zhang, S., Cottaar, S., Liu, T., Stackhouse, S., & Militzera, B. (2016a). High-pressure, temperature elasticity of Fe-and Al-bearing $MgSiO_3$: Implications for the Earth's lower mantle. *Earth and Planetary Science Letters, 434,* 264–273.

Zhang, J., Li, B., Utsumi, W., & Liebermann, R. C. (1996). In situ X-ray observations of the coesite-stishovite transition: Reversed phase boundary and kinetics. *Physics and Chemistry of Minerals, 23,* 1–10.

Zhang, L., Meng, Y., Yang, W., Wang, L., Mao, W. L., Zeng, Q. S., et al. (2014). Disproportionation of (Mg, Fe)SiO_3 perovskite in Earth's deep lower mantle. *Science, 344* (6186), 877–882. doi:10.1126/science.1250274

Zhang, L., Popov, D., Meng, Y., Wang, J., Ji, C., Li, B., et al. (2016b). In situ crystal structure determination of seifertite SiO_2 at 129 GPa: Studying a minor phase near Earth's core–mantle boundary. *American Mineralogist, 101,* 231–234.

Zhang, J., & Weidner, D. J. (1999). Thermal equation of state of aluminum-enriched silicate perovskite. *Science, 284,* 782–784.

Zhang, J., & Zhao, Y. (2005). Effects of defect and pressure on the thermal expansivity of Fe_XO. *Physics and Chemistry of Minerals, 32,* 241–247.

Zhu, Q., Oganov, A. R., & Lyakhov, A. O. (2013). Novel stable compounds in the Mg–O system under high pressure. *Physical Chemistry Chemical Physics, 15,* 7696–7700.

Zou, G. T., Mao, H. K., Bell, P. M., & Virgo, D. (1980). High-pressure experiments on the iron oxide wüstite ($Fe_{1-x}O$). *Yearbook Carnegie Institution of Washington, 79,* 374–376.